# Modeling and Control of Half-wave Rectified Rotor Brushless Synchronous Motor

**By**

**Getsh Fikadie**

**A Thesis Submitted to the School of Graduate Studies of Addis Ababa University in Partial Fulfilment of the Requirements for the Degree of Masters of Science in Control Engineering**


Thesis Supervisor: Assoc. Prof. Mengesha Mamo, (PhD.)

August 2020

Addis Ababa, Ethiopia


## School of Electrical and Computer Engineering

# Modeling and Control of Half-wave Rectified Rotor Brushless Synchronous Motor

(Addis Ababa, Ethiopia)

**APPROVAL BY BOARD OF EXAMINERS**

| | |
|---|---|
| Dr. Dereje Shiferaw | _____ |
| Chairman | Signature |
| Assoc. Prof. Mengesha Mamo (PhD.) | _____ |
| Advisor | Signature |
| Mr. Yared Tadesse | _____ |
| External Examiner | Signature |
| Dr. Lebsework Negash | _____ |
| Internal Examiner | Signature |

# Declaration

I declare that the work entitled “Modeling and Control of Half-wave Rectified Rotor Brushless Synchronous Motor” is my original work and has not been presented for any degree in this university or any other university or colleges, as well as all sources of material, used for the thesis have been duly acknowledged.

| | |
|---|---|
| Getsh Fikadie | Date |

# Acknowledgments

First and foremost I would like to give a huge thanks to my advisor, Assoc. Prof. Mengesha Mamo who has given me a great support and guidance throughout the whole work. I am deeply indebted to my friends for their continuous support and encouragement over the years. I also would like to thank my family for the unconditional support and absolute understanding during the writing of this thesis.

# Abstract

In this thesis, modeling and control of the half-wave rectified rotor brushless synchronous motor is presented. The motor has a range of promising performance characteristics that are suitable for electric vehicle (EV) traction drive applications. Its mechanical structure is simple and robust with brushless means of field excitation capable of variable field flux control over a wide range of operating speed and torque. To use the motor for such application, accurate modeling and characterization of the motor is needed. Two different modeling paradigms were used to study the behavior of the motor.

The finite element method (FEM) was used to first verify the principle of operation and next to confirm the analytical model calculations. COMSOL Multiphysics was used to perform the two dimensional (2D) FEM analysis. Besides the FEM model, a simplified analytical model and Simscape based model convenient for MATLAB/Simulink simulations and control system design purposes were also built using the magnetic equivalent circuit concept. The analytical model developed in this thesis uses a closed form analytical expression for the field winding current, $i_{fd}$, derived from observing FEM model behavior. This enabled a more complete description of basic motor characteristics that allowed determination of motor capabilities, limits and design of controllers which were not possible without the use of the such closed form expressions. Comparison of the responses of those models was performed. Field oriented control (FOC) based architecture was used to design and implement a velocity control system for both the FEM based and Simscape based models.

The results show that the three models agree as long as effects due to the inductance variation of the FEM model because of iron cores saturation (motor load) and stator slots are taken into account. The three models showed a logarithmic relationship between the bias frequency $f_b$ and motor torque, field winding current and flux. The field winding flux was shown to be linearly dependent on the amplitude of the field excitation current component $I_f$ of the stator current for a fixed bias frequency $f_b$. The decoupled nature of field flux and torque currents allowed implementation simple PI based speed and current controllers. In terms of field winding flux linkage variation, the analytical showed a $1.7\%$, Simscape a $14.8\%$ and FEM a $18.4\%$ of maximum deviation from the ideal constant flux. As long as the basic motor characteristics such as flux, torque and efficiency are considered, the models can be used interchangeably.

***Keywords***— 2D FEM, variable flux, Simscape, half-wave rectified rotor excitation, brushless

# Contents

# List of Figures

# List of Tables

# Listings

# List of Abbreviations

| | |
|---|---|
| 2D | two dimensional |
| 3D | three dimensional |
| AV | across variable |
| cir | electrical circuit |
| DAE | differential algebraic equation |
| DQ | direct-quadrature |
| EMF | electromotive force |
| EV | electric vehicle |
| FEM | finite element method |
| FOC | field oriented control |
| ge | Global Equation |
| HRRBSM | half-wave rectified rotor brushless synchronous motor |
| IM | induction motor |
| KVL | Kirchhoff's voltage law |
| mf | Magnetic Fields |
| MMF | magnetomotive force |
| ODE | ordinary differential equation |
| PDE | partial differential equation |
| PI | proportional integral |
| PMSM | permanent magnet synchronous motor |
| rmm | rotating machinery magnetic |
| TV | through variable |
| ZDAC | zero d-axis control |

# Chapter 1

# Introduction

## 1.1 Background

Electric Vehicles (EVs) are motor vehicles that partially (Hybrid Electric Vehicles, HEV) or completely (Batter Electric Vehicles, BEV) use electric propulsion systems. EVs have been rapidly gaining popularity in the global automobile market due to the following reasons:

- Lower maintenance and running costs
- Better for environment
- Safety improvements
- Government initiatives

One of the main components of EVs is the traction motor. The two primary types of AC traction motors, permanent-magnet and induction, have their own advantages and limitations for automotive applications. Many automakers and suppliers have favored permanent magnet synchronous motor (PMSM) because they typically are inherently more efficient. Honda, Toyota, GM and BMW, as well as many major suppliers, currently use permanent-magnet motors in production vehicles. Tesla uses induction motors induction motor (IM) for its larger and more performance-oriented Model S and Model X vehicles, but elected permanent-magnet drive motors for its most recent (and smaller) Model 3 vehicle [1].

IMs have dominated the electric vehicle industry for the past few decades due to being rugged, easy to manufacture and cheap. However, the problem with induction motors is that they have narrow high efficiency area and controllable torque area, i.e. there is a limited range of operating speed at which high efficiency can be attained and at which torque control is possible. IMs are preferred if high power output is a factor. PMSMs are used (but not limited) to smaller, efficiency-focused vehicles because of their high torque density. However, the supply of permanent magnet materials, especially rare-earth elements, is very limited and fluctuating that the corresponding market prices for permanent magnet based devices, like PMSMs, are soaring and volatile. Besides, the manufacturing process of these rare-earth element permanent magnets have severe environmental effects and health issues.

Although they can be the best option in many cases, PMSMs present a huge limitation as a traction motor. The drive cycle of most EVs is dominated by high speed operation region. The permanent magnets in PMSMs produce fixed field (rotor) magnetic flux which generates (induces) proportionally high back-electromotive force (back-emf) voltage at the stator winding when these motors are operated in this high-speed region. This back-emf voltage opposes the stator voltage supply. There is a limit in the stator voltage that can be applied to the motor and is determined by the voltage rating of the motor and the capacity of the inverter supplying power to the motor. The back-emf voltage opposing this stator voltage limits the stator current that can be supplied to the motor and thus limiting the motor electromagnetic torque.

To operate PMSMs at high-speed region, the influence of the back-emf voltage has to be reduced by weakening the field flux generated by the permanent magnet using an additional stator current that produces an opposite magnetic flux to that produced by the permanent magnet (flux weakening). Therefore, using field weakening scheme to extend the constant power operation requires additional current which results in copper loss and hence lower motor efficiency. As a result, several methods of replacing the permanent magnets have been tried over the past few decades. Higher order harmonic, and spatial sub-harmonic means of field excitation methods have been investigated in [2, 3, 4]. These techniques require additional winding configurations in the stator or rotor. More than one inverters are also needed to drive such type of machines.

Another simple solution proposed in literature is the use of brushless, self-excited synchronous motors to partially or completely replace the magnets. The half-wave rectified brushless synchronous motor studied in this thesis consists of a rotor with a field winding short circuited through a diode. The stator of this motor is the conventional stator equipped with a three-phase winding. The current fed to the stator consists of an arbitrary three-phase current superimposed with a pulsating current. The pulsating current, which can be any kind of periodic ac waveform with its own frequency known as bias frequency, is made to rotate synchronously with the d-axis of the rotor. An alternating magnetomotive force (MMF) rotating synchronously with the d-axis of the rotor is thus produced by this pulsating current, linking the rotor (field) winding. This then induces an electromotive force (EMF) in the field winding which is half-wave rectified by the diode integrated into the field winding to generate the excitation current needed [5].

This brushless synchronous motor has following special merits:

1 The machine structure is same as the conventional synchronous motor except that the field winding is short-circuited through a diode. Thus, the motor is simple, robust and maintenance free.

2 Due to the decoupling of the excitation current and the torque current, torque control capability is possible only by detecting the position of the rotor over the speed range from the state of stand-still (occasionally containing the position control) and is easier than that of IMs.

3 The average value of the flux linkage held in the field winding is determined by the peak value of the excitation current supplied to the three-phase stator windings. Consequently, motor characteristics are not affected by the variations of the machine parameters caused by, for instance, temperature rise, which is usually the case in PMSMs.

4 Field weakening operation is simpler in high speed region because direct control of field winding flux is possible.

5 Higher power machine than a conventional synchronous motor can be easily designed by combining permanent magnet and half-wave rectified excitation.

## 1.2 Problem Statement

In order to use this motor in a range of applications, its behavior has to be properly studied and investigated. In addition, variable speed drive control system design for the motor would require appropriate model capable of representing the motor's characteristics accurately. Due to the complicated principle of operation (owing to the presence of rectifying diode in the rotor winding and non-sinusoidal form of current waveform) of this motor, it is difficult to accurately analyze the operating characteristics using classical machine analysis approaches. Experimental investigations have been used in literature [6, 7, 8, 9]. In the real-life motor a number of factors affect its behavior. It is usually difficult and time consuming to distinguish which factor affects what characteristic and in what way. Actual testing of a prototype is also costly and may not reveal what is actually going on inside the machine in terms of the magnetic flux distribution. Instead, investigation of the underlying physics behind the characteristics of this machine using modern powerful numerical tools can provide us the ability to model and characterize the machine more easily with a reasonable degree of accuracy.

Unlike ordinary electric machines like IMs and PMSMs, the motor studied in this thesis

## 1.3 Objectives

### 1.3.1 General Objective

- To model a half-wave rectified rotor brushless synchronous motor (HRRBSM) using the finite element method and analytical methods for study, analysis and further drive control design purposes for EV traction applications.

### 1.3.2 Specific Objectives

- To model the half-wave rectified rotor brushless synchronous motor (HRRBSM) in using the finite element method (FEM).
- To investigate the operating characteristics of the model using the FEM model.
- To extract model parameters of the motor from the FEM model for analytical model and MATLAB/Simulink modeling in the Simscape physical systems modeling toolbox.
- To develop a closed form analytical and Simscape models for the motor
- To implement a simple field oriented control for the motor in MATLAB/Simulink

## 1.4 Scope and Relevance

This thesis involves the characterization (model generation) and analysis of a half-wave rectified synchronous motor without permanent magnet using modern numerical computational tools and analytical methods based on magnetic equivalent circuits analysis method. Specifically, the magnetic flux distribution within the motor geometry is computed using 2D FEM modeling and used for extraction of machine parameters such as coil inductance and resistance, computation of motor performance characteristics like torque, induced voltage is performed. Approximate closed form analytical model is also built for variable speed control system design. After the model is built and its characteristics are analyzed, controller configuration that will be more appropriate for traction application is suggested.

## 1.5 Motivation

Conversion of the transportation industry from internal combustion engines (ICE) based vehicles to EVs is one approach of slowing down the progress of climate change mainly caused by emissions from ICE propelled vehicles. Such conversion requires development of efficient electric machines at a market competitive price. The motor studied in this thesis is such a machine with its simple rugged structure, easy torque and field flux controllability and absence of permanent magnets or brushes. This thesis is thus an effort to contribute to the industry's exploitation of this promising idea.

## 1.6 Thesis Contributions

In general, the following contributions have been made

1. A set of closed form analytical equations that describe motor behavior in a general manner were derived. These equations depended on the derivation of a closed form equation describing the relationship between field winding current $i_{fd}$ and stator d-axis current $i_d$ which was accomplished in this thesis by using careful observation of the motor behavior.
2. Method of motor behavior analysis using its voltage and current limit curves was provided.
3. A Simscape library model was built for the motor that is portable and can be used by anyone interested to study the motor within the MATLAB/Simulink environment.

## 1.7 Thesis Outline

1. **Chapter 2** Explains theoretical background on FEM theory and machine analysis plus related research works done on the motor.
2. **Chapter 3** Deals with the methods used to model the motor using analytical methods, the FEM approach using COMSOL Multiphysics and in the MATLAB/Simulink environment.
3. **Chapter 4** Presents the results obtained along with a discussion on those results
4. **Chapter 5** Concludes the thesis adding recommendation and future works to be done.

# Chapter 2

# Literature Survey

## 2.1 Modeling

Mathematical modeling is the art of transforming science and engineering problems in the physical world into tractable mathematical formulations in a conceptual world [10]. Mathematical models can be classified into:

**Empirical models** models based on the interpretation of data obtained from a series of experimentation

**Conceptual models** models based on the algebraic, integral or differential equations that describe the fundamental laws of physics governing the system under consideration.

In electrical machines, Maxwell's equations are used as the basis of the conceptual models. These equations describe the distribution of electric and magnetic fields within the geometry of the machines. Modeling electric machines thus involves the process of applying these space and time dependent equations and determining the solutions of such equations. Based on the method used for arriving at these solutions, conceptual models are further subdivided into analytical (theoretical) and numerical models.

Analytical models describe systems using mathematical equations whose solutions are functions usually dependent on the problem and/or geometry. They can only be applied to problems with simple geometries. Using some simplifying assumptions however, complex multi-dimensional field problems can be reduced to one-dimensional (time-dependent) circuit equivalent models suitable for easy analysis with acceptable accuracy. The space-dependent magnetic flux distribution part of the equations can be encapsulated using coil flux linkage idea. The flux linkage contains the necessary information about the magnetic field behavior of the winding and core combination. Winding inductance is used to relate this magnetic behavior to electric current flowing through those windings. This approach is usually known as the concept of magnetic circuits and is the most commonly used method of modeling, analyzing and designing electrical machines.

Numerical models on the other hand provide the solution for the governing equations using approximate methods. Figure 2.1 shows the relationship between the real-life device, the numerical simulation and the classical analytical theory. From the figure it is obvious that the numerical simulation is a connecting element between reality, measurements, and analytical predictions. The

numerical computations can be assumed to represent realistic activities in a fictitious laboratory. This means that simulation results should be theoretically measurable in practice. The numerical simulation is in fact an experiment performed on the computer as a fictitious laboratory, where the engineer is using numerical tools to perform the experiments instead of measurement devices such as current, voltage, power, temperature and force meters [11].

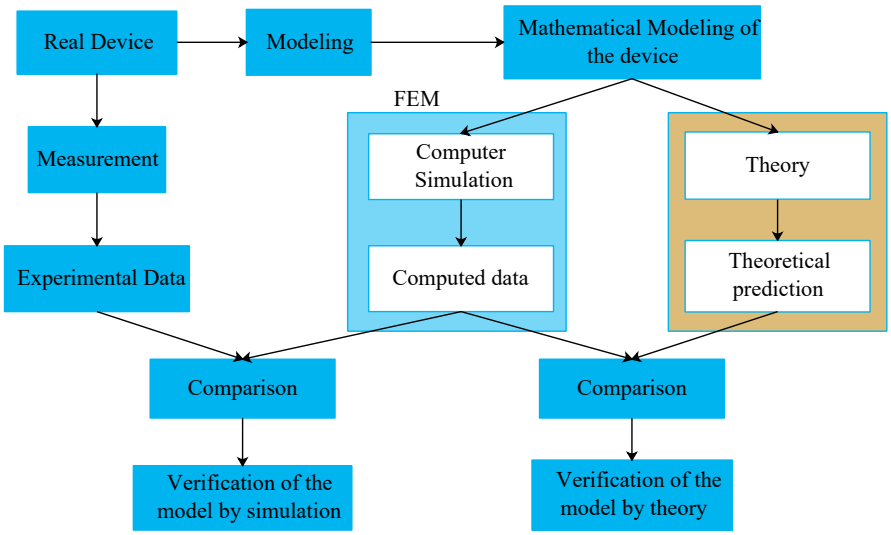


Figure 2.1: Theory experimentation and simulation, taken from [11]

The verification of numerical solutions and results obtained by the analytical theory, performed by comparing their predictions of device characteristics, can lead to improved analytical models and vice versa. Under certain circumstances numerical solutions provide insight into how to approach the analytical solutions. Both numerical simulation and analytical theory help to understand the physical reality and to improve technical predictions.

The finite element method is such a numerical method suitable for multi-physical devices, such as electric machines [12]. It is an excellent tool that fits with the strictest design requirements of electrical industry. Therefore, it is crucial to dispose of software packages specially conceived for designing and analyzing the rotating electrical machine in detail, from which a near-optimum design may be obtained. It is in this area where FEM packages offer an integrated powerful solution. They are currently being applied instead of the classical analytical and experimental methods, which require expensive and nonflexible prototyping.

## 2.2 FEM Theory

Electrical machines are very complex devices that involve electromagnetic, thermal, mechanical and structural aspects, to name a few. Those aspects are described using space and time dependent partial differential equation (PDE). Analyzing, designing and modeling these devices thus requires the solution of these PDEs. For complex systems like electric machines involving complicated geometries, the use of analytical methods to find an exact solution is almost impossible due to the nature of the problem. An alternative option is to search for approximate numerical solutions. The Finite Element Method (FEM) is exactly this type of method – a numerical method for the solution

of PDEs. Especially, the multiphysics approach used in many of the FEM softwares enables users to account for most of the important physical behaviors of electrical machines during design, analysis and drive system development stages [13].

The FEM offers improved accuracy and almost an unlimited flexibility in the geometrical shape, boundary conditions, and material properties in different regions of the problem domain [14].

### 2.2.1 Revision of Maxwell's Equations

The electromagnetic aspect of electrical machines can be studied with the use of Maxwell's equations that describe the relationship among the electric flux intensity $\boldsymbol{E}$, electric flux density $\boldsymbol{D}$, current density $\boldsymbol{J}$, magnetic flux density $\boldsymbol{B}$, and magnetic field intensity $\boldsymbol{H}$ as provided in the following equations [15].

$$\nabla \times \boldsymbol{E} = -\frac{\partial \boldsymbol{B}}{\partial t} \tag{2.1a}$$

$$\nabla \times \boldsymbol{H} = \boldsymbol{J} + \frac{\partial \boldsymbol{D}}{\partial t} \tag{2.1b}$$

$$\nabla \cdot \boldsymbol{D} = \rho \tag{2.1c}$$

$$\nabla \cdot \boldsymbol{B} = 0 \tag{2.1d}$$

where $\rho$ is the volume charge density in the region under consideration. Equation (2.1b) is commonly referred to as **Ampere's Law**. The following constitutive relations that describe the macroscopic properties of the medium are also required to obtain a closed system.

$$\boldsymbol{B} = \mu \boldsymbol{H} \tag{2.2a}$$

$$\boldsymbol{D} = \epsilon \boldsymbol{E} \tag{2.2b}$$

$$\boldsymbol{J} = \sigma \boldsymbol{E} \tag{2.2c}$$

where $\mu$, $\epsilon$, and $\sigma$ are the permeability, the permittivity, and the electrical conductivity of the materials (media) involved. Usually these parameters are given in the form given below:

$$\mu = \mu_r \mu_0 \tag{2.3a}$$

$$\epsilon = \epsilon_r \epsilon_0 \tag{2.3b}$$

where $\mu_r$ and $\epsilon_r$ are the relative permeability and permittivity of the materials, assuming linear materials. $\mu_0$ and $\epsilon_0$ are permeability and permittivity of vacuum that have the following values in the SI system:

$$\mu_0 = 4\pi \cdot 10^{-7} H/m \tag{2.4a}$$

$$\epsilon_0 = 8.854 \cdot 10^{-12} F/m \tag{2.4b}$$

For some materials, the relationship between $\boldsymbol{B}$ and $\boldsymbol{H}$ is nonlinear such that

$$\boldsymbol{B} = f(|\boldsymbol{H}|) \tag{2.5}$$

Common iron core materials used in electrical machines have the above nonlinear magnetic property where the relationship is described using a table of $\boldsymbol{H}$ and corresponding $\boldsymbol{B}$ values.

In certain cases, the solution for Maxwell's equations can be simplified by introducing the concepts of electric scalar potential $V$ and magnetic vector potential $\boldsymbol{A}$ defined as:

$$\boldsymbol{B} = \nabla \times \boldsymbol{A} \tag{2.6a}$$

$$\boldsymbol{E} = -\nabla \cdot V - \frac{\partial \boldsymbol{A}}{\partial t} \tag{2.6b}$$

For example for a two dimensional magnetostatic problem, the vector potential concept is a useful approach which reduces the number of unknown functions from two ($B_x$ , and $B_y$ ) to one ($A_z$) [14].

### Boundary and Physics Interface Conditions

To get a full description of an electromagnetics problem, boundary conditions must be specified at material interfaces and physical boundaries. At interfaces between two media, the boundary conditions can be expressed mathematically as [15]

$$\boldsymbol{n_2} \times (\boldsymbol{E_1} - \boldsymbol{E_2}) = \boldsymbol{0} \tag{2.7a}$$

$$\boldsymbol{n_2} \cdot (\boldsymbol{D_1} - \boldsymbol{D_2}) = \rho_s \tag{2.7b}$$

$$\boldsymbol{n_2} \times (\boldsymbol{H_1} - \boldsymbol{H_2}) = \boldsymbol{J_s} \tag{2.7c}$$

$$\boldsymbol{n_2} \cdot (\boldsymbol{B_1} - \boldsymbol{B_2}) = 0 \tag{2.7d}$$

where $\rho_s$ and $\boldsymbol{J_s}$ denote surface charge density and surface current density, respectively, and $\boldsymbol{n_2}$ is the outward normal from medium two.

### Electromagnetic Forces

The calculation of electromagnetic forces involves the computation of volume forces acting on a body, and of surface forces originating from jumps in the electromagnetic fields on the boundaries.

Among the several methods of computing the electromagnetic forces acting on a body within a given field problem, COMSOL Multiphysics, by default, uses the Maxwell stress tensor approach. In this approach, the total electromagnetic force acting on a given body is calculated by summing the local magnetic stress at all points of the surface surrounding the body. The Maxwell stress tensor contains this information of local magnetic stress values at the points within the surface. This quantity for air is given by [15] (p. 49)

$$T = -pI - \left(\frac{\epsilon_0}{2}\boldsymbol{E}\cdot\boldsymbol{E} + \frac{1}{2\mu_0}\boldsymbol{B}\cdot\boldsymbol{B}\right) I + \epsilon_0 \boldsymbol{E}\boldsymbol{E}^T + \frac{1}{2\mu_0}\boldsymbol{B}\boldsymbol{B}^T \tag{2.8}$$

where $p$ is air pressure and $I$ is a 3-by-3 tensor. The total force is computed as a boundary integral of the stress tensor in vacuum or air surrounding the solid. Thus, the general expression for the force $\boldsymbol{F}$ and torque $\boldsymbol{\tau}$ is given by:

$$\boldsymbol{F} = \oint_{\partial\Omega} d\boldsymbol{n_1} T dS \tag{2.9}$$

$$\boldsymbol{\tau} = \oint_{\partial\Omega} d(\boldsymbol{r} - \boldsymbol{r_0}) \times (\boldsymbol{n_1} T) dS \tag{2.10}$$

where $\boldsymbol{r_0}$ is a point on the axis of rotation $\boldsymbol{r}$ is the vector traversing the boundary surface $\partial\Omega$.

**Flux Linkage**

The magnetic flux through a surface $S$ oriented by the normal vector $\boldsymbol{n}$ , is given by

$$\Phi = \int_S \boldsymbol{B} \cdot \boldsymbol{n} dS = L_m \int_{l_s} \boldsymbol{B} \cdot \boldsymbol{n} dl \tag{2.11}$$

Or using Stoke's theorem, one can have

$$\Phi = \int_S \boldsymbol{B} \cdot \boldsymbol{n} dS = \int_S \nabla \times \boldsymbol{A} \cdot \boldsymbol{n} dS \tag{2.12}$$

Coil flux linkages can be computed by appropriety selecting the surface $S$ and calculating using the above equations.

If the field distribution ($\boldsymbol{B}$ or $\boldsymbol{A}$) at every point of interest is known, then Equations (2.1) along with Equation (2.10) and (2.12) can be used to describe the performance of the machine in terms of voltage, flux, power, etc...

### 2.2.2 Numerical Solution of Maxwell's Equations

The general vector field problem that needs to be solved in a given domain[1] $\Omega$ can be described by the differential equation given as

$$L\phi(\boldsymbol{x}, t) = f(\boldsymbol{x}, t) \tag{2.13}$$

where $L$ is a differential operator, $\phi$ is the unknown function, and $f$ is the forcing function, $\boldsymbol{x}$ is the vector of space coordinates of the point and $t$ is time [16]. For example, for a magnetostatic problem **Ampere's Law** in Equation (2.1b) implies $L = \nabla\times$, $\phi = \boldsymbol{H}$, and $f = \boldsymbol{J}$. Equation (2.13) describes the distribution of the field $\phi$ for all points of the domain $\Omega$. In addition, field problems can also have constraints given as a set boundary conditions. These boundary conditions specify the value of the unckown function $\phi$ along the boundaries $\Gamma$.

### 2.2.3 Solution of the Field Problem

Finding an exact solution $\phi$ that satisfies Equation (2.13) along with the boundary conditions using analytical methods is in most cases impossible. This is because electrical machines are built using complex geometrical arrangement and contain materials with nonlinear magnetic and electric properties. This makes the equations describing the field distribution within the machine geometry very complex. Thus, numerical methods are usually applied to arrive at an approximate solution. The FEM is such a numerical method suitable for a wide range of problems. The general FEM approach used for a static 2D field problem is described as follows.

In numerical methods the function $\phi^*$ that approxiamtes the unknown function $\phi$ is defined as a linear combination of interpolating (basis) functions $v_j$ as

$$\phi^*(\boldsymbol{x}, t) = \sum_{j=1}^{N} \Phi_j v_j(\boldsymbol{x}, t) \tag{2.14}$$

where $\Phi_j$ are the unknown coefficients that have to be determined during the computation process. Thus, finding an approximate solution $\phi^*$ means finding these unknown coefficients. This can be

[1] any region of space in which the problem is defined

achieved using different techniques one of which is the residual (Galerkin's) method. This method solves the field problem by reducing the residual of the differential equation defined as

$$r = L\phi^* - f \tag{2.15}$$

If the function $\phi^*$ approximates the actual solution $\phi$, then the residual $r$ is equal to zero or very low in the whole domain of analysis. A more appropriate approach used in the residual method is to force the integral of the residuals weighed by some weight functions $w_i$ to zero over the whole domain $\Omega$.

$$R_i = \int_\Omega w_i(L\phi^* - f)d\tau = 0 \tag{2.16}$$

In the Galerkin's method the weight functions $w_i$ are chosen to be equal to the interpolating functions $v_i$, i.e. $w_i = v_i$ for $i = 1,\ 2,\ 3,\ ...,\ N$ Finally, the weighed residual becomes

$$R_i = \int_\Omega \left[ v_i L \left( \sum_{j=1}^{N} \Phi_j v_j \right) - v_i f \right] d\tau = 0 \tag{2.17}$$

which results in a system of equations of the form

$$[SS][\phi] = [T] \tag{2.18}$$

where $[\phi]$ is the column vector of unknown coefficients $\Phi_j$, [SS] is an $N \times N$ matrix that depends on the interpolating functions whose elements are given by

$$s_{ij} = \frac{1}{2} \int_\Omega \left( v_i L v_j + v_j L v_i \right) d\tau \tag{2.19}$$

The vector $[T]$ in Equation (2.18) is an $N \times 1$ column vector whose elements are given by

$$t_i = \int_\Omega v_i f d\tau \tag{2.20}$$

Equation (2.18) can the be solved for $[\phi]$ using numerical methods giving the required coefficients $\Phi_i$, thus the approximate solution as in Equation (2.14).

For large and complex domain geometries with nonlinear material properties, choosing the appropriate interpolating functions is a difficult task. The selection of the interpolating functions $v_i$ can be simplified by dividing the whole domain into fixed number of small subdomains. It follows that, because of the small dimension of these subdomains, the function $\phi$ is approximated by simple interpolating functions whose coefficients are the unknown quantities. This is the FEM.

### Finite element analysis steps for static problems

Based on the above approach, the general steps followed in FEM analysis are [17]:

1. Divide the domain into many small, nonoverlapping elements, which are called mesh elements
2. Select appropriate local interpolation functions or basis functions
3. Formulate system equation
4. Solve

### Mesh Generation

In this step the domain is subdivided into $N_m$ element domains $\Omega_m$ ($m = 1, 2, 3, ..., N_m$). The number of such subdomains affects the solution accuracy. In general better accuracy can be obtained by using larger numbers of elements. However this will require bigger memory and computational resources. For 2D problems, the most common elements are triangular and/or rectangular in shape, see Figure 2.2. The figure shows the field region subdivided into an arbitrary number of triangles. The only requirement for the construction of the triangle elements is that the triangles are nonovelapping and all nodes are connected.

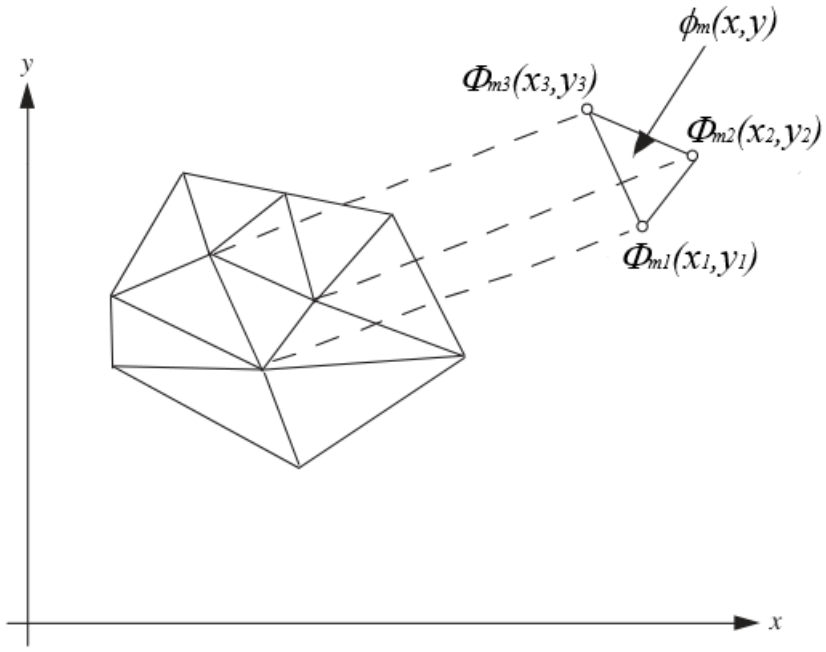


Figure 2.2: Typical mesh grid for a 2D field problem, adopted from [14]

### Interpolation function selection

During this step the interpolating (shape) functions $v_i$ in Equation (2.14) are defined for each mesh element. These functions are usually polynomials of the space coordinates. The order of the polynomial determines the type of discretizaton used in FEM, i.e., first order polynomial–linear discretization, second order polynomial–quadratic discretization, and so on. For the problem in Figure 2.2, one can have

$$\phi_m^*(x,y) = \sum_{j=1}^{n} \Phi_{mj} v_{mj}(x_m, y_m) \tag{2.21}$$

where $\Phi_{mj}$ is the value of $\phi$ at the $j$-th node of the $m$-th element, n is the number of nodes.

For example, for triangular mesh elements just like as shown in Figure 2.2 if linear discretization is assumed in which the interpolating function is linear both in the space coordinates $x$ and $y$, the functions $v_{mj}$ can be defined for each the element as

$$v_{m1} = \frac{1}{2\Delta}(a_1 + b_1 x + c_1 y) \tag{2.22a}$$

$$v_{m2} = \frac{1}{2\Delta}(a_2 + b_2 x + c_2 y) \tag{2.22b}$$

$$v_{m3} = \frac{1}{2\Delta}(a_3 + b_3 x + c_3 y) \tag{2.22c}$$

where $\Delta$ given by

$$\Delta = \frac{1}{2}[(x_2 y_3 - x_3 y_2) + x_1(y_2 - y_3) + y_1(x_3 - x_2)] \tag{2.23}$$

is the area of the triangle element $m$. The coefficients $a_i$, $b_i$, $c_i$ are chosen to make the value of the interpolating function $v_{mi}$ equal to 1 at node $i$ and zero at the other nodes. Thus, one can have

$$\begin{aligned} a_1 &= x_2 y_3 - x_3 y_2, \quad & b_1 &= y_2 - y_3, \quad & c_1 &= x_3 - x_2 \\ a_2 &= x_3 y_1 - x_1 y_3, \quad & b_2 &= y_3 - y_1, \quad & c_2 &= x_1 - x_3 \\ a_3 &= x_1 y_2 - x_2 y_1\ , \quad & b_3 &= y_1 - y_2, \quad & c_3 &= x_2 - x_1 \end{aligned}$$

The basis functions in this case are chosen to be linear (first order) functions of the space coordinates $(x, y)$. Higher order polynomials of $x$ and $y$ can be used for better accuracy.

### Formulation of System Equation

Once the interpolating functions are defined, Equation (2.21) is applied for each element as

$$R_{im} = \int_{\Omega_m} v_i (L\phi_m^* - f_m) d\tau = 0 \tag{2.24a}$$

$$= \int_{\Omega_m} \left[ v_i L \left( \sum_{j=1}^{n} \Phi_{mj} v_{mj} \right) - v_i f_m \right] d\tau = 0 \quad i = 1,\, 2,\, ...,\, n \tag{2.24b}$$

which gives a system of $n$ equations with $n$ unknowns, $\Phi_{mj}$.

A particular node can be a vertex of an arbitrary number of elements, in which case a single matrix equation can be formed out of adjoining the appropriate elements of each of the mesh network. This one global equation can be written as:

$$[SS][\phi] = [T] \tag{2.25}$$

Equation (2.25) consists of $N_n$ equations with $N_n$ unknowns of nodal values $\Phi_j$. $N_n$ here is the total number of nodes of the whole domain mesh network sometimes also known as number of degrees of freedom of the solution. The boundary conditions are also included within Equation (2.25) during this step of the solution process.

### Solution

Equation (2.25) can consist of either linear or non-linear set of equations depending mostly on the material properties of the domain, i.e. the constitutive relations. Solution of the problem can then be computed using any of the commonly used numerical methods (Gauss-Jordan method for linear problems or Newton-Raphson iterative method for non-linear problems.) The vector of unknown potentials $[\phi]$ can then be solved for every node in the network from Equation (2.25) which then can be used to determine the potential inside each triangle from Equation (2.21).

### 2.2.4 Time Stepping

When the field problem is time dependent, the FEM method usually implements an independent discretization of the time domain, i.e.

$$\frac{\partial \phi}{\partial t} \approx \frac{\phi_{m,t+\Delta t} - \phi_{m,t}}{\Delta t} \tag{2.26}$$

Thus, the field problem is solved at each time step. Modern time-stepping algorithms control the time marching scheme by varying the length of the time step length depending on the problem and the evolution of the solution with time [18].

## 2.3 Analytical Machine Equations

A simplified version of Maxwell's equations describing a given electrical machine can be formulated using the following assumptions [19, 20]:

a) due to the high permeability of the iron cores used, almost all of magnetic flux is confined to the iron cores much like electric currents are confined to the conducting wires in electric circuits.

b) stator windings are sinusoidally distributed along the air-gap.

c) no variation of rotor self-inductance with rotor position

d) magnetic hysteresis and saturation effects are negligible

Assumption (a) is based on the fact that the magnetic flux lines always prefer paths of low magnetic reluctance. Thus, the magnetic flux is confined to the iron cores in the stator and rotor (i.e. no appreciable magnetic flux distribution at stator slots or rotor inter-polar regions). However, at the air gap between stator and rotor there is no alternative path to take. In addition, the air gap width is comparatively small at certain regions (for salient pole machines). So, the flux lines can easily cross the air gap to link the stator and rotor winding (see Figure 2.3).

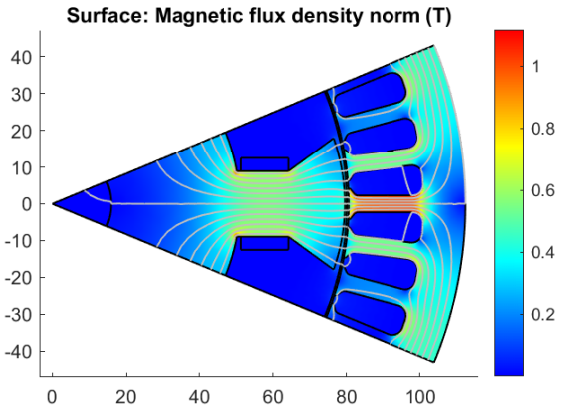


Figure 2.3: Typical magnetic flux distribution in an electric machine

Based on these assumptions, the equivalent circuit representation of a three-phase synchronous machine will be as follows.

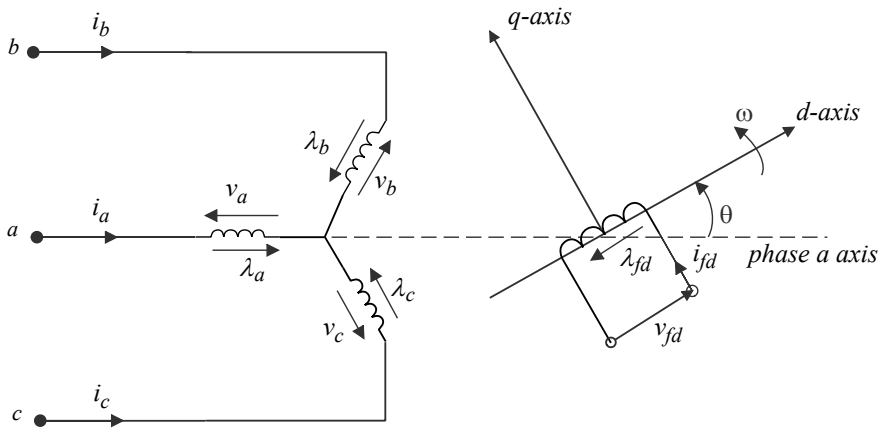


Figure 2.4: Salient-pole synchronous machine equivalent circuit

The $d-$and $q-$ axes in the figure are new reference frame axes that are convenient for machine analysis and will be described shortly. Magnetic flux produced by one of the stator or the rotor windings links the other windings, implying that these windings are magnetically coupled. With the assumption of linear flux-current relationship through the used of the inductance concept, the following set of equations can be derived for a general three-phase synchronous machine.

### Equations of Stator Circuits

In Figure 2.4, motor convention is used for polarities where positive direction of stator phase currents is assumed to flow into the positive terminal of the phase windings. The instantaneous voltage equations can now be written for each phase of the stator winding as.

$$v_a = \frac{d\lambda_a}{dt} + R_a i_a \tag{2.27a}$$

$$v_b = \frac{d\lambda_b}{dt} + R_b i_b \tag{2.27b}$$

$$v_c = \frac{d\lambda_c}{dt} + R_c i_c \tag{2.27c}$$

where, in most cases $R_a = R_b = R_c$, and where we have

$$\lambda_a = l_{aa} i_a + l_{ab} i_b + l_{ac} i_c + l_{afd} i_{fd} \tag{2.28a}$$

$$\lambda_b = l_{ba} i_a + l_{bb} i_b + l_{bc} i_c + l_{bfd} i_{fd} \tag{2.28b}$$

$$\lambda_c = l_{ca} i_a + l_{cb} i_b + l_{ca} i_c + l_{cfd} i_{fd} \tag{2.28c}$$

For the purpose of simplicity, rotor damper windings are not considered in this thesis. The inductance terms $l_{aa}$, $l_{bb}$, $l_{cc}$ are the self inductances of the stator phase windings, which can generally be expressed as [20]:

$$l_{aa} = L_{aa0} + L_{aa2}\cos(2\theta) \tag{2.29a}$$

$$l_{bb} = L_{aa0} + L_{aa2}\cos(2\theta - \frac{2\pi}{3}) \tag{2.29b}$$

$$l_{cc} = L_{aa0} + L_{aa2}\cos(2\theta + \frac{2\pi}{3}) \tag{2.29c}$$

As seen from the above equations, the inductance terms are rotor electrical angle $\theta$ dependent. The mutual inductance terms $l_{ab}$, $l_{ac}$, $l_{cb}$, etc in the above equations are also rotor position dependent terms which can be described as:

$$l_{ab} = l_{ba} = -L_{ab0} - L_{ab2}\cos(2\theta + \frac{\pi}{3}) \tag{2.30a}$$

$$l_{bc} = l_{cb} = -L_{ab0} - L_{ab2}\cos(2\theta - \pi) \tag{2.30b}$$

$$l_{ac} = l_{ca} = -L_{ab0} - L_{ab2}\cos(2\theta - \frac{\pi}{3}) \tag{2.30c}$$

Rotor and stator circuit mutual inductances $l_{afd}$, $l_{bfd}$ and $l_{cfd}$ are the mutual inductances of the field winding with the phases $a$, $b$, and $c$ of the stator winding, respectively, given as.

$$l_{afd} = L_{afd}\cos(\theta) \tag{2.31a}$$

$$l_{abd} = L_{afd}\cos(\theta - \frac{2\pi}{3}) \tag{2.31b}$$

$$l_{acd} = L_{afd}\cos(\theta + \frac{2\pi}{3}) \tag{2.31c}$$

**Equations of Rotor Circuits**

The rotor (field winding) circuit voltage equations have similar form to the stator voltage equations.

$$v_{fd} = \frac{d\lambda_{fd}}{dt} + R_{fd}i_{fd} \tag{2.32}$$

where

$$\lambda_{fd} = l_{ffd}i_{fd} + l_{afd}i_a + l_{bfd}i_b + l_{cfd}i_c \tag{2.33}$$

Unlike most of the inductance terms seen previously, $l_{ffd}$, the self-inductance of the field winding, remains constant irrespective of rotor position.

### 2.3.1 Direct-quadrature (DQ) axis frame model

As one can observe from the above equations, the stator self- and mutual-inductance terms are rotor position dependent, making the coefficients of the differential equations (voltage equations) that describe the behaviour of the motor time-varying, except when the rotor is stalled [21]. Analysis using these forms of equations is cumbersome and error prone. Thus, in rotating electric machines studies, a change of variables is used to reduce the complexity of these differential equations. Change of variables involves refering machine variables to an arbitrary frame of reference. For example, Park's transform refers to a change of variables in which machine variables (current, voltage, flux linkages) associated with the stator windings can be replaced by new variables associated with fictious (d- and q-) windings rotating with the rotor. This eliminates the time-varying inductances caused by the relative motion between the stator and rotor.

Any general change of variables that refers a set of variables $\boldsymbol{f}_{abc}$ from the $abc$ frame to an other set of variables $\boldsymbol{f}_{dq0}$ in the arbitrary frame $dq0$ is given by the equation

$$\boldsymbol{f}_{dq0} = T\boldsymbol{f}_{abc} \tag{2.34}$$

where

$$\boldsymbol{f}_{dq0} = \begin{bmatrix} f_d \\ f_q \\ f_0 \end{bmatrix} \tag{2.35a}$$

$$\boldsymbol{f}_{abc} = \begin{bmatrix} f_a \\ f_b \\ f_c \end{bmatrix} \tag{2.35b}$$

In Park's transformation [20], the term $T$ is given by

$$T = \frac{2}{3}\begin{bmatrix} \cos\theta & \cos(\theta - \frac{2\pi}{3}) & \cos(\theta - \frac{4\pi}{3}) \\ -\sin\theta & -\sin(\theta - \frac{2\pi}{3}) & -\sin(\theta - \frac{4\pi}{3}) \\ \frac{1}{2} & \frac{1}{2} & \frac{1}{2} \end{bmatrix} \tag{2.36}$$

where

$$\theta = \int \omega dt \tag{2.37}$$

is the instantaneous rotor electrical angular position. In the above equations the variable $f$ can represent voltage, current, flux or electric charge variables [19]. For example one can have

$$\begin{bmatrix} i_d \\ i_q \\ i_0 \end{bmatrix} = T \begin{bmatrix} i_a \\ i_b \\ i_c \end{bmatrix} \tag{2.38}$$

Under balanced conditions the $0-$axis components are zero. Hence only the $d-$ and $q-$axis components are usually considered in machine analysis. Applying this transformation to the stator winding flux linkage equations in Equation (2.28) and field winding flux linkage in Equation (2.33) gives

$$\lambda_d = L_d i_d + M_{fd} i_{fd} \tag{2.39a}$$

$$\lambda_q = L_q i_q \tag{2.39b}$$

$$\lambda_{fd} = \frac{3}{2} M_{fd} i_d + L_{fd} i_{fd} \tag{2.39c}$$

where, from Appendix A.1:

- $L_d = L_{aa0} + L_{ab0} + \frac{1}{2}L_{aa2} + L_{ab2}$ is the stator d-axis self inductance
- $L_q = L_{aa0} + L_{ab0} - \frac{1}{2}L_{aa2} - L_{ab2}$ is the stator q-axis self inductance
- $L_{fd} = l_{ffd}$ is the rotor d-axis self inductance
- $M_{fd} = L_{afd}$ is the stator-rotor d-axis mutual inductance

Similarly transforming the voltage Equations (2.27a through 2.27c) for stator windings and Equation (2.32) for the field winding to the rotor synchronous frame results (Refer to Appendix A.1)

$$v_d = \frac{d}{dt}\lambda_d - \omega\lambda_q + R_a i_d \tag{2.40a}$$

$$v_q = \frac{d}{dt}\lambda_q + \omega\lambda_d + R_a i_q \tag{2.40b}$$

$$v_{fd} = \frac{d}{dt}\lambda_{fd} + R_{fd} i_{fd} \tag{2.40c}$$

where new reference frame currents $i_d$ and $i_q$ in the above equations are given by Equation (2.38). The resulting flux and voltage expressions in this new reference frame are now rotor angle independent providing a more convenient form for analysis.

### Power and Torque

The instantaneous power into the stator of the motor is given by the expression:

$$P_t = v_a i_a + v_b i_b + v_c i_c \tag{2.41}$$

In terms of the dq-axis variables, assuming the motor operates under balanced conditions, i.e. $v_0 = i_0 = 0$, the power into the motor can be written as:

$$P_t = \frac{3}{2}\left(v_d i_d + v_q i_q\right) \tag{2.42}$$

Using the expressions in Equations (2.40) for $v_d$ and $v_q$ and substituting in Equation (2.42) we have:

$$P_t = \frac{3}{2}\left[\left(i_d\frac{d\lambda_d}{dt} + i_q\frac{d\lambda_q}{dt}\right) + \left(\lambda_d i_q - \lambda_q i_d\right)\omega + \left(i_d^2 + i_q^2\right)R_a\right] \tag{2.43}$$

The terms inside the first parenthesis describe the rate of change of armature energy, the second parenthesis contains the expression related to the power transferred through the air gap, while the remaining expression is related to the armature resistance loss. Thus, the air gap torque can be obtained by dividing the air gap power to the rotor mechanical rotational speed $\omega_{mec}$.

$$T_e = \frac{3}{2}(\lambda_d i_q - \lambda_q i_d)\frac{\omega}{\omega_{mec}} \tag{2.44}$$

$$= \frac{3}{2}(\lambda_d i_q - \lambda_q i_d)\frac{P}{2} \tag{2.45}$$

where $P$ is the number of poles. Substituting

$$\lambda_d = L_d i_d + M_{fd} i_{fd} \tag{2.46}$$

$$\lambda_q = L_q i_q \tag{2.47}$$

in Equation (2.45) gives:

$$T_e = \frac{3}{2}\frac{P}{2}\, i_q\left[\left(L_d - L_q\right) i_d + M_{fd} i_{fd}\right] \tag{2.48}$$

Thus, Equations (2.39) for stator and field windings flux linkage, Equation (2.40) and Equation (2.48) for machine torque along with Equation (2.38) for stator current transformation describe (model) the electromagnetic dynamics of a salient pole synchronous machine in terms of the $dq0$ frame components.

## 2.4 Physical Network Modeling

As it will be apparent in the results, despite the impressive representation of the actual motor behavior, the COMSOL Multiphysics® FEM based model has one big limitation: the fact that it requires a large amount of computing power to simulate. Moreover to that, designing drive control systems is difficult within the COMSOL Multiphysics® environment. The analytical model based on the equations derived in the previous section requires a closed form solution for the field winding current $i_{fd}$ which can be difficult under normal operating conditions. Thus another modeling option that can potentially replace this FEM based model and convenient for MATLAB®/Simulink® simulation purposes is required. This is where the physical network based modeling approach in Simscape™ comes in handy.

Simscape™ software is a set of block libraries and special simulation features for modeling physical systems in the Simulink® environment. In Simulink each block represents a basic mathematical operation. Connecting Simulink blocks together gives the equivalent mathematical model of the system under design. Simscape, however, provides the network representation of the system using the Physical Network approach. The approach is particularly suited to modeling and simulating systems consisting of real physical components [22].

According to this approach, a given system is considered as consisting of functional elements whose interaction with each other is decided by exchanging energy through their connection ports. These connection ports mimic physical connections between elements and are nondirectional. Connecting Simscape elements together is similar to the way real components are connected. That means, a given Simscape system diagram is just like the actual physical system network layout. If physical components modeled by the elements can be connected, their models can be connected, too. Specifying variable flow directions is not required when connecting Simscape blocks, just as one does not have to specify this information when connecting real physical components. The Physical Network approach automatically resolves all the traditional issues with variables, directionality, using its **through variable (TV)** and **across variable (AV)** concept.

The number of connection ports for each element is determined by the number of energy flows it exchanges with other elements in the system, and depends on the level of idealization. A given energy flow is characterized by its across and through variables. Usually, the product of these two variables is the rate of energy flow in watts. These variables are commonly called the basic, or conjugate variables.

**Through** variables that are measured with a gauge connected in series to an element.

**Across** variables that are measured with a gauge connected in parallel to an element.

If the element shown in Figure 2.5 is oriented from connection port $A$ to connection port $B$, it implies that the TV is positive if it "flows" from port $A$ to port $B$, and the AV is determined as $AV = AV_A – AV_B$, where $AV_A$ and $AV_B$ are the element node potentials or, in other words, the values of this AV at connection ports $A$ and $B$, respectively.

Under the assumptions, three types of energy flow exchanges occur for the motor considered in this thesis. Two flows of electrical energy associated with the three phase stator supply and the field winding rectifying diode, and a flow of mechanical energy associated with the rotational

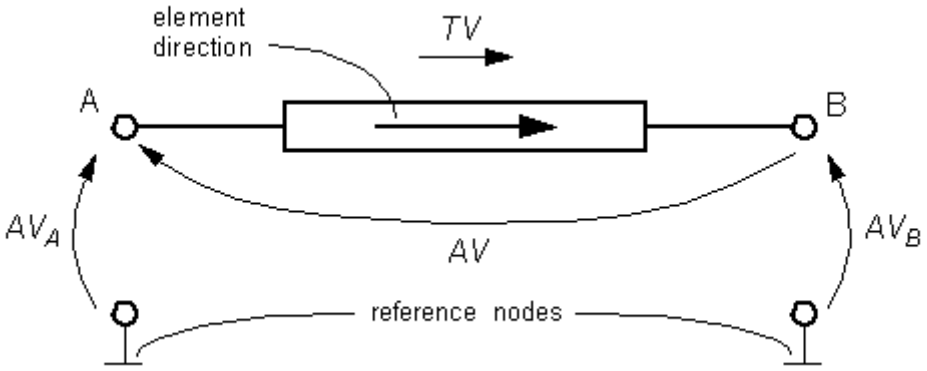


Figure 2.5: Simscape element Across and Through variables, taken from [22]

motion of the rotor. The basic variables for mechanical rotational systems are torque and angular velocity and for electrical systems, they are current and voltage.

For the motor considered here, the mechanical energy exchange is described using a torque through variable and an angular velocity across variable. Port $A$ in Figure 2.5 is the stator and port $B$ is the rotor. Positive torque flows from stator to rotor while positive angular velocity direction is defined from reference node to the stator or rotor ports. The reference node in this case is the stator case or chasis. Thus, the angular velocity for the stator will be zero while for the rotor is the actual rotor velocity.

## 2.5 Related Works

Two-dimensional finite element analysis was used to study a new type of half-wave rectified brushless synchronous motor with permanent magnet in [5] to characterize the flux distribution and torque characteristics. The analysis showed that the field flux of this is kept constant and it was possible to assume that the motor is excited by a DC current similar to a conventional synchronous motor. The authors also showed in their analysis that the flux density produced by the permanent magnet in the radial direction was concentrated around the magnetic poles and that the flux produced by the half-wave rectified excitation was distributed sinusoidally.

The authors in [6] proposed a salient pole type half-rectified brushless motor and described its principle of operation. After a mathematical analysis of the motor equations and experimental verification of the results, the paper suggested the use of triangular modulating waveform over sinusoidal waveform. They also recommended to reduce the values of the leakage coefficient and the q-axis-to-d-axis inductance ratio as much as possible by using salient type rotor design, which effectively reduces the d-axis air gap. The paper demonstrated that reduction in bias frequency reduced the power factor of the motor. Finally, the paper concluded by pointing out that the exciting current and the torque current can be calculated only by detecting the rotor position and that the proposed control scheme makes it possible to control the torque over a much wider speed range from zero (including position control) to full speed than is the case with the vector control of an induction motor. It was clear from the analysis that the characteristics of the proposed motor are little affected by parameter variations caused by the temperature rise.

The work in [7] experimentally investigated the effect of load conditions and speed command values on the fundamental output characteristics such as voltage, current and efficiency. The influence of the variable filed flux on those fundamental characteristics was also considered. The result reported in the paper showed that peak efficiency in different output power ranges varied for different effective excitation current values. The paper also showed that motor efficiency did not depend on the rotor speed and that it decreased with increasing output power. It was shown that it is possible to get the maximum efficiency by choosing the optimal effective excitation current for each output power range.

The authors in [8] presented a similar work to those in [7] in that it involved the experimental investigation of the influence of the variable field flux on the torque and efficiency behavior of the proposed motor. They finalized their paper by stating that armature current decreased with increasing effective value of the excitation current, that efficiency increased with increasing output torque, that field current increased with increasing effective excitation current and was hardly affected by bias frequency of rotor speed.

In [9], a half-wave rectified brushless self-excited synchronous motor with a special design idea different from the previously discussed was explored. The paper specifically focused on a balanced three-phase rotor winding with its own rectifying circuit. The motor proposed in this work uses a static magnetic field, produced on the stator winding by a diode inserted to the stator winding and that induces a fundamental frequency ac voltage in the field winding which in turn is rectified to supply a dc field current. This motor behaved like a series dc motor. The motor also showed better operating performance and capacity than induction motors of the same size. With the voltage source inverter designed by the researchers it was possible to control the speed of the motor economically and reliably.

In [23] the influence of the variable field flux on the motor torque and efficiency characteristics was evaluated. By simulating the equations describing the motor to analyze the fundamental characteristics of a prototype design, the authors found out that the average torque produced by the motor was influenced by the field flux and that this torque had its peak value in a specific range of the excitation current values. The result also showed that torque ripple increased in proportion to exciting current. The influence of the bias frequency on the average torque and the torque ripple was also examined in this paper. Furthermore, variation of the motor efficiency with respect to excitation current and frequency ratio was investigated which showed that efficiency decreases with increasing frequency ratio.

The effect of different rotor designs on the torque characteristics of the proposed motor was investigated in [24], with special focus on optimizing the rotor design for better performance. Specifically, the sizes of Tip and Root of the claw type, rotor field winding turn number, and rotor core shape were considered in the analysis. The average motor torque was observed to peak at specific value of the sizes of the Tip and Root. The rotor winding turn number also affected both the average torque and torque ripple in a direct fashion. These two pairs of torque were also shown to be affected by the other rotor design parameters like Shoe, Yoke and RootT values. 3D finite element analysis (three dimensional (3D) FEM) was used to conduct the analysis and reach the above conclusions.

Most of the previously mentioned researches focused only on a specific aspect of motor design and its effect on the performance of the motor. In this thesis a general analytical model to predict the

motor's performance and behavior verified by an FEM model is presented. The models formulated here are applicable to any motor with a triangular superimposed d-axis current form of excitation.

# Chapter 3

# Methodology

## 3.1 Modeling Approach

In this chapter three types of modeling approaches that are used to study the behavior of the motor are discussed. The first approach involves the use of the FEM method to represent the electromagnetic aspects of the motor plus additional physics implementations for representing other physical aspects. COMSOL Multiphysics® is used for this purpose. The second approach is based on the simplified magnetic circuits concept. From insights obtained from the COMSOL FEM model and some simplifying assumptions, closed form analytical equations were derived. The third model is a MATLAB®/Simulink® environment implementation of the magnetic circuits equations. This model is built using the Simscape™ modeling language based on the physical network approach. Figure 3.1 shows the relationship between the developed models.

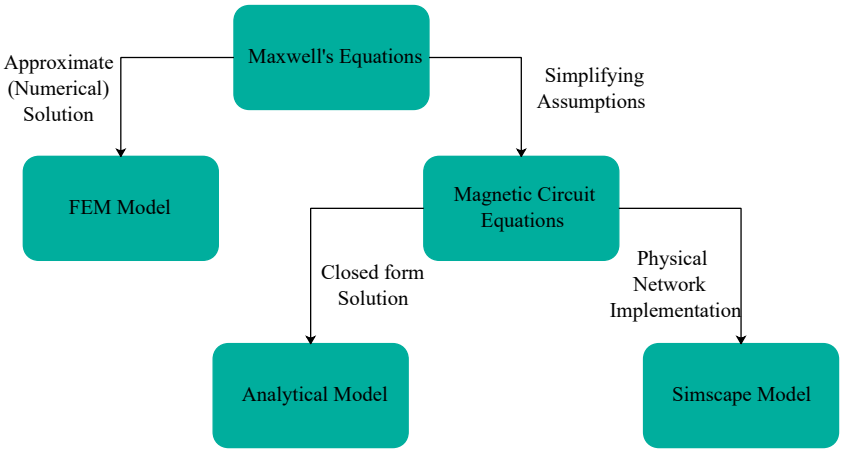


Figure 3.1: Model Relationship

## 3.2 Finite Element Method (FEM) model

COMSOL Multiphysics is a powerful interactive simulation environment used to model and solve a number of scientific and engineering problems. The software provides a powerful integrated

desktop environment. With COMSOL Multiphysics one can easily extend conventional models for one type of physics into multiphysics models that solve coupled physics phenomena — and that do so simultaneously [25]. Generally, the following steps are followed in modeling and simulating a multiphysics system in the COMSOL Multiphysics® environment.

### 3.2.1 Spatial Dimension

3D models require large memory space and bigger computational power, which would be difficult to satisfy with the computing resource used in this thesis. 2D FEM analysis of the motor is used in COMSOL Multiphysics. Assuming that fringing and end winding effects can be neglected, planar symmetry (or xy symmetry) can be used to reduce the actual 3D problem to a 2D problem. In this symmetry the magnetic phenomena are assumed to be identical on each plane (x, y) normal to the z-axis. The **Out-of-plane thickness** parameter value within the **Rotating machinery magnetic (rmm)** physics interface is set to the actual length of the rotor in the 3D geometry. The interface takes care of the 3D effects based on this parameter.

### 3.2.2 Geometry

The motor topology used for the FEM analysis is shown in Figure 3.2. Both the stator and rotor were designed with $8$ poles. The stator is consists of $48$ slots with distributed winding arrangement of $2$ slots per pole per phase. The power rating of this motor was selected to be $7.5\,kW$ while the rated torque is $60\,Nm$. Using those values as a starting point and performing the design using a method modified from the approach used in [26, 27] (see Appendix D), the geometrical prameters needed for the design can be generated, see Table 3.1.

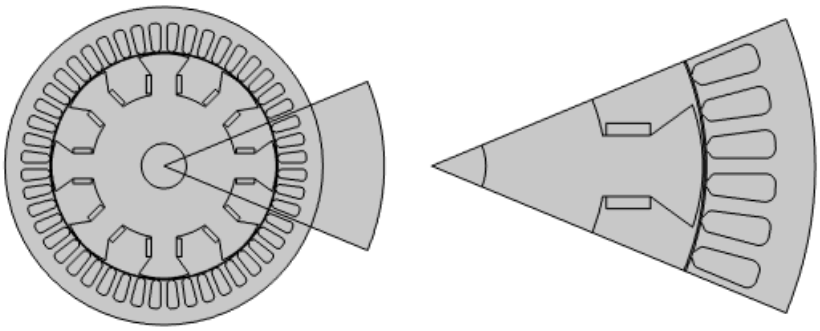

(a) Full geometry (b) Simulated geometry

Figure 3.2: FEM Model Geometry

Large and complex geometries require huge amount of memory and bigger computational resources, hence longer solution time, than smaller and simpler ones. Thus, during FEM analysis it is customary to simplify and reduce the model using different approaches without sacrificing accuracy. One such approach is the use of symmetry. From the symmetric behavior of the model, one can see that simulating only one-eighth of the total model can provide the necessary information to predict the characteristic of the whole model.

Table 3.1: Basic geometrical parameters

| Parameter | Value | Unit |
|---|---|---|
| Stator core outer diameter | 225 | mm |
| Stator core inner diameter | 161.2 | mm |
| Maximum stator slot width | 8.6569 | mm |
| Minimum stator slot width | 6.2454 | mm |
| Stator slot height | 20.052 | mm |
| Stator tooth thickness | 4.5214 | mm |
| Stator yoke height | 11.874 | mm |
| Air gap length | 1.05 | mm |
| Motor axial length | 239.1 | mm |
| Rotor outer diameter | 159.1 | mm |
| Rotor inner diameter | 101.8 | mm |
| Rotor axle diameter | 31.8 | mm |
| Maximum rotor tooth width | 35.8 | mm |
| Minimum rotor tooth width | 17.896 | mm |
| Rotor tooth height | 44.636 | mm |
| Pole span of rotor | 36.6 | mm |

### 3.2.3 Material Assignment

After the geometry has been built, the next step is to assign materials for the model. This stage of the modeling process defines the constitutive relations in terms of the material properties. Four types of materials have been used in this thesis, see Figure 3.3.

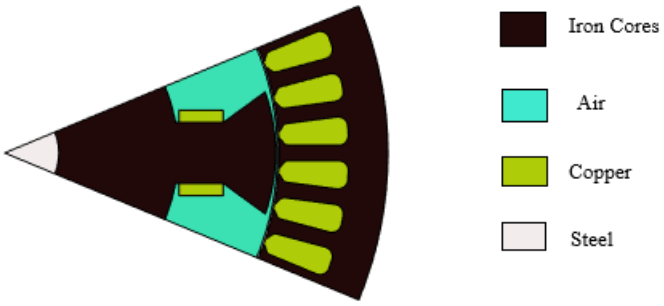


Figure 3.3: Materials assigned to the model

The material properties that are relevant for study of the model for these four materials are provided in the table below (Table 3.2). In the table the electric and magnetic properties of the materials are shown. The electrical property of the domains used for modeling the winding is given

using electrical conductivity and relative permittivity. The electrical conductivity value used for the soft iron core is zero since it is lossless (soft) [28]. Electrical permittivity is used to model the constitutive relation in Equation (2.2b). For low frequency electromagnetic problems, the electric displacement **D** is usually assumed to be negligible which allows freedom for the choice of the relative permittivity value in Equation (2.2b).

Table 3.2: Basic properties of the materials used [28], [29], [30]

| **Material** | **Air** | **Soft Iron** | **Copper** | **Steel** |
|---|---|---|---|---|
| Electrical Conductivity $(S/m)$ | 0 | 0 | $5.998e7$ | $4.032e6$ |
| Relative Permeability | 1 | B-H curve | 1 | 1 |
| Relative Permittivity | 1 | 1 | 1 | 1 |

The magnetic properties of the Air, Steel, and Copper are modeled using the relative permeability parameter, while the corresponding property for the soft iron is computed from the B-H curve of the actual material shown in Figure 3.4. Copper relative permeability values are around 1 as in [31]. Steel was used as the axial material for its mechanical properties, not for its magnetic properties. Any other material with similar mechanical properties can be used. Thus, the use of the relative permeability $\mu_r = 1$ for steel is justified. In fact, the value provided for $\mu_r$ is obtained from the COSMSOL software materials library, [28]. For example, austenitic steels which are classified as paramagnetic with relative permeabilities approaching 1.0 (generally in the range of 1.003 to 1.05 in the fully annealed condition) can be used for such applications [30].

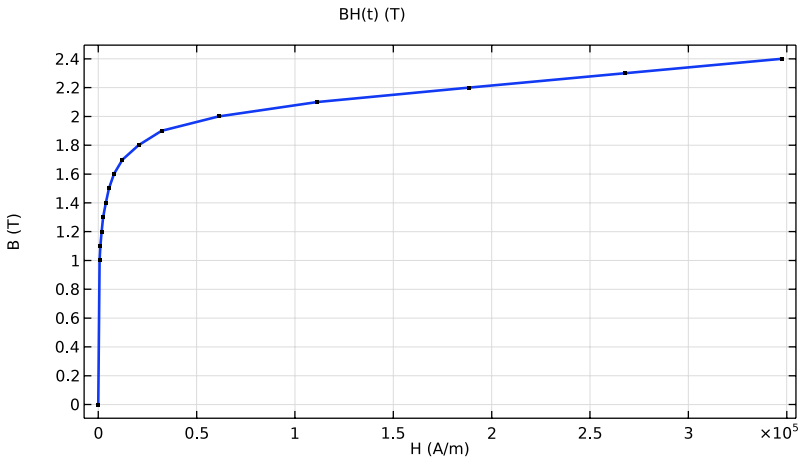


Figure 3.4: B-H curve of the soft iron core used in the model, [29]

### 3.2.4 Physics

Defining the physics involves the process of setting up all the physical equations that should be solved in order to determine the model's behavior. For the motor studied in this thesis, the following

physics interfaces were defined:

1. Rotating Machinery, Magnetic (rmm) physics
2. Electrical circuit (cir) physics
3. Global ordinary differential equation (ODE) and differential algebraic equation (DAE) physics

### Rotating Machinery, Magnetic (rmm)

This physics interface solves Maxwell's equations formulated using a combination of magnetic vector potential and magnetic scalar potential as the dependent variables [15]. In the former approach a vector field $\boldsymbol{A}$, is introduced and the approach defines the magnetic flux density and the electric field as in Equations (2.6a) and (2.6b). In the scalar potential formulation a scalar potential $V_m$ is introduced where the magnetic field is defined as the gradient of this potential.

The two formulations can be used together by combining the vector potential formulation for conductive or current-carrying domains and the scalar potential formulation for the air gap and nonconductive domains. This approach is referred to as mixed formulation. The mixed formulation approach is particularly useful for 3D models. For 2D models the discretization scheme is same for both the vector potential and potential, hence the use of mixed formulation is not necessary. Within the Rotating Machinery, Magnetic (**rmm**) interface node the following additional nodes are included, all of which are formulated using the vector potential approach:

1. The **Electric Field Transformation** node imposes suitable transformations to the electric field definitions in all the domains depending on rotor rotational velocity.

2. **Ampere's Law** (Equation (2.1b)) which is the vector potential formulation is applied to the Air, Steel and Iron core domains of the model. The constitutive relations described in equations (2.2a)-(2.2c) are applied based on the material property the respective domain is assigned to, i.e. using the relative permeability and permittivity for the Air, Steel and coil Copper domains and the B-H curve in Figure 3.4 for the Iron cores in the stator and rotor.

3. The **Coil** node is used to model coils, cables and other conductors subject to a lumped excitation, such as an externally applied current or voltage. This feature transforms this lumped excitation into local quantities (electric field and electric current density), and computes lumped parameters of interest such as impedance, and inductance [15]. The winding arrangement used in this thesis is three-phase, single layer, distributed winding with 2 slots per pole per phase. According to this, each stator slot domain in Figure 3.5a represents a single coil side of the stator winding. Excitation to the coils can be provided as current, voltage or power. Current excitation is used in this thesis due to its simplicity. Positive signs represent reference out-of-plane current direction while the negative signs represent the reverse. The feature the generates the current density vector $\boldsymbol{J}$ for the coil domains shown in the figure. $\boldsymbol{J}$ for this 2D problem has only $z-$ direction, i.e. $\boldsymbol{J} = [0,\ 0,\ J_z]$.

4. The following set of boundary conditions were applied in the modeling process, see Figure 3.5b.

   **Magnetic Insulation** feature takes care of the magnetic field boundary conditions at the outer periphery of the stator core implemented using Equation (2.7d) in which $\boldsymbol{B_2} =$

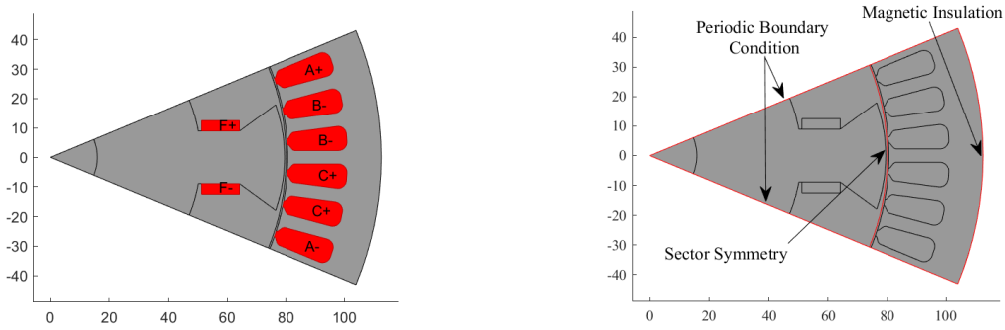


(a) Model domains used for coils

(b) Boundary conditions

Figure 3.5: Physics assignment

0. This sets the normal component of the magnetic flux density at this boundary to zero.

**Periodic Boundary Conditions** are also applied to the symmetry cut boundaries of the sector model, both for the stator and rotor parts. For the vector (Ampere's Law) and scalar potential formulations, the following conditions are set at the boundaries $\Gamma_1$ and $\Gamma_2$

$$\boldsymbol{A}_{\Gamma_1} = \pm \boldsymbol{A}_{\Gamma_2} \tag{3.1a}$$

$$V_{\Gamma_1} = \pm V_{\Gamma_2} \tag{3.1b}$$

The plus sign is used when there is even periodicity, i.e., each sector is the same, while the negative sign is used when when there is anti-periodicity (odd periodicity), i.e., change sign in adjacent sectors. The latter form is used here since alternating north and south poles of the motor introduce anti-periodicity.

**Sector Symmetry** condition was applied to the boundary between the stator and rotor in the middle of the air gap. The feature couples the dependent variables on the two sides to make sure that the same formulation is used on either side.

5. Using the Maxwell's stress tensor method described in Section 2.2.1, the **Force Calculation** feature computes the electromagnetic force (torque) on a given domain in the model (rotor in this case).

With the problem defined this way, the **rmm** physics interface then solves for the magnetic vector potential variable **A**. Quadratic discretization was used in which the dependent variable **A** is approximated by a linear combination of second order polynomial interpolating functions.

### Electrical Circuit (cir)

In COMSOL Multiphysics an electrical circuit element can be modeled in one of the following two ways:

- Using field model (FEM) to get a better, more accurate description of the element in the electrical circuit model.
- Using the **cir** interface to model the element to drive or terminate components (especially windings) in the field model in such a way that the field model and circuit model can be simulated both as a tightly coupled system.

The **Electrical Circuit** interface makes it possible to add nodes representing circuit elements directly to the Model Builder tree in a COMSOL Multiphysics model. The circuit variables can then be connected to a physical device model to perform co-simulations of circuits and the field model to give a multiphysics problem. The model acts as a device connected to the circuit so that its behavior is analyzed in larger systems. The fundamental equations solved by the **Electrical Circuit** interface are Kirchhoff's circuit laws, which in turn can be deduced from Maxwell's equations [15].

The diode that short circuits the field winding along with the appropriate connections to this winding is modeled using this physics interface. In this interface the diode is behavior is described using the large signal model, in which the relationship between the voltage across the diode $v_{fd}$ and current $i_{fd}$ is determined by an exponential equation, Equation (3.2) [15]. **External I Vs. U** feature is used to connect the diode in **cir** physics to the rotor coil in **rmm** physics.

$$i_{fd} = I_S \left( e^{\frac{v_{fd}}{NV_T}} - 1 \right) \frac{1}{\sqrt{1 + \frac{I_S}{I_{KF}} \left( e^{\frac{v_{fd}}{NV_T}} - 1 \right)}} \tag{3.2}$$

where $I_S$ is the saturation current, $N$ is ideality factor, $V_T$ is junction thermal voltage, $I_{KF}$ is corner for high-current roll-off.

### Global ODEs and DAEs, Global Equation (GE)

Using this interface global space-independent equations that represent additional states in the model can be represented. For the motor considered, these states are the rotor angular speed and position. Mechanical dynamics of the rotor is modeled using this block. It is implemented using the COMSOL Multiphysics® **Global ODEs and DAEs, Global Equation (ge)** interface. This block is a simplified representation of Newton's second law of motion relating the angular velocity $\omega_{mec}$ with the electromagnetic torque $T_e$, rotor inertia $J_r$ and rotational damping $B_r$. Additionally, the rotor angular position $\theta_{mec}$ is determined from the angular velocity variable.

$$\frac{d\omega_{mec}}{dt} = \frac{T_e - T_{load} - B_r\omega_{mec}}{J_r} \tag{3.3a}$$

$$\frac{d\theta_{mec}}{dt} = \omega_{mec} \tag{3.3b}$$

## 3.2.5 Meshing

Although COMSOL Multiphysics® provides a physics-controlled meshing capability that automaticaly meshes the geometry based on the applied physics, user-controlled meshing is preferred here. This gives the user a greater degree of control on the meshing process. It is preferred to

mesh the model geometry separately [32]. Specifically, the boundary between the stator and rotor (half-way in the air gap) should be meshed very carefully. To accurately map field quantities from source[1] to destination [2] boundaries in the identity pair (a pair of boundaries in relative motion with each other), there needs to be a finer mesh on the destination side (rotating boundary) than on the source side (stationary boundary), see Figure 3.6. The boundaries at the cut edges of the sector were also meshed using identical settings to provide accurate application of periodic boundary conditions. The remaining 2D regions within the problem domain were meshed with triangular elements.

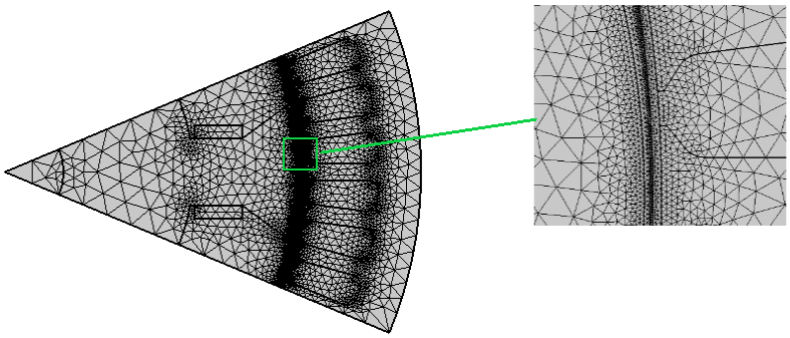

Figure 3.6: Mesh plot of the sector model used in simulation

Finer mesh elements were also used for curved geometric entities. The complete mesh consists of 14155 domain elements and 1704 boundary elements.

### 3.2.6 Solver Settings

Two types of studies are performed for this model: stationary and time dependent. Stationary studies provide the electromagnetic behavior of the motor for specific values of excitation current supplied to the stator coils. The result from this study will then be used as an initial condition for the time dependent study.

The following dependent variables are formulated during the time dependent solution process

1. Magnetic vector potential, $A_z$
2. Rotor angular speed, $\omega_{mec}$
3. Diode currents and voltage $i_{diode}$, $v_{diode}$

The time dependent problem is highly non-linear. Each time step is solved by a Newton-Raphson iterative non-linear solver. Convergence is reached when the difference between successive values of the solution and the independent variable are below a certain value referred to as the tolerance setting of the iterative solver. The iteration stops if such convergence is achieved or the maximum number of iterations specified for the solver is reached. If the solution does not converge after the specified number of iterations, the solver stops computing and error message will be reported.

[1] Stator side of the boundary
[2] Rotor side of the boundary

### 3.2.7 Post Proccessing

The solution to the field problem is the value of the magnetic vector potential $\boldsymbol{A}$ at each node of the mesh network. The current density in this case has only z- direction component. Consequently, the magnetic vector potential $\boldsymbol{A}$, which is parallel to $\boldsymbol{J}$ has components $\boldsymbol{A} = [0,\ 0,\ A_z]$. From this information, the magnetic flux density $\boldsymbol{B}$, flux linkage $\lambda$, for instance can be computed from Equations (2.6a) and (2.12), respectively. Other required characteristics of the model, like coil voltages, power, and so on can also be extracted from the solution.

### 3.2.8 COMSOL Model Structure

The hierarchy of all the above model components and their interactions to give the whole motor model is shown in the block diagram in Figure 3.7.

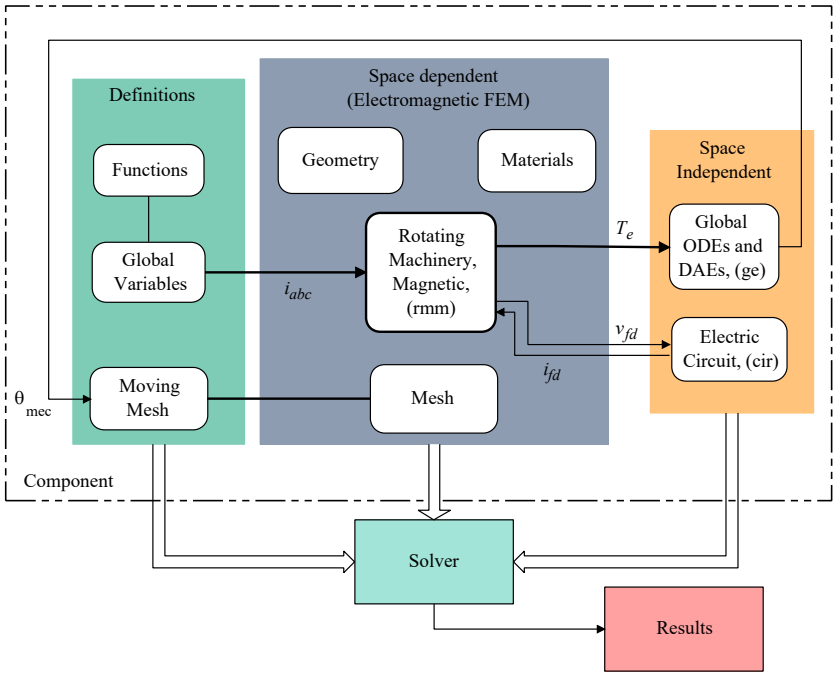


Figure 3.7: COMSOL FEM model structure

The figure shows that there are five main components of the model. The **Definitions** part of the model defines various features that are applied to the model. These features include global variables, functions, mass properties and general coordinate transformations. In this thesis, a set of globally defined variables are used to represent the current source for the coils. Using the **Functions** feature, desired kinds of stator supply current waveforms can be defined. The **Moving Mesh** feature applies coordinate transformations to the mesh to reflect the spatial displacement caused by rotor motion.

The FEM based electromagnetic block consists of the space dependent part of the the model. It is the only part of the overall motor model in which FEM is used to determine its behavior. In it are the actual motor geometry, material assignment, **Rotating Machinery, Magnetic, (rmm)** physics, and mesh. The current excitation for the stator coils is provided by the variables defined

in the **Defnitions** node. The excitation for the field winding, however, is provided by the current computed using the **Electric Circuits (cir)** physics interface. The interface calculates this current using Equation (3.2), where the voltage for the diode is voltage induced in the winding. This voltage across the winding is computed using **Maxwell's** equations. This way the electromagnetic part and the circuits part are coupled.

## 3.3 Analytical Model of the Motor

In order to predict the capabilities of the motor and estimate its limitations, simplified explicit input-output analytical expressions are required. Analytical models allow the exploration of the whole search space of solutions while reducing the pre-design stages duration. Especially in drive control design, power, torque and voltage characteristics of the motor for the whole range of operation speed is needed. This can be extracted from the circuits based model of the motor. To do this, the works of [6] are extended to find analytical framework that can be used as a basis for the purpose of performance analysis and FEM model verification.

### 3.3.1 Principle of Operation

#### Structure of the Motor

The stator of the motor has basically the same construction as the conventional three phase synchronous or induction motors. Three coils are arranged in symmetrical positions displaced by 120 electrical degrees, see Figure 3.8. The rotor of the motor has a salient pole structure with the field winding short circuited by a diode.

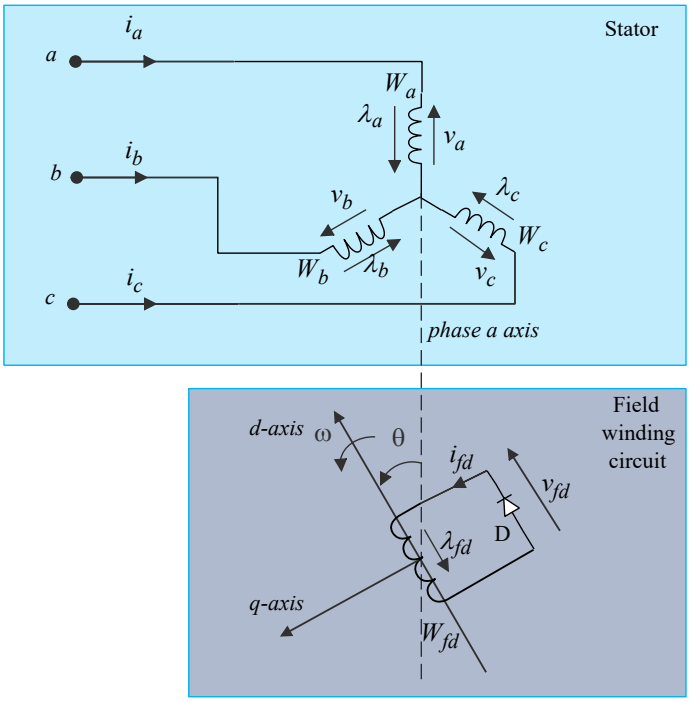


Figure 3.8: Motor configuration

The stator coils carry a balanced three-phase current producing a magnetic field of constant magnitude rotating at a constant angular velocity $\omega$. Additionally, an amplitude modulated three-phase current with a modulating waveform of frequency $f_b$ is added to the normal three-phase current. This additional modulated current will produce a magnetomotive force which rotates at synchronous speed and alternating at angular frequency $2\pi f_b$. The field winding is excited by the current induced by the oscillating d-axis component of the stator current which will then be rectified resulting a unidirectional current in the field winding. This unidirectional current can now provide the magnetomotive force required to produce field winding flux without the use of permanent magnets or external field current supplied through brushes.

### Excitation and Principle of Torque Generation

The three-phase current supplied to the stator winding of this specific motor is as given in Equation (3.4).

$$i_a(t) = A_f(t)\cos\theta - I_t \sin\theta \tag{3.4a}$$

$$i_b(t) = A_f(t)\cos(\theta - \frac{2\pi}{3}) - I_t \sin(\theta - \frac{2\pi}{3}) \tag{3.4b}$$

$$i_c(t) = A_f(t)\cos(\theta - \frac{4\pi}{3}) - I_t \sin(\theta - \frac{4\pi}{3}) \tag{3.4c}$$

where $\theta$ is the rotor electrical angular position in radians given by Equation (2.37).

The first term on the right side of these equations generates a synchronously rotating pulsating waveform $A_f(t)$. This waveform can be of any type although the most common ones are triangular, sinusoidal and trapezoidal. It has a peak value of $I_f$ and (bias) frequency $f_b$. Triangular waveform is preferred over the others for its better performance in terms of average field winding flux linkage and power factor of the motor [6]. The second term on the right side of those equations is the usual three-phase current that generates the constant magnitude rotating magnetomotive force (mmf) at rotor synchronous electrical speed $\omega$. Its peak value is $I_t$, see Figure 3.9.

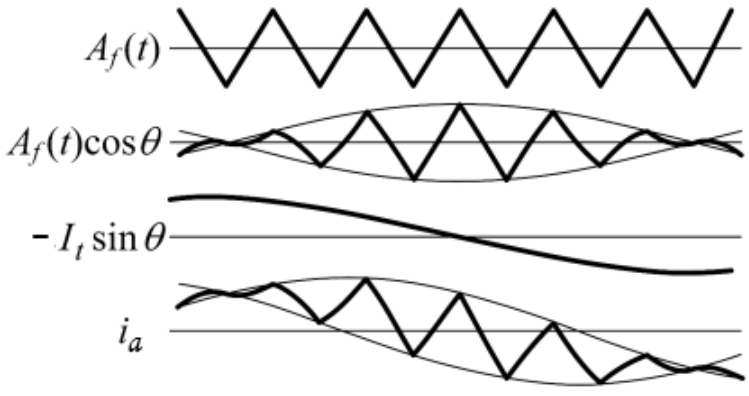


Figure 3.9: Stator phase current waveforms, taken from [23]

Transforming the three-phase currents in Equation (3.4) to rotor synchronous reference frame with $dq0$ axes using Park's coordinate transformation provided in Equation (2.38) gives the fol-

lowing expressions for the reference frame dq-axis current variables.

$$i_d = A_f(t) \tag{3.5a}$$

$$i_q = I_t \tag{3.5b}$$

Under balanced operation conditions in which $i_a + i_b + i_c = 0$, the 0-axis current $i_0$ is equal to zero. The transformed dq-axis equivalent circuit can now be represented as shown in Figure 3.10.

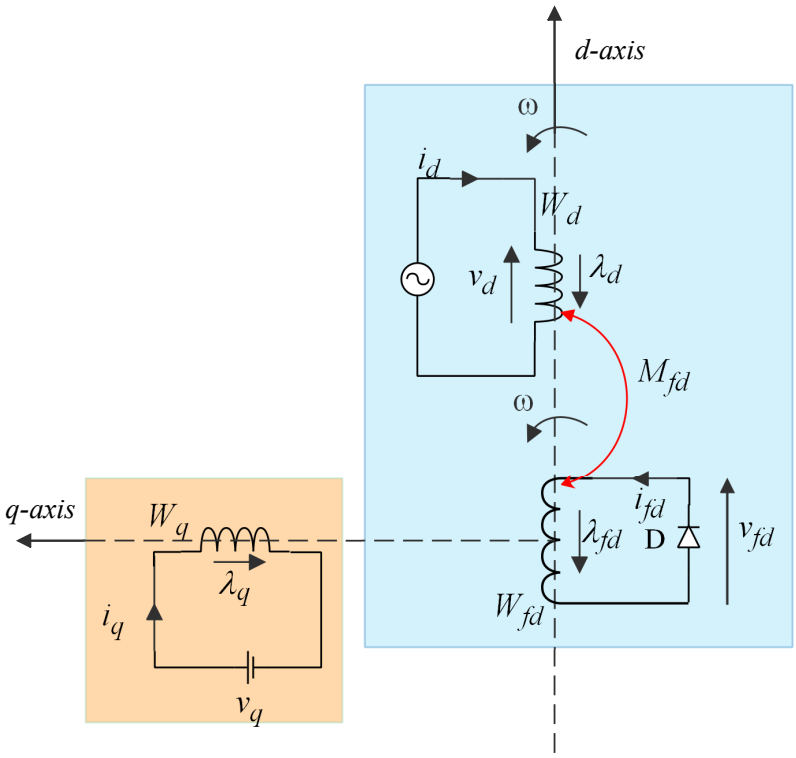


Figure 3.10: Motor principle of operation

From Figure 3.10, it can be seen that the stator d-axis winding $W_d$ and field winding $W_{fd}$ are coupled through the stator-rotor mutual d-axis inductance term $M_{fd}$. The pulsating current $i_d$, generates a pulsating MMF in the d-axis. This pulsating MMF links both the stator d-axis winding $W_d$ and field winding $W_{fd}$. The variation of this MMF induces the field winding voltage, $v_{fd}$, in $W_{fd}$ causing current to flow. This in turn, by the action of the diode, results in the generation of a uni-directional (DC) current in the field winding. The synchronously rotating q-axis winding, $W_q$, is excited by the q-axis current component, $i_q$.

The field winding current $i_{fd}$ depends on a number of aspects including motor design parameters (inductances and resistances), field excitation current component amplitude $I_f$ and bias frequency $f_b$. Explicit expression for the field winding current $i_{fd}$ is necessary in order to clearly describe the motor. $i_{fd}$ is caused by the interaction of the stator d-axis circuit and the rotor (field) winding circuit. The equivalent circuit representing this interaction taken from Figure 3.10 is shown in Figure 3.11.

The circuit has two distinct operating states: Diode ON and Diode OFF. Assuming an ideal diode, the two states for the above d-axis equivalent circuit can be represented as shown in Figure 3.12.

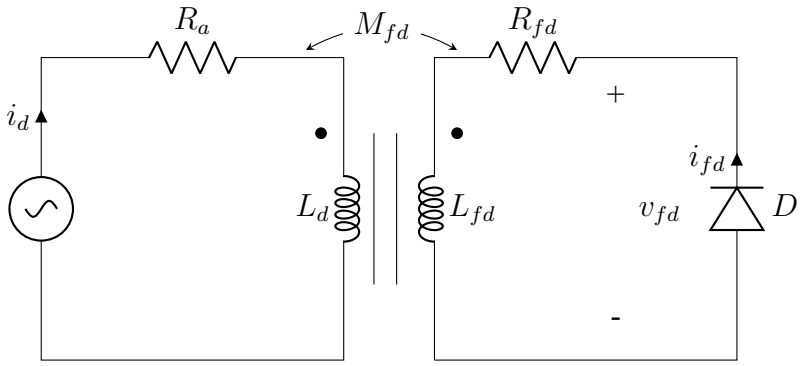


Figure 3.11: Simplified d-axis equivalent circuit

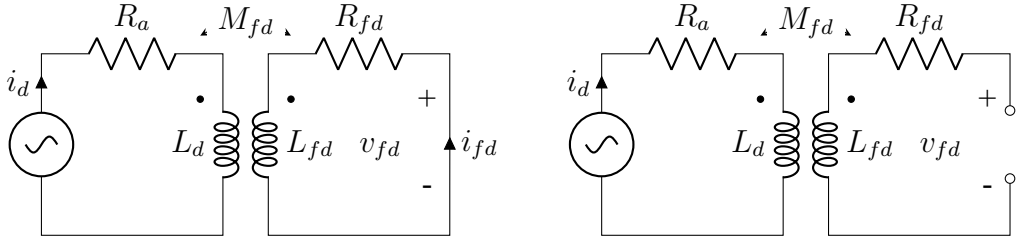


(a) Diode ON (b) Diode OFF

Figure 3.12: Two modes of operation of the equivalent circuit

The current $i_d$ is controlled by the inverter supplying the stator and is kept to have the desired kind of waveform, amplitude, and frequency. In our case the traingular waveform has been chosen based on the data from previous literature [6]. Mathematically, $i_d$ is described by the piecewise function given in Equation (3.6). In the equation, $I_f$ is the amplitude and, $T_b$ is the period, respectively, of the triangular waveform $A_f(t)$ in Equations (3.4a - 3.4c).

$$i_d(t) = \begin{cases} \dfrac{-4I_f}{T_b}\, t + I_f & \text{for } 0 \leq t \leq \dfrac{T_b}{2} \\ \\ \dfrac{4I_f}{T_b}\, t - 3I_f & \text{for } \dfrac{T_b}{2} < t \leq T_b \end{cases} \tag{3.6}$$

Figure 3.13 shows the plot of this current waveform for three full period intervals.

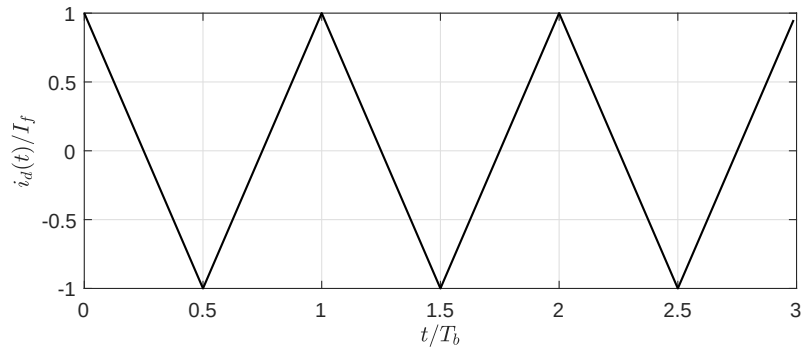


Figure 3.13: D-axis current waveform

To find the expression for the rotor current $i_{fd}$ during the time the diode is conducting, we can apply Kirchhoff's voltage law (KVL) for the circuit in question. Deducing from Figure 3.12a the following equation can be written.

$$v_{fd} = 0 \tag{3.7}$$

Substituting

$$v_{fd} = \frac{d}{dt}\,\lambda_{fd} + R_{fd} i_{fd} \tag{3.8}$$

where

$$\lambda_{fd} = \frac{3}{2} M_{fd} i_d + L_{fd} i_{fd} \tag{3.9}$$

in Equation (3.7) and rearranging gives a linear ODE of the form

$$\frac{d}{dt}\,i_{fd}(t) + \frac{R_{fd}}{L_{fd}}\,i_{fd}(t) = -\frac{3}{2}\frac{M_{fd}}{L_{fd}}\,\frac{d}{dt}\,i_d(t) \tag{3.10}$$

Equation (3.10) has to solved for $i_{fd}(t)$ for the whole period of the the d-axis current $i_d(t)$. The method of integrating factors can be used to find the solution for ODEs of this type [33]. This solution can be written as

$$\frac{d}{dt}\left(i_{fd}(t)e^{P(t)}\right) = Q(t)e^{P(t)} \tag{3.11}$$

where

$$P(t) = \int \frac{R_{fd}}{L_{fd}}dt = \int \frac{1}{T_0}dt = \frac{t}{T_0} \tag{3.12}$$

$$Q(t) = -\frac{3}{2}\frac{M_{fd}}{L_{fd}}\,\frac{d}{dt}\,i_d(t) \tag{3.13}$$

Here, the parameter $T_0 = \dfrac{L_{fd}}{R_{fd}}$ is the time constant of the RL circuit of the field winding inductor-resistor combination. $Q(t)$ in Equation (3.13) can have the following form depending on the time interval.

$$Q(t) = \begin{cases} \dfrac{3}{2}\dfrac{M_{fd}}{L_{fd}}\dfrac{4I_f}{T_b} & \text{for } 0 \le t \le \dfrac{T_b}{2} \\[2ex] -\dfrac{3}{2}\dfrac{M_{fd}}{L_{fd}}\dfrac{4I_f}{T_b} & \text{for } \dfrac{T_b}{2} < t \le T_b \end{cases} \tag{3.14}$$

where

$$\frac{d}{dt}i_d(t) = \pm\frac{4I_f}{T_b} = \pm 4I_f f_b \tag{3.15}$$

The solution for Equation (3.11) is given by

$$\left(i_{fd}(\tau)\,e^{\frac{\tau}{T_0}}\right)\Big|_{t_0}^{t} = \int_{t_0}^{t} Q(\tau)\,e^{\frac{\tau}{T_0}}\,d\tau \tag{3.16}$$

For the interval $0 \le t \le {}^{T_b}/_{2}$, using the expression for $Q(t)$ in that interval from Equation (3.14), in which $t_0 = 0$ and $i_{fd}(t_0) = i_{fd}(0) = 0$, one can have the following for $i_{fd}$

$$i_{fd}(t)\,e^{t/T_0} - i_{fd}(0)\,e^{0/T_0} = \int_0^t \frac{3}{2}\frac{M_{fd}}{L_{fd}}\frac{4I_f}{T_b}\,e^{\tau/T_0}d\tau \tag{3.17}$$

which when simplified gives the following general expression for $i_{fd}$

$$i_{fd}(t) = 4\left(\frac{T_0}{T_b}\right)\left(\frac{3}{2}\frac{M_{fd}}{L_{fd}}\right) I_f \left(1 - e^{-t/T_0}\right) \tag{3.18}$$

A more useful form of Equation (3.18) can be obtained by defining

$$r = {}^{T_0}/_{T_b} \tag{3.19}$$

r is the ratio of the R-L circuit time constant to bias period. This parameter determines the time at which the rotor current $i_{fd}$ decays to zero during the second half of the full period of the excitaion waveform.

$$i_{fd}(t) = 4r\left(\frac{3}{2}\frac{M_{fd}}{L_{fd}}\right) I_f \left(1 - e^{-t/T_0}\right) \tag{3.20}$$

Using a similar approach, the expression for $i_{fd}$ in the second interval i.e $\frac{T_b}{2} < t \leq T_b$ can be found by solving Equation (3.11) in this interval as follows

$$\left(i_{fd}(\tau)\, e^{\tau/T_0}\right)\Big|_{T_b/2}^{t} = \int_{T_b/2}^{t} Q(\tau)\, e^{\tau/T_0} d\tau \tag{3.21}$$

which gives

$$i_{fd}(t) = 4r\left(\frac{3}{2}\frac{M_{fd}}{L_{fd}}\right) I_f \left(2e^{1/2r - t/T_0} - e^{-t/T_0} - 1\right) \tag{3.22}$$

In this interval the current starts from a maximum value and decays to zero. To find the time $t_1$ at which this current becomes zero, one can solve the equation

$$2e^{1/2r - t_1/T_0} - e^{-t_1/T_0} - 1 = 0 \tag{3.23}$$

which gives

$$t_1 = T_0 \ln\left(2e^{1/2r} - 1\right) \tag{3.24}$$

Further simplification by dividing both sides of Equation (3.24) by $T_b$ gives

$$\frac{t_1}{T_b} = \frac{T_0}{T_b}\ln\left(2e^{1/2r} - 1\right) = r\ln\left(2e^{1/2r} - 1\right) \tag{3.25}$$

Equation (3.25) describes how the OFF time of the circuit (Diode) depends on the parameter $r$. A plot of the ratio $\frac{t_1}{T_b}$ versus $r$ is shown below (see Figure 3.14)

The figure shows that for small values of $r$, i.e low frequency excitation while $T_0$ is held fixed, the diode turns off immediately after the half period interval $t = {}^{T_b}/_2$. On the other hand, if $r$ is large enough, the circuit diode remains conducting for nearly the whole period. This behavior has significant effect on a number of motor characteristics such as induced field winding current, field winding flux linkage, average and ripple torque produced at the rotor, as shown in the next sections.

In general

$$i_{fd} = \begin{cases} 4r\left(\frac{3}{2}\frac{M_{fd}}{L_{fd}}\right) I_f \left(1 - e^{-t/T_0}\right) & \text{, for } 0 \leq t \leq \frac{T_b}{2} \\ 4r\left(\frac{3}{2}\frac{M_{fd}}{L_{fd}}\right) I_f \left(2e^{1/2r - t/T_0} - e^{-t/T_0} - 1\right) & \text{, for } \frac{T_b}{2} < t \leq t_1 \\ 0 & \text{, for } t_1 < t \leq T_b \end{cases} \tag{3.26}$$

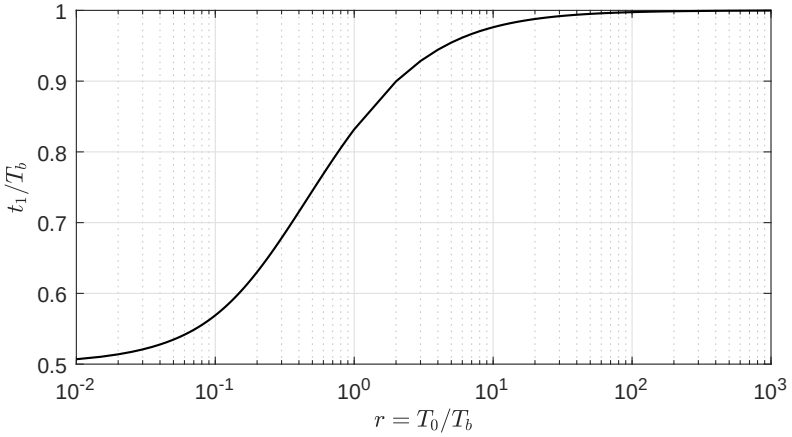


Figure 3.14: Variation of Diode OFF time for different $r$ values

The effect the value of $r$ has on the induced rotor current $i_{fd}$ and rotor flux linkage $\lambda_{fd}$ is depicted in Figure 3.15 for three cases. In the figure, the value of $r$ was set to $0.1$, $1$ and $100$ keeping all the other parameters constant. The vertical broken lines show the instant the diode turns from ON to OFF. As one can observe from the figure, the field winding flux linkage approaches to a more constant value, while the current resembles triangular waveform instead of exponential one, for large values of $r$.

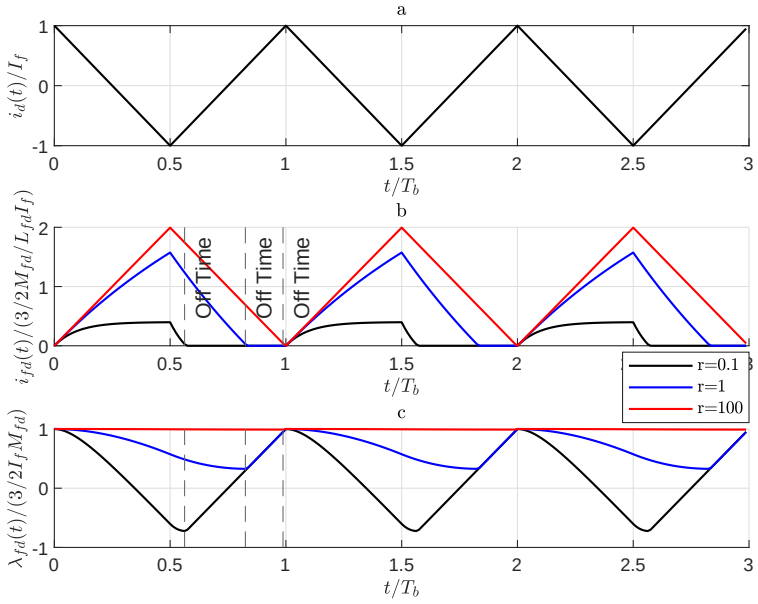


Figure 3.15: Variation of current and flux waveforms for different $r$

From Equation (3.19) one can easily that

$$r = T_0 f_b = \frac{L_{fd}}{R_{fd}} f_b \tag{3.27}$$

where $f_b$ is the bias frequency. High values of $r$ would mean high bias frequency $f_b$. However, there is an upper limit on $f_b$ decided by many factors such as iron loss limits, inverter capacity,

controller bandwidth, etc. Thus, a good choice for the minimum value of $r$ should be at least $50$ (see Figure 3.14) with the upper limit depending on the design and performance requirements.

### Power and Torque

Substituting the expressions for $i_d$ and $i_{fd}$ in Equations (3.6) and (3.26) into Equation (2.48), one can have

$$T_e(t) = \frac{3}{2}\frac{P}{2} i_q I_f T_{esub}(t) \tag{3.28}$$

where $T_{esub}(t)$ is given by:

$$T_{esub}(t) = \begin{cases} \dfrac{-4(L_d - L_q)}{T_b} t + 6r\dfrac{M_{fd}^2}{L_{fd}} \left(1 - e^{-t/T_0}\right) + (L_d - L_q) & \text{, for } 0 \le t \le \dfrac{T_b}{2} \\ \dfrac{4(L_d - L_q)}{T_b} t + 6r\dfrac{M_{fd}^2}{L_{fd}} \left(2e^{1/2r} e^{-t/T_0} - e^{-t/T_0} - 1\right) & \\ -3(L_d - L_q) & \text{, for } \dfrac{T_b}{2} < t \le t_1 \\ (L_d - L_q)\left(\dfrac{4}{T_b} t - 3\right) & \text{, for } t_1 < t \le T_b \end{cases} \tag{3.29}$$

The average torque generated by the motor can be found by integrating the Equation (3.28) over the whole period of the waveform $T_e(t)$, i.e.

$$T_{avg} = \frac{1}{T_b}\int_0^{T_b} T_e(t)dt = \left(\frac{3}{2}\right)\left(\frac{P}{2}\right) i_q I_f \left(\frac{1}{T_b}\right)\int_0^{T_b} T_{esub}(t)dt \tag{3.30}$$

where the integral $\displaystyle\int_0^{T_b} T_{esub}(t)dt$ can be calculated as

$$\int_0^{T_b} T_{esub}(t)dt = \int_0^{\frac{T_b}{2}} T_{esub}(t)dt + \int_{\frac{T_b}{2}}^{t_1} T_{esub}(t)dt + \int_{t_1}^{T_b} T_{esub}(t)dt \tag{3.31}$$

in which

$$\int_0^{\frac{T_b}{2}} T_{esub}(t)dt = 6r\left(\frac{M_{fd}^2}{L_{fd}}\right)\left(\frac{T_b}{2} - T_0 + T_0 e^{-1/2r}\right) \tag{3.32}$$

$$\begin{aligned}\int_{\frac{T_b}{2}}^{t_1} T_{esub}(t)dt = {} & (L_d - L_q)\left[T_b - 3t_1 + 2\frac{t_1^2}{T_b}\right] \\ & + 6r\left(\frac{M_{fd}^2}{L_{fd}}\right)\left[\frac{T_b}{2} - t_1 - T_0\left(e^{-1/2r} - e^{-t_1/T_0} + 2e^{1/2r}e^{-t_1/T_0}\right)\right]\end{aligned} \tag{3.33}$$

and

$$\int_{t_1}^{T_b} T_{esub}(t)dt = -(L_d - L_q)\left[T_b - 3t_1 + 2\frac{t_1^2}{T_b}\right] \tag{3.34}$$

Thus, adding Equations (3.32) through (3.34), and noting that

$$2e^{1/2r - t_1/T_0} - e^{-t_1/T_0} - 1 = 0$$

from Equation (3.23) gives

$$\int_0^{T_b} T_{esub}(t)dt = 6r\left(\frac{M_{fd}^2}{L_{fd}}\right)(T_b - t_1) \tag{3.35}$$

Finally we will have,

$$T_{avg} = \left(\frac{3}{2}\right)\left(\frac{P}{2}\right) i_q I_f \left(\frac{M_{fd}^2}{L_{fd}}\right) 6r\left(\frac{1}{T_b}\right)(T_b - t_1) \tag{3.36}$$

which using Equation (3.25) gives

$$T_{avg} = \left(\frac{3}{2}\right)^2\left(\frac{P}{2}\right) i_q I_f \left(\frac{M_{fd}^2}{L_{fd}}\right) 4r\left(1 - r\ln\left(2e^{1/2r} - 1\right)\right) \tag{3.37}$$

In equation (3.37), the term $4r\left(1 - r\ln\left(2e^{1/2r} - 1\right)\right)$ detemines the magnitude of the average torque $T_{avg}$ for different values of $r$. The following figure shows the variation of this term as a function of the parameter $r$.

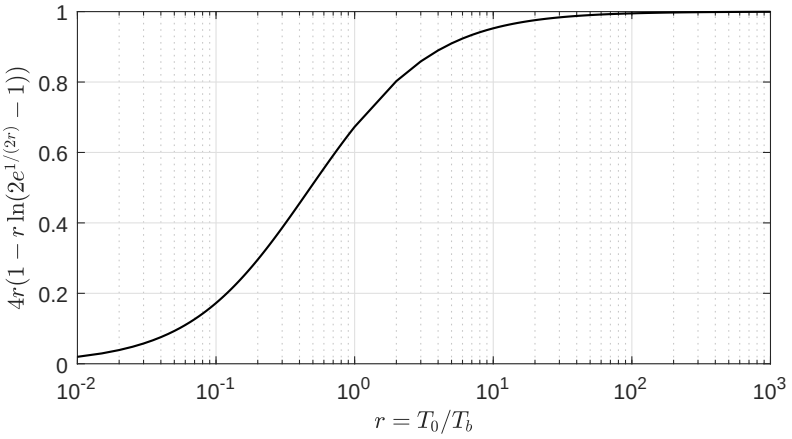


Figure 3.16: Variation of average torque factor for different $r$

Deriving a general analytical expression for the ripple torque just like the one done for the average torque is cumbersome. However, a simple trick can be used to arrive at a relatively accurate expression for the ripple torque. From Figure 3.15, it can be observed that for large values of $r$ the $i_{fd}$ waveform is almost a triangular wave similar to $i_d$. Mathematically, the relationship between $i_d$ and $i_{fd}$ can be expressed as:

$$\frac{i_{fd}(t)}{I_f \frac{3}{2}\frac{M_{fd}}{L_{fd}}} \approx -\frac{i_d(t)}{I_f} + 1 \tag{3.38}$$

which when rearranged gives

$$i_{fd}(t) \approx I_f\left(\frac{3}{2}\frac{M_{fd}}{L_{fd}}\right) - \left(\frac{3}{2}\frac{M_{fd}}{L_{fd}}\right) i_d(t) \tag{3.39}$$

Substituting Equation (3.39) into Equation (2.48) for $i_{fd}$ and neglecting the approximation sign, we have

$$T_e = \frac{3}{2}\frac{P}{2} i_q I_f \left(\frac{M_{fd}^2}{L_{fd}}\right)\left[\frac{3}{2} + \left((L_d - L_q) - \frac{3}{2}\frac{M_{fd}^2}{L_{fd}}\right)\frac{i_d(t)}{I_f}\right] \tag{3.40}$$

Equation (3.40) can be separated to two terms representing the average and ripple torque as:

$$T_{avg} = \left(\frac{3}{2}\right)^2 \frac{P}{2} i_q I_f \left(\frac{M_{fd}^2}{L_{fd}}\right) \tag{3.41}$$

$$T_{rip}(t) = \frac{3}{2}\frac{P}{2} i_q I_f \left((L_d - L_q) - \frac{3}{2}\frac{M_{fd}^2}{L_{fd}}\right) \frac{i_d(t)}{I_f} \tag{3.42}$$

Equation (3.41) is identical to Equation (3.37) for large values of $r$. The peak-to-peak variation of the ripple torque, $T_{rip}$, is given by

$$\begin{aligned} \Delta T_{rip} &= T_{rip,max} - T_{rip,min} \\ &= \frac{2}{3}\left[\frac{(L_d - L_q)}{\frac{Mfd^2}{L_{fd}}} - \frac{3}{2}\right]\left(\left(\frac{i_d(t)}{I_f}\right)_{max} - \left(\frac{i_d(t)}{I_f}\right)_{min}\right) \end{aligned} \tag{3.43}$$

The term $i_d(t)/I_f$ in Equation (3.43) varies between 1 and $-1$ as shown in Figure 3.15. Hence, $T_{rip}$ will have its maximum value when this term is 1 and minimum value when the term is $-1$. The ratio of the peak-to-peak ripple torque to the the average torque, (or ripple factor, $R_{rip}$) can be expressed as:

$$R_{rip} = \frac{\Delta T_{rip}}{T_{avg}} = \frac{4}{3}\left[\frac{(L_d - L_q)}{\frac{Mfd^2}{L_{fd}}} - \frac{3}{2}\right] \tag{3.44}$$

Small $R_{rip}$ requires $L_d > L_q$ which implies salient rotor topology.

### Voltage and Current Limits

Above the rated speed of the motor, the stator voltage increases without limit unless it is regulated using flux weakening techniques. Thus, to analyze the high speed performance of the motor, the voltage and current limit conditions must be clearly described. In terms of the reference frame dq axis variables, the current and voltage limits are given by:

$$i_d^2 + i_q^2 \leq I_{s\_max}^2 \tag{3.45a}$$

$$v_d^2 + v_q^2 \leq V_{s\_max}^2 \tag{3.45b}$$

where $I_{s\_max}$, and $V_{s\_max}$ are the maximum stator current and voltage values obtained from the rating of the machine.

The current limit condition specifies the allowable combination of d-axis and q-axis currents based on thermal and other constraints. Equation (3.45a) describes an area surrounded by a circle of radius $I_{s\_max}$ centered at $(0, 0)$ in the dq-axes coordinates, see Figure 3.17. In addition, the d-axis current of the motor is limited as $-I_f \leq i_d \leq I_f$. This limit is shown by the two vertical lines $i_d = -I_f$ and $i_d = I_f$ as shown in the figure. Thus, resulting current limit area will be determined by the intersection of the area inside circle and area between the these two vertical lines (shaded area in Figure 3.17).

The voltage $V_{s\_max}$ in Equation (3.45b) is the maximum output voltage of the inverter driving the motor. From Equation (2.40), neglecting the stator resistance voltage drops, one can have

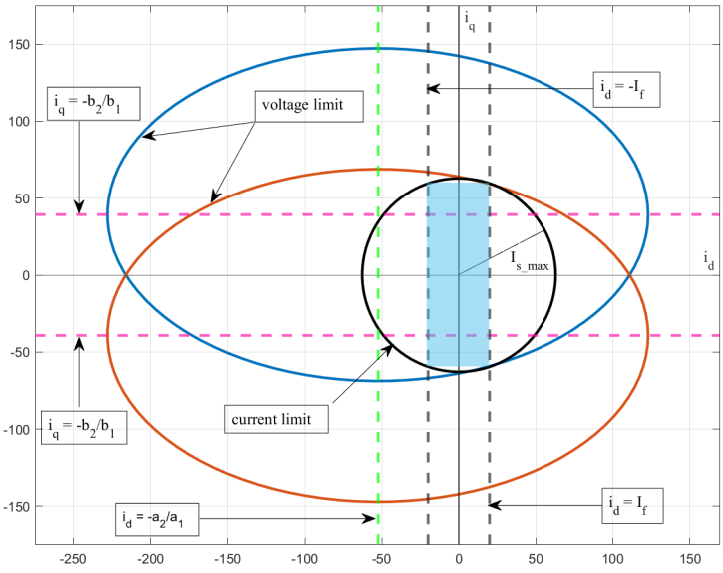


Figure 3.17: Current and voltage limit curves

$$v_d = \frac{d}{dt}\lambda_d - \omega\lambda_q + R_a i_d \approx \frac{d}{dt}\lambda_d - \omega\lambda_q \tag{3.46a}$$

$$v_q = \frac{d}{dt}\lambda_q + \omega\lambda_d + R_a i_q \approx \frac{d}{dt}\lambda_q + \omega\lambda_d \tag{3.46b}$$

Under steady-state conditions, $\frac{d}{dt}\lambda_q = 0$. Using Equation (2.39) for flux linkages in which $i_{fd}$ is given by Equation (3.39), and simplifying gives

$$\left(\frac{i_d + {}^{a_2}/_{a_1}}{{}^{V_{s\_max}}/_{a_1}}\right)^2 + \left(\frac{i_q + {}^{b_2}/_{b_1}}{{}^{V_{s\_max}}/_{b_1}}\right)^2 \leq 1 \tag{3.47}$$

where

$$a_1 = \omega\left(L_d - \frac{3}{2}\frac{M_{fd}^2}{L_{fd}}\right) \tag{3.48a}$$

$$a_2 = \omega\left(\frac{3}{2}\frac{M_{fd}^2}{L_{fd}} I_f\right) \tag{3.48b}$$

$$b_1 = -\omega L_q \tag{3.48c}$$

$$b_2 = \left(L_d - \frac{3}{2}\frac{M_{fd}^2}{L_{fd}}\right)\frac{d}{dt} i_d \tag{3.48d}$$

Equation (3.47) is the equation of an ellipse with the following geometrical parameters:

- center at

$$\left(-\frac{a_2}{a_1}, -\frac{b_2}{b_1}\right) = \left(\frac{3}{2} I_f \frac{\frac{M_{fd}^2}{L_{fd}}}{L_d - \frac{3}{2}\frac{M_{fd}^2}{L_{fd}}}, -\frac{1}{\omega L_q}\left(L_d - \frac{3}{2}\frac{M_{fd}^2}{L_{fd}}\right)\frac{d}{dt} i_d\right) \tag{3.49}$$

- length of major axis

$$2a = 2\frac{V_{s\_max}}{a_1} = 2\frac{V_{s\_max}}{\omega\left(L_d - \frac{3}{2}\frac{M_{fd}^2}{L_{fd}}\right)} \tag{3.50}$$

- length of minor axis

$$2b = 2\frac{V_{s\_max}}{b_1} = 2\frac{V_{s\_max}}{\omega L_q} \tag{3.51}$$

The sign of the term $\frac{d}{dt}i_d$ in Equation (3.49) can be both positive and negative as given by Equation (3.15), hence the two ellipses as shown in the figure (Figure 3.17). The intersection of these two ellipses determines the set of all controllable d- and q- axis current combinations satisfying the voltage limit condition (Equation (3.45b)). Therefore, the set of all d- and q-axis current values that are controllable using an inverter of the rated voltage without violating the maximum allowable stator current limit will be those found inside the area determined as the intersection of both the current and voltage limit curves.

From Equations (3.49 through 3.51), it can be seen that the rotor electrical angular speed $\omega$ affects the geometrical parameters of the ellipses. Given a constant voltage $V_{s\_max}$, the length of both the major and minor axes decrease as speed increases. This causes the area covered by the voltage limit ellipses to shrink, which limits the range of controllable d- and q-axis currents. The position of the centers is also changed (see Figure 3.18.) The base speed $\omega_b$ of the motor is the maximum speed at which both the voltage and current limit curves cover the d- and q- axis currents combinations from zero up to the rated stator current $I_{s\_max}$ under the rated voltage $V_{s\_max}$. In this case, for example, $\omega_b = \omega_1$ in the figure.

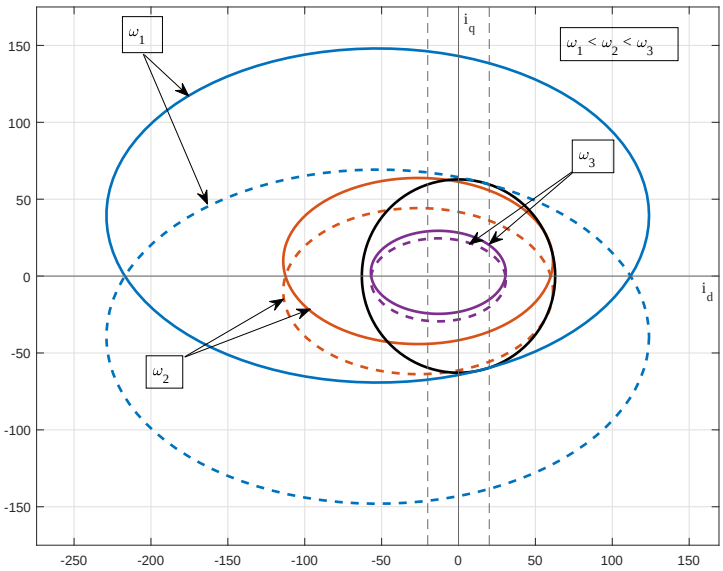


Figure 3.18: Effect of $\omega$ on voltage limit curves

At this speed, the stator voltage reaches the maximum value of $V_{s\_max}$ when supplied with rated stator current. The value of this speed can be determined by solving the equality in Equation

(3.47) for $\omega$ for a given value of $V_{s\_max}$, taking into consideration the intersection of the two ellipses (see Appendix A.2).

$$|\omega_b| = \frac{-8ABI_tI_ff_b + \sqrt{(8ABI_tI_ff_b)^2 - 4\left[B^2I_t^2 + ((A+C)I_f)^2\right]\left[(4AI_ff_b)^2 - V_{s\_max}^2\right]}}{2\left[B^2I_t^2 + ((A+C)I_f)^2\right]} \tag{3.52}$$

where

$$A = L_d - \frac{3}{2}\frac{M_{fd}^2}{L_{fd}} \tag{3.53a}$$

$$B = -L_q \tag{3.53b}$$

$$C = \frac{3}{2}\frac{M_{fd}^2}{L_{fd}} \tag{3.53c}$$

For motor operation above base speed, flux weakening techniques have to be applied to limit the stator voltage to the rated value while increasing the speed. Flux weakening technique is used to limit the back-emf of the motor, which is directly proportional to rotor rotational speed and field winding flux, to a desired level so that the stator voltage does not exceed the available inverter voltage. If the rotor speed is increased above base speed, the field flux has to be reduced by changing the value of $I_f$ of the stator current. Once this value of $I_f$ is chosen, the value of $I_t$ satisfying both the current and especially the voltage limit curves can be calculated from

$$I_t = \frac{4AI_ff_b - \sqrt{V_{s\_max}^2 - (A+C)^2I_f^2\omega^2}}{B\omega} \tag{3.54}$$

where $A$, $B$, and $C$ are as given by Equation (3.53) (refer to Appendix A.3). $I_t$ here is the maximum allowable current component for the given speed. Equation (3.54) is derived taking into consideration the intersection of the voltage limit ellipses.

### Efficiency

One of the main motivations of studying this motor was the promise that the motor offers better efficiency improvement in the flux-weakening region than conventional PMSMs. To see this the efficiency map of the motor for the whole range of operation speeds has to be generated. The efficiency model used for this purpose is given by

$$\eta_m = \frac{P_{out}}{P_{out} + P_{losses}} \tag{3.55}$$

where $P_{out}$ is the average motor output power and $P_{losses}$ is the sum of all the motor losses.

$$P_{out} = T_{avg}\omega_{mec} \tag{3.56}$$

$$P_{losses} = P_{cu} + P_{core} + P_f \tag{3.57}$$

The power loss term consists of the losses caused by stator and rotor winding losses, $P_{cu}$, iron core (hysteresis plus eddy) loss, $P_{core}$ and friction losses, $P_f$, where

$$P_{cu} = 3I_{sRMS}^2 R_a + I_{fdRMS}^2 R_{fd} \tag{3.58}$$

$$P_{core} = P_h + P_e \tag{3.59}$$

$$P_f = T_f \omega_{mec} \tag{3.60}$$

The iron core losses can be combined using the expression above (Equation (3.59)) [34]. Unlike PMSMs, the total copper loss of this motor decreases as the speed of operation increases. This is the result of the reduction in the field excitation current component $A_f(t)$ of the stator supply in the high speed region. Although this is true in general the rate of reduction in copper loss as speed increases differs greatly for different combination of $I_t$ and $I_f$, see Figure 3.19. Optimal selection of this current ratio can be applied to better increase the efficiency of the motor for different operating points, as shown in the figure.

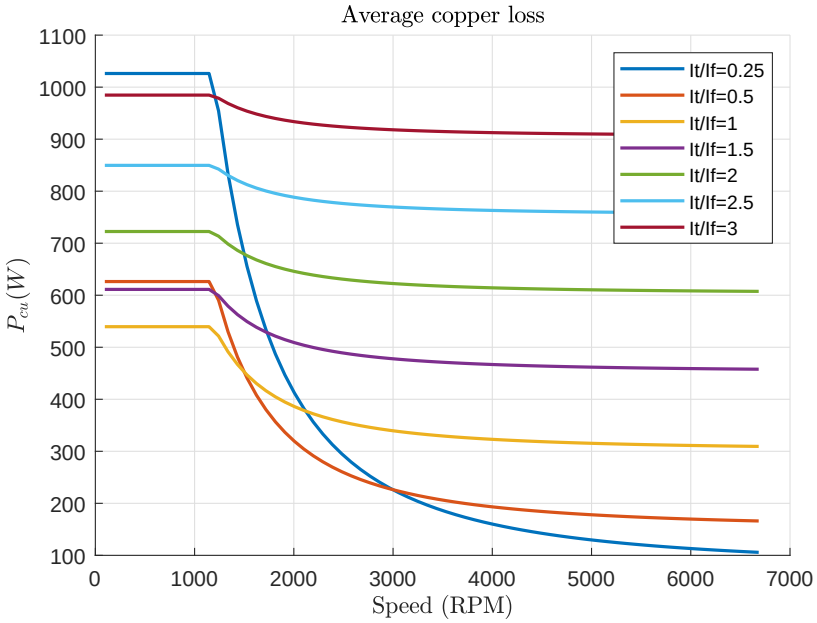


Figure 3.19: Effect of different $\frac{I_t}{I_f}$ values on machine total copper loss

Using a simple field weakening technique where the stator d-axis current component is modified according to the rotor speed, the current terms in Equation (3.58) can be made functions of the mechanical speed $\omega_{mec}$. The hysteresis loss component of the core loss $P_{core}$ is proportional to the rate of change of the magnetic flux density. For sinusoidal excitation the Steinmetz equation is used to calculate the hysteresis loss. The coil excitation in this motor is non-sinusoidal which means the Steinmetz equation cannot directly be used for the hysteresis loss modeling. However, it is safe to assume that the loss is proportional to both the excitation frequency and magnitude of the magnetic flux density. Eddy losses can usually be reduced by using thinner iron core lamination or better materials. Thus, ignoring the eddy losses, Equation (3.55) can have the general form;

$$\eta_m = f(\omega_{mec}) \tag{3.61}$$

Based on this efficiency model, the efficiency maps for different stator current component ratios $I_t/I_f$ can be generated. For $I_t/I_f = 3$, the value used in this thesis, the efficiency map is as shown in Figure 3.20.

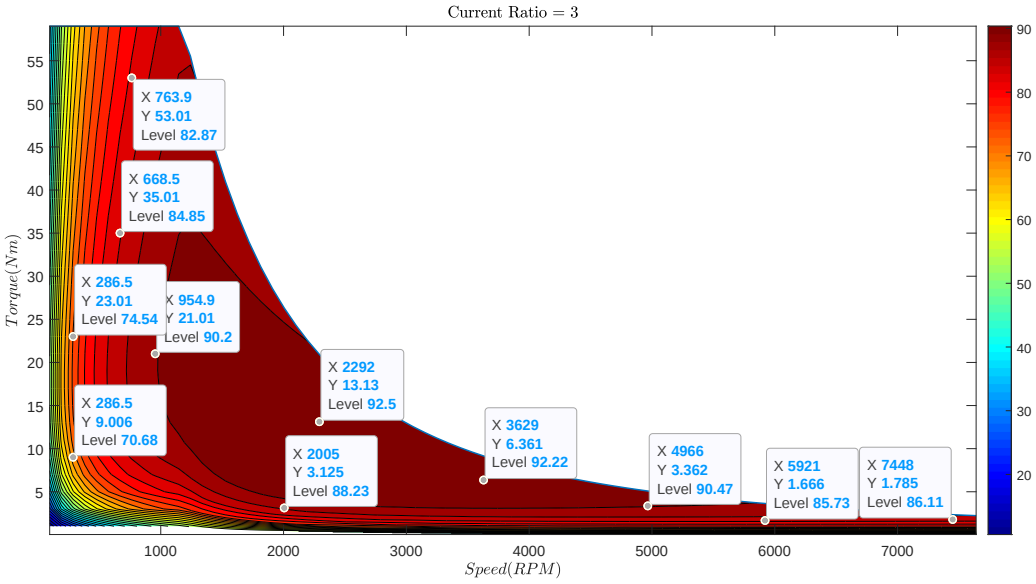


Figure 3.20: Motor efficiency map generated based on analytical model at $280\,V$

From the figure one can observe that, in general, the efficiency of the motor is the higher in the high speed region. For EV traction applications this is essentially desired since EVs spend most of their drive cycle in this operation region.

## 3.4 Simscape Model

Using the physical network approach the motor is modeled as two element device. The first element consists of the entire machine (except the diode shorting the field winding) implemented using the reference frame dq-axes equations. The second element is obviously the diode the model of which is already available in the MATLAB/Simulink Simscape components library. These two elements are connected to give the complete motor model. The single phase electrical energy exchange between the two elements automatically determines the field winding current $i_{fd}$, voltage $v_{fd}$, diode current and voltage.

The implementation and description of part of the Simscape code used in the first element of the model is described below. Detailed explanation of how such code is written can be found at the MATLAB software documentation in [22].

**Component name and description** A given physical device is first defined using the component class. The component is given a specific name along with its description that is displayed on the dialog box of the block. The equations, connection ports, parameters and variables defining the characteristics of the element are included within the scope of this definition

Listing 3.1: Component Definition

```
component HWRRBSM
% Half-Wave Rectified Rotor Brushless Synchronous Motor
% This block models half-wave rectified brushless synchronous motor
% parametrized using constant inductance values. Connect the field winding
% rectifying diode using the 'ef+' and 'ef-' ports
.
.
.
end
```

**Nodes definition** nodes are the external connection ports through which the element block is connected to other systems. They are defined as shown in Listing 3.2. The following syntax defines a given node, *a*.

*package_name.domain_name.a  % label:location*

*package_name* is the full path to the domain, starting with the top package directory and including the subpackages. Simscape provides a collection of packages for different physical systems. The port label and location in the element block are specified as a comment.

Listing 3.2: Node Definition

```
nodes
        N  = foundation.electrical.three_phase;           % ~:left
        R  = foundation.mechanical.rotational.rotational; % R:right
        C  = foundation.mechanical.rotational.rotational; % C:right
        ep = foundation.electrical.electrical;            % ef+:right
        en = foundation.electrical.electrical;            % ef-:right
 end
```

**Branches section** defines the positive direction of flow for each **Through** variable of the element. There are three through variables, two current variables $I$ and $i_{fd}$, and one torque variable.

Listing 3.3: Branch Definition

```
branches
        I      : N.I  -> *;
        if_d   : ep.i -> en.i;
        torque : C.t  -> R.t;
 end
```

The three phase stator supply $I$ flows from the node N to the neutral point '*'. Positive field winding current, $i_{fd}$ is defined as the current flow from the positive terminal of the winding (*node ep*) to the negative terminal (*node en*). From the mechanical systems point of view, the motor is considered as an active element, i.e. it supplies mechanical energy. This implies that the torque through variable flows from port C (stator) to port R (rotor), while the angular velocity across variable is measured as the difference between its value at port R and its value at port C, see Section 2.4 for details.

**Equations section** this section consists of the relationship between the across and through variables describing the energy exchange equations. An intermediate physical system is used in

the transfer of the electrical energy to mechanical energy. This intermediate system is the magnetic system implemented using magnetic flux equations.

Listing 3.4: Equations section

```
equations
    let
            vf_d = ep.v - en.v;
            angular_velocity = R.w - C.w;
            .
            .
            .
    in
            % Electric to mechanical rotation
            angular_velocity == wNominal + angular_position_diff.der;

            % Electrical equations
            vd == lambda_d.der - nPolePairs*angular_velocity*lambda_q + i_d*Ra;
            vq == lambda_q.der + nPolePairs*angular_velocity*lambda_d + i_q*Ra;
             0 == -lambdaf_d.der - Rfd*if_d + vf_d;
             .
             .
             .
            % Mechanical torque
            torque == 3/2*nPolePairs*(lambda_d*i_q - lambda_q*i_d);
    end
end
```

The complete MATLAB® code used for building this model is as shown in listing found in Appendix B.1. From this code, a custom Simscape library component that is just like any other default Simulink/Simscape library component can be generated. The component will be represented by a block with connection ports as described earlier.

The block consists of five external connectinon ports: two for mechanical systems (R and C), two for field winding rectifying diode (*ef*+ and *ef*-), and one electrical three phase port for motor supply (~). The field winding rectifying diode is connected to the model through the (*ef*+ and *ef*-) terminals shorting the field winding of the rotor. The motor block is parametrized using stator and rotor winding inductances and resistances. The inductances are stator d-axis self inductance $L_d$, q-axis self-inductance $L_q$, stator-rotor d-axis mutual inductance $M_{fd}$, and rotor self-inductance $L_{fd}$. Stator phase winding resistance $R_s = R_a = R_b = R_c$ and rotor winding resistance $R_{fd}$ are also required. Mechanical behaviors of the motor like friction, inertia. etc can be modeled using the already built-in mechanical library components and connecting them to the motor model using its mechanical ports.

In this thesis, the piece-wise linear diode model is used for Simulink simulations. This diode model gives the diode current $i_{fd}$ for diode voltage $v_{fd}$ applied across its terminals as [22]:

$$i_{fd}(t) = \begin{cases} \dfrac{v_{fd} - V_f(1 - R_{on}G_{off})}{R_{on}} & \text{for } v_{fd} \geq V_f \\ v_{fd}G_{off} & \text{for } v_{fd} < V_f \end{cases} \tag{3.62}$$

where $V_f$ is the forward bias voltage, $R_{on}$ is the on resistance, $G_{off}$ is the off conductance. The diode model that can be used is not limited to the piece-wise linear.

## 3.5 Controller Design

Field oriented control (FOC) is used to control the motor. The structure of the control drive system is shown in Figure 3.21 below

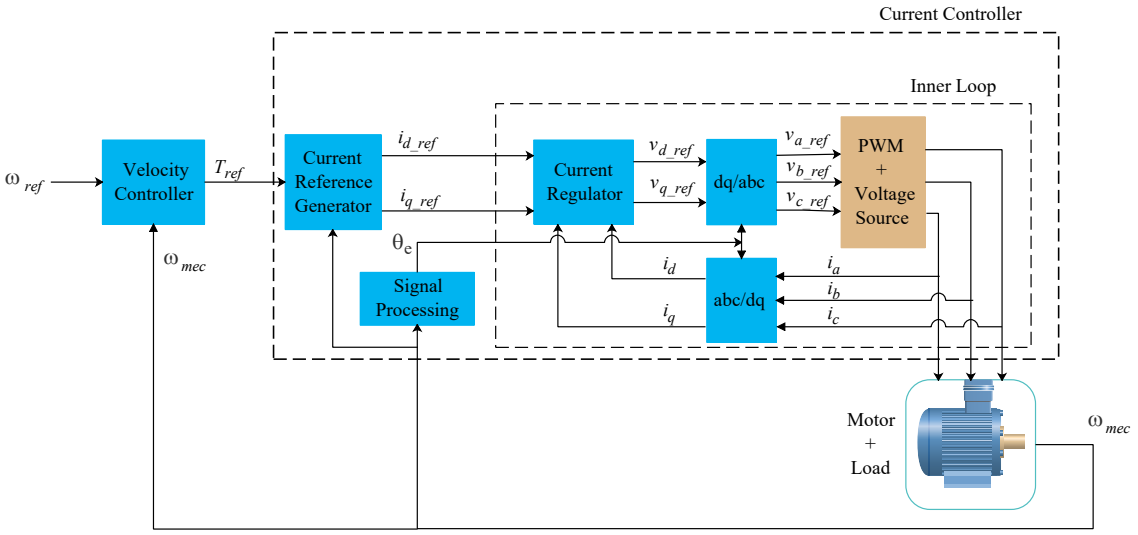


Figure 3.21: Control System configuration

### Velocity Control Loop

The velocity controller block regulates the rotational speed of the motor. The loop consists of the velocity controller proportional integral (PI) block, current controller and motor plus load. The current controller part, shown inside the shaded rectangle in Figure 3.22, consists of the current reference generator and the inner loop. Load torque is included as a disturbance. The output of the inner loop is the resulting motor velocity, $\omega_{mec}$. The velocity controller then uses PI control law to compute the reference torque, $T_{ref}$. The parameters for the PI controller are calculated using the pole placement method.

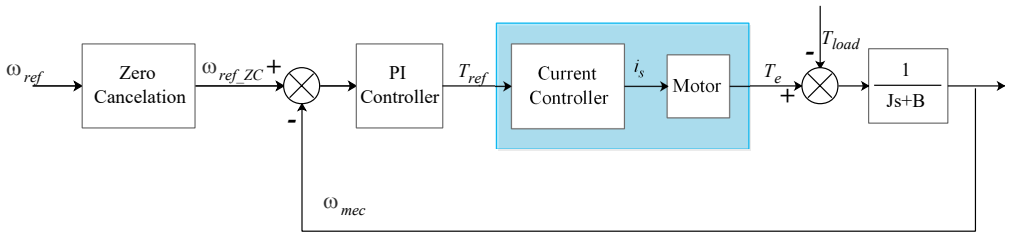


Figure 3.22: Velocity control loop block diagram represention

Considering the general form of closed loop system shown in Figure 3.22 in which the mechanical load is modeled as a first order, the transfer functions of each block will be [35]:

$$G_{PI}(s) = \frac{K_P s + K_I}{s} \tag{3.63a}$$

$$G_M(s) = \frac{1}{J_r s + B_r} \tag{3.63b}$$

where $J_r$ is the motor rotational inertia and $B_r$ is the rotational friction coefficient. Since the current controller loop is run at a much faster sampling frequency than the speed loop, the response of the current loop will have reached steady state between sampling instants of the speed loop. This implies that from the outer loop's perspective the transfer function from $T_{ref}$ to $T_e$ can be considered as a unity gain. The closed loop transfer function from $\omega_{ref\_ZC}$ to $\omega_{ref}$ is then

$$\begin{aligned} G_{OL}(s) = \frac{\omega_{mec}(s)}{\omega_{ref}(s)} &= \frac{G_{PI}(s)G_M(s)}{1 + G_{PI}(s)G_M(s)} \\ &= \frac{\frac{K_I}{J_r}\left(\frac{K_P}{K_I}s + 1\right)}{s^2 + \left(\frac{K_P + B_r}{J_r}\right)s + \frac{K_I}{J_r}} \end{aligned} \tag{3.64}$$

From Equation (3.64) it can be observed that the PI controller introduces a zero to the closed loop transfer function. This derivative characteristic of the loop increases the system overshoot, lowering the potential closed loop bandwidth. Due to this, the zero of the PI controller must be compensated. This can be accomplished by a zero cancelation block introduced in the feed-forward path with the following transfer function.

$$G_{ZC}(s) = \frac{1}{\frac{K_P}{K_I}s + 1} \tag{3.65}$$

The speed loop transfer function with the zero-cancellation block in feed-forward path is then:

$$\begin{aligned} G_{OL}(s) = G_{ZC}(s)\frac{G_{PI}(s)G_M(s)}{1 + G_{PI}(s)G_M(s)} \\ = \frac{\frac{K_I}{J_r}}{s^2 + \left(\frac{K_P + B_r}{J_r}\right)s + \frac{K_I}{J_r}} \end{aligned} \tag{3.66}$$

Equation (3.66) represents a general second-order system which can be written in the form [35]

$$G_{OL}(s) = \frac{\omega_n^2}{s^2 + 2\xi\omega_n s + \omega_n^2} \tag{3.67}$$

where $\omega_n$ is the natural frequency and $\xi$ is the damping ratio of the closed-loop system transfer function. Thus, once the $\omega_n$ and $\xi$ are chosen based on the desired transient peformance requirements, the PI controller parameters can be obtained using:

$$K_P = 2\xi\omega_n J_r - B_r \tag{3.68a}$$

$$K_I = J_r\omega_n^2 \tag{3.68b}$$

The following table shows motor mechanical parameters and required closed-loop performance measures.

$\omega_n$ is selected to be high enough to make the closed-loop step response as fast as possible without introducing too much oscillation. To reduce this oscillation it is preferred to make the closed-loop system overdamped, i.e. $\xi > 1$. A good choice would be 2. Using Equation (3.68) one can then have, $K_P = 2.4$ and $K_I = 36$.

Table 3.3: Parameters used for outer loop PI controller design

| **Paramter** | **Value** |
|---|---|
| Rotor Inertia, $J_r$ $(kgm^2)$ | 0.01 |
| Rotational Friction, $B_r$ $(Nms)$ | 0.1 |
| Natural Frequency, $\omega_n$ $(rad/s)$ | 60 |
| Damping Ratio, $\xi$ | 2 |

### Current Controller Loop

This part of the controller consists of the current reference generator block and current regulator loop. The current reference generator block generates reference dq-axis currents based on the reference torque command $T_{ref}$ signal obtained from the outer (velocity) control loop, discussed previously. The approach used for generating the current references is a modified version of the zero d-axis control (ZDAC) method. ZDAC is mostly used in drives for PMSM and wound rotor synchronous motors in which dc excitation is given through brushes. In ZDAC, the d-axis current reference is set to zero for speeds up to base speed $\omega_{base}$. Above base speed, flux weakening method is used to determine the d-axis current reference value. The q-axis current is then determined from the torque demand, $T_{ref}$.

For this motor the d-axis current is always the superimposed triangular waveform $A_f(t)$. The field winding flux is proportional to amplitude, $I_f$, of this current. For speeds upto $\omega_{base}$, $I_f$ is kept constant. In the high speed operation region, $\omega_{mec} > \omega_{base}$, flux weakening techiques are used to determine the amplitude, $I_f$. The classical flux weakening method varies the field winding flux-producing current ($A_f(t)$) in proportion to the inverse of the rotor speed as [36].

$$I_{f\_ref} = \frac{\omega_{base}}{\omega_{mec}} I_{f\_rated} \tag{3.69}$$

Here, $I_{f\_rated}$ is the amplitude of the rated field excitation current. $i_{d\_ref}$ is thus $A_f(t)$ with amplitude $I_{f\_ref}$. Once $i_{d\_ref}$ is determined, the q-axis reference current, $i_{q\_ref}$ is then computed using

$$i_{q\_ref} = \frac{T_{ref}}{K_t I_{f\_ref}} \tag{3.70}$$

where

$$K_t = \left(\frac{3}{2}\right)^2 \frac{P}{2} \left(\frac{M_{fd}^2}{L_{fd}}\right)$$

is the average torque constant in Equation (3.41). The magnitude of $i_{q\_ref}$ in Equation 3.70 is limited by the voltage limit condition as given by Equation (3.54). As a result, the available axial torque will be saturated between the maximum and minimum values specific to the corresponding speed.

### Current Regulator

This block generates dq-axis voltage references from the corresponding current references. For controller design purposes, the load consists of the voltage source and the motor are modeled as first order plant for each axis.

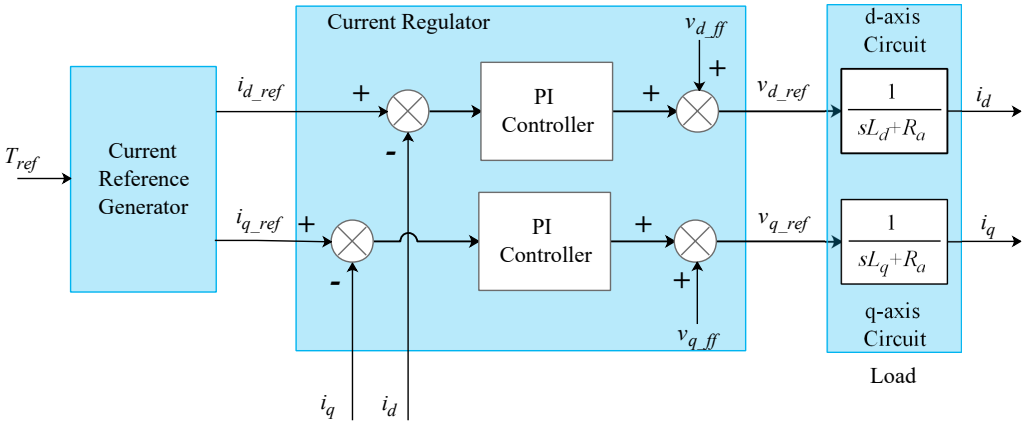


Figure 3.23: Current controller loop block diagram represention

Two PI controllers are required to regulate the current in each axis to the required values, $i_{d\_ref}$ and $i_{q\_ref}$. Each individual circuit in each reference frame axis can be modeled as an R-L circuit with an additional voltage term resulting from the speed voltages $-\omega_e\lambda_q$ for the d-axis and $\omega_e\lambda_d$ for the q-axis citcuit (Equation (2.40)). These voltage components can have a negative influence on the feedback current control. To eliminate the effect of these disturbance components and improve the performance of the current control, the feedforward control, as shown in Figure 3.23, is usually used along with the feedback control [36]. These feedforward terms represent cross coupling between the two axes and are given by

$$v_{d\_ff} = -\omega_e\lambda_q \tag{3.71a}$$

$$v_{q\_ff} = \omega_e\lambda_d \tag{3.71b}$$

Similar to the speed loop, the PI controller gains can be designed using the pole palcement method. Considering the following transfer function for the PI controller and the R-L load

$$G_{PI\_k} = \frac{K_{P\_k}s + K_{I\_k}}{s} \tag{3.72a}$$

$$G_{RL\_k} = \frac{1}{sL_k + R_a} \tag{3.72b}$$

where $k = d,\ q$ for the d- and q- axis circuits, respectively. The closed-loop transfer function for this inner loop is then

$$\begin{aligned} G_{IL\_k}(s) = \frac{i_k(s)}{i_{k\_ref}(s)} &= \frac{G_{PI\_k}(s)G_{RL\_k}(s)}{1 + G_{PI\_k}(s)G_{RL\_k}(s)} \\ &= \frac{\frac{K_{I\_k}}{L_k}\left(\frac{K_{P\_k}}{K_{I\_k}}s + 1\right)}{s^2 + \left(\frac{K_{P\_k}+R_a}{L_k}\right)s + \frac{K_{I\_k}}{L_k}} \end{aligned} \tag{3.73}$$

Introducing a zero-cancelation block in the feedforward path to compensate for the zero added by the PI controller with the transfer function

$$G_{ZC\_k}(s) = \frac{1}{\frac{K_{P\_k}}{K_{I\_k}}s + 1} \tag{3.74}$$

would result in the complete closed-loop transfer function

$$\begin{aligned} G_{IL\_k}(s) &= G_{ZC\_k}(s)\frac{G_{PI\_k}(s)G_{RL\_k}(s)}{1 + G_{PI\_k}(s)G_{RL\_k}(s)} \\ &= \frac{\frac{K_{I\_k}}{L_k}}{s^2 + \left(\frac{K_{P\_k}+R_a}{L_k}\right)s + \frac{K_{I\_k}}{L_k}} \end{aligned} \tag{3.75}$$

In a similar way to speed loop controller design approach, comparing the Equation (3.75) with the general form of a second order system in Equation (3.67), one can have

$$K_{P\_k} = 2\xi\omega_n L_k - R_a \tag{3.76a}$$

$$K_{I\_k} = L_k\omega_n^2 \tag{3.76b}$$

once $\omega_n$ and $\xi$ are chosen based on closed-loop pole location (or transient performance). The values of the PI gains for the current controller loops used in this thesis, however, are selected using a trial and error procedure, i.e, first the PI gains were selected by tuning the response. As such for the d-axis current loop, $K_P = 31.915$, $K_I = 930.321$ and for the q-axis current loop $K_P = 2.073$, $K_I = 37.213$. This results in $\omega_n = 282.91$, $\xi = 4.8$ for the d-axis current controller loop and $\omega_n = 84.726$, $\xi = 2.2547$ for the q-axis current controller loop.

### Implementation of control in FEM model

Within the COMSOL Multiphysics model the stator coils are driven with current excitation (where the coils are given current as an excitation instead of voltage) whose waveform is given using the **Definitions** part of the model. Since the currents supplied to the coils in the FEM model are already the desired waveform, current control is not necessary. However, velocity control can be added to the model using the **Global ODEs and DAEs** interface. This introduces additional dependent variables to be solved for, making the whole model more complex and time consuming. The PI controller algorithm are implemented using the following global equation.

$$T_{ref} = K_P\omega_{err} + K_I\int \omega_{err}dt \tag{3.77}$$

where $\omega_{err} = \omega_{ref} - \omega_{mec}$ is the error signal. Once the reference torque is computed, the stator current components can be determined using Equations (3.69) and (3.70). The maximum value of $i_{q\_ref}$ is limited by the $I_t$ value calculated from Equation (3.54). This approach adds the independent variables $\omega_{ref}$, $\int \omega_{ref}$ to the total system matrix.

# Chapter 4

# Results and Discussion

In this chapter, the results obtained from investigating the three models along with the discussion are presented. First the FEM model was used to study basic motor characteristics and operating principle. Next the analytical and Simscape models results are provided in comparison with the FEM model characteristics.

## 4.1 Results

Analyzing the motor using FEM in COMSOL Multiphysics involves performing a number of studies. Parametric, stationary and time dependent studies were used in this thesis to investigate the characteristics of the motor.

### Stationary study

The stationary studies for the model built took less than $10$ seconds to complete. The number of degrees of freedom solved for was $29,394$, which is the number of nodes of the mesh network on which the value of the unknown coefficients $\Phi_j$ are to be determined. The results of those studies are used as an initial conditions for the more complex time dependent studies.

### Time dependent study

Stationary studies for this motor do not provide the full information about the motor's behavior. The motor has, by design, variable field winding flux which can only be provided by time dependent studies. Performing time dependent studies using FEM involves a careful solver configuration of the time dependent solver. Especially in this motor there is a diode component that is highly nonlinear which makes the solution process very time consuming and sometimes nonconvergent at moments where the diode switches on and off. For example Figure 4.1 shows the convergence plot of a typical solution process for the motor.

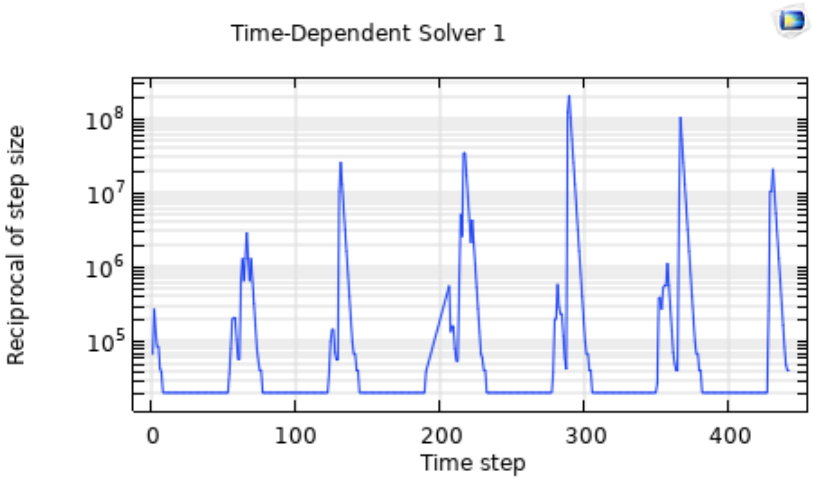


Figure 4.1: Time dependent solution convergence plot

In Figure 4.1 the value of the reciprocal of time step size taken by the solver to make the solution converge are shown. The peaks in the figure occur when the diode switches from off to on state and vice versa. At those instants very small amout of step size are taken by the solver in order to make the solution converge and be consistent with the previous state of the solution.

The time stepping algorithm used in this thesis was backward differentiation formula (BDF) of maximum order 2. For example the above convergence plot is for a time dependent solution was solved for six excitation periods, i.e. $6T_b = 6/f_b = 0.0150\,s$ at intervals of $8.3333 \times 10^{-5}$ seconds, where $f_b = 400\,Hz$. For this solver setting, the solution took around 14 minutes to complete. Similar to the stationary study, the number of degrees of freedom solved for was $29,394$.

### 4.1.1 FEM Model

#### Parameter Extraction

To determine the inductances of the motor, a **Magnetic Fields (mf)** study was performed in COMSOL Multiphysics. The **Magnetic Field** interface is used to compute magnetic field and induced current distributions in and around coils, conductors, and magnets [15]. Specially these types of studies can provide the inductance information of coils automatically. If one of the coils in the models is excited while the other coils remain open circuited (unexcited), the interface can compute the self-inductance of the excited coil along with the mutual inductances of this coil with the other unexcited coils. Thus, parametric stationary study was used to extract the inductances for different rotor positions in which by varying the rotational position of the rotating part of the motor, one can obtain the variation of the coil inductance values as a function of the rotor position as shown in Figure 4.2.

Figure 4.2a depicts the way the self inductance of coil b $l_{bb}$, mutual inductances between coils b and a ($l_{ab}$), b and c ($l_{cb}$) and b and f ($l_{bfd}$), respectively, vary as the rotor is rotated from $0\,rad$ to $\pi/2$, $radians$ (one full rotation in terms of electrical angle) and coil b is supplied with a dc excitation. In Figure 4.2b however, only field winding (coil f) is excited and the results show the variation of the coil f inductance $l_{ffd}$, mutual inductances between coils a and f ($l_{afd}$), coils b and f ($l_{bfd}$), and coils c and f ($l_{cfd}$) for the same amount of rotor rotation.

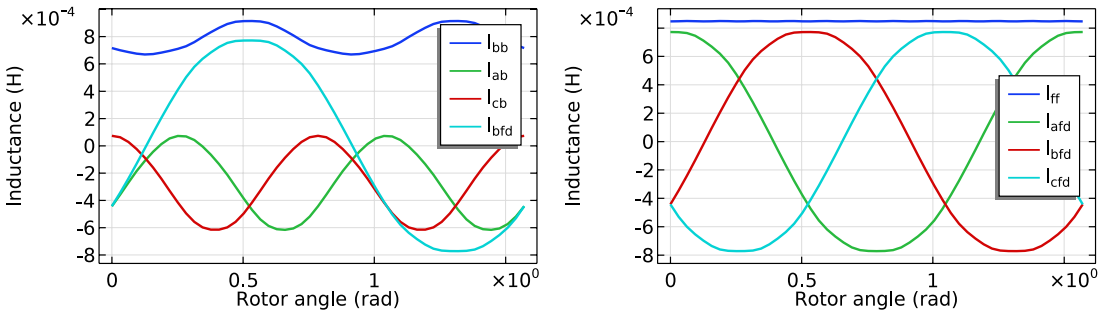


(a) Only coil b is excited

(b) Only coil f is excited

Figure 4.2: FEM calculated inductances

These inductance variations with respect to rotor position are similar to Equations (2.29a through 2.30c), although the actual waveforms in Figure 4.2 are not exact sinusoidal because of the stator slots. From these results, DQ- axis inductances can be computed. The MATLAB script used to extract those inductances from COMSOL and calculate the dq-axis inductances is provided in Appendix B.2. The resulting values of these inductance calculations are provided in Table 4.1. These calculations are based on the assumptions of sinusoidal variation as in Equations (2.29a through 2.30c). However due to the stator slots exact sinusoidal MMF distribution is not achievable. Hence, the actual motor dq-axis inductances differ from those provided in the table for different rotor positions. In addition to the inductances, DC resistances of the windings can also be computed using this interface. The resulting resistance values are provided in the table.

Table 4.1: Per-pole DQ-axis inductances and resistances

| **Parameter** | **Symbol** | **Value** |
|---|---|---|
| Stator d-axis self inductance | $L_d$ | $1.459 \times 10^{-3}$ H |
| Stator q-axis self inductance | $L_q$ | $6.480 \times 10^{-4}$ H |
| Stator rotor d-axis mutual inductance | $M_{fd}$ | $7.721 \times 10^{-4}$ H |
| Rotor (field) d-axis self inductance | $L_{fd}$ | $8.483 \times 10^{-4}$ H |
| Stator phase winding resistance | $R_a$ | $0.0116\,\Omega$ |
| Rotor (field) winding resistance | $R_{fd}$ | $0.0058\,\Omega$ |

These inductances and resistances can then be used to parametrize the Simscape and analytical models that will be extensively used for control design and simulation purposes. Due to saturation of the iron cores used in the stator and rotor, the inductances do not remain constant for the whole range of loading. This behavior can be extracted from the FEM model. Performing the inductance extraction procedure for different loading of the stator and rotor windings and computing the d-q axis self- and mutual- inductances, the following plot was generated (see Figure 4.3).

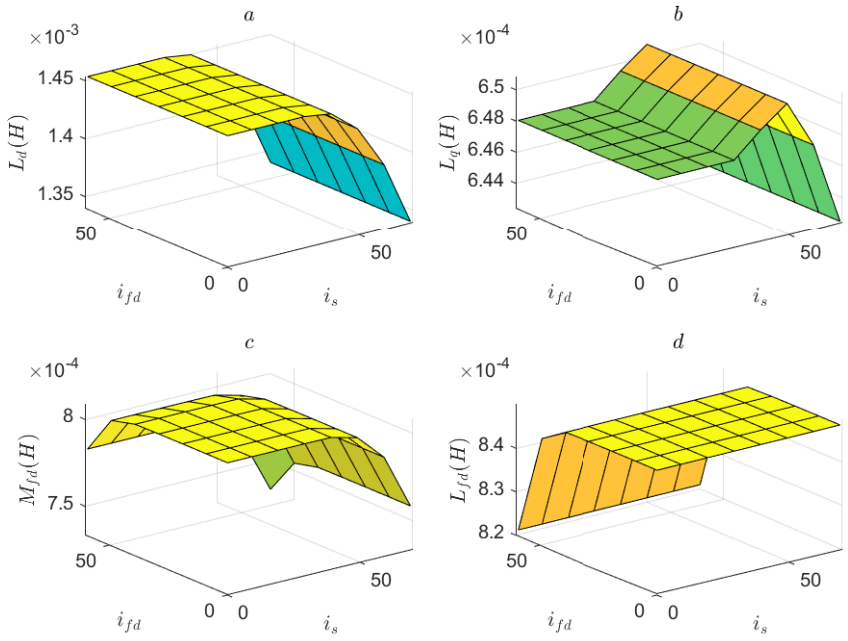


Figure 4.3: D-Q axis inductances variation with load

### Effect of Slots

Stator slots in the motor geometry introduce spatial disturbance in the magnetic flux distribution from the expected sinusoidal distribution. Figure 4.4, for example shows distribution of the magnitude of the magnetic flux density **B** across the middle of the air gap for the single pole of the motor under rated field winding excitation.

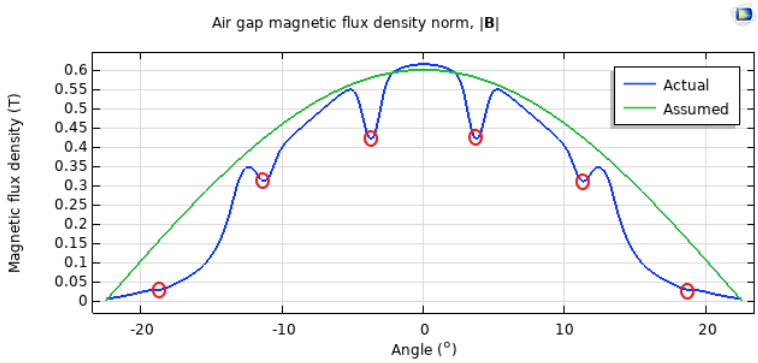


Figure 4.4: Air gap magnetic flux density variation due to stator slots

There are six dips in the figure corresponding to the six slots per single stator pole span. The plot is generated by supplying the field winding with a constant excitation. Most machine analysis techniques are done under the assumption of sinusoidal spatial flux distribution. Thus, this effect of stator slots introduces spatial variation in most of the important machine characteristics like, inductance, torque and flux linkage. For example, ignoring the torque ripple caused by the intentional d-axis MMF variation, the model studied in this thesis has the following normalized torque variations (see Figure 4.5).

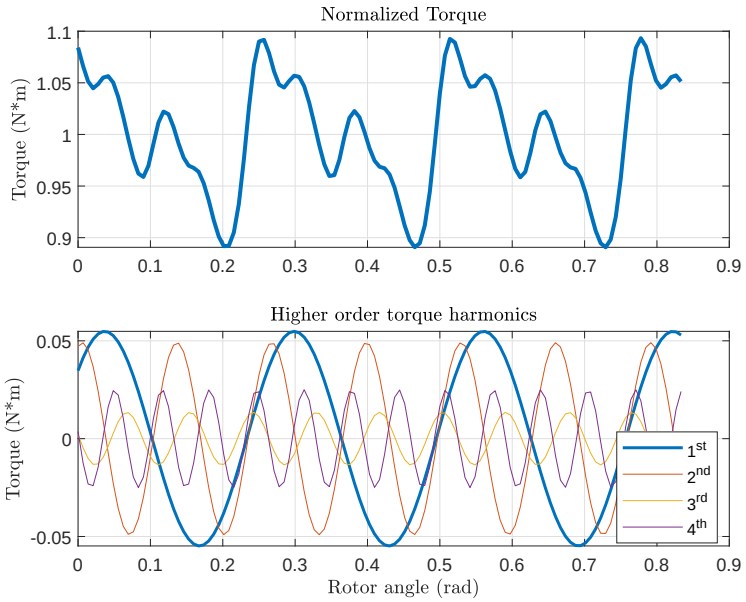


Figure 4.5: Axial torque ripple and higher order harmonics

The second figure in Figure 4.5 shows the higher ($2^{nd}$ to $4^{th}$) order harmonic components. Axial torque is not the only motor variable affected by the slots this way. Stator and field winding flux linkages also get affected.

### Rated Performance

The rated three-phase stator current supplied to the stator coils is as shown below in Figure 4.6. The selection of the bias frequency $f_b$ for this motor was based on the Equation (3.27). From the inductance and resistance values in Table 4.1, choosing $f_b = 400\,Hz$ gives $r = 58.3573$. Figure 4.6 shows the three-phase current supplied to the actual windings in the FEM model. The rotor synchronous rotating reference frame axes are shown in Figure 4.7a.

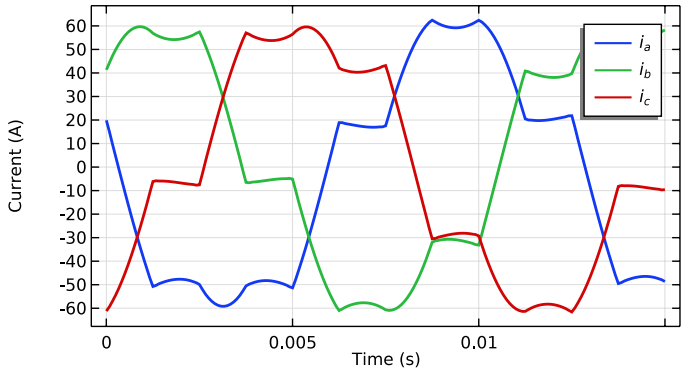


Figure 4.6: Rated abc stator current supply

Referring the three-phase to this reference frame gives the dq-axis currents as shown in Figure 4.7b.

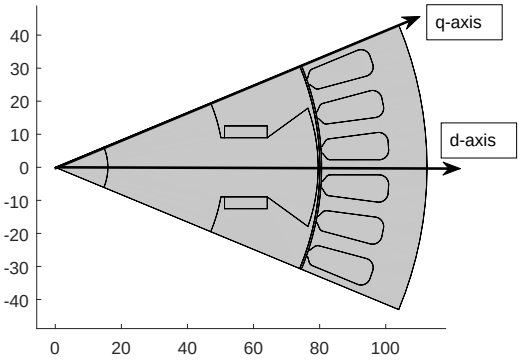


(a) Reference frame DQ axes

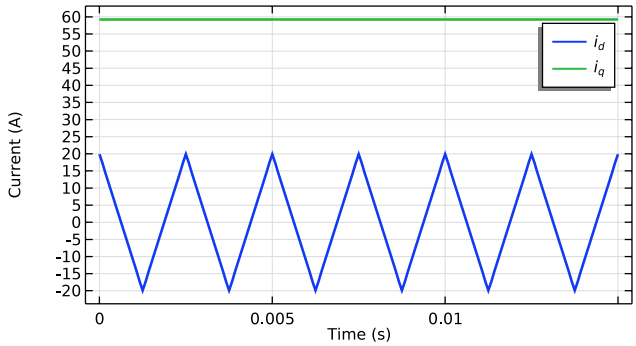


(b) dq-axis current

Figure 4.7: Reference frame DQ-axes and stator current supply

Supplying rated current for stator coils in the model and solving the problem using the stationary study gives the flux distribution of the motor at $t = 0s$ as shown in Figure 4.8a.

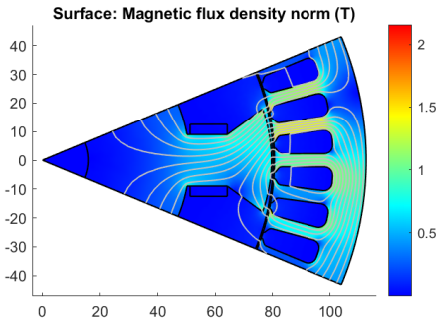


(a) Total flux distribution

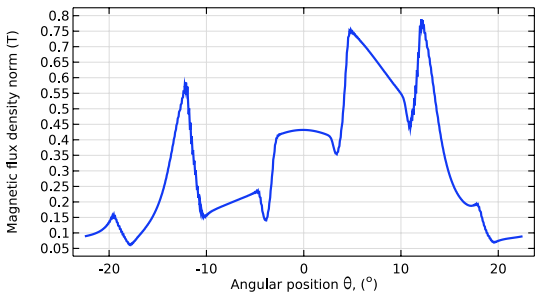


(b) Air gap magnetic flux density norm

Figure 4.8: Magnetic flux distribution at $t = 0\,s$

The flux distribution in Figure 4.8 is the result of both d-axis and q-axis current excitation, as shown by the non-zero values of both $i_d$ and $i_q$ in Figure 4.7b at $t = 0\,s$. To see the individual

effect of the d- and q-axis currents on the magnetic flux distribution, separate simulations were performed studying the effect of only $i_d$ or $i_q$, see Figures 4.9 and 4.10,.

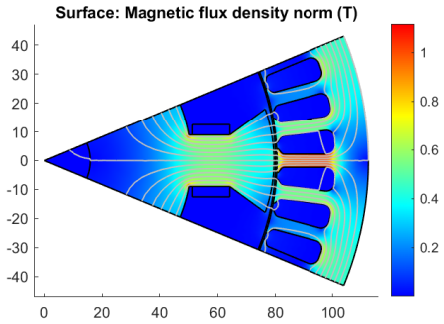


(a) Magnetic flux distribution

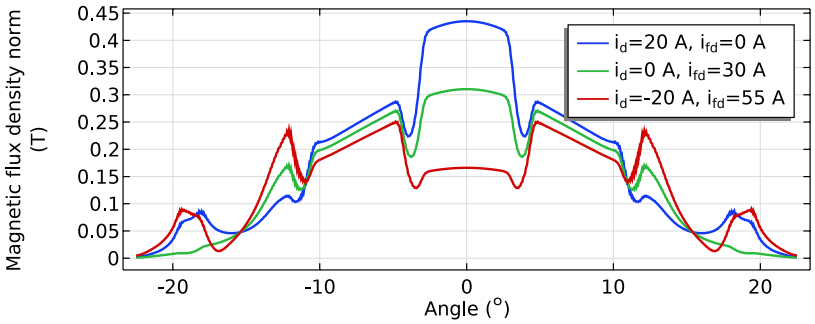


(b) Air gap magnetic flux density norm

Figure 4.9: Air gap magnetic flux distribution due to d-axis excitation only

The d-axis flux distribution is produced by the combination of the the stator d-axis current ($M_{fd}i_d$ term) and the field winding current ($L_{fd}i_{fd}$ term). Both these components do not remain constant during the operation of the motor. The resulting air gap magnetic flux density norm variation caused by this inherent behavior is depicted in Figure 4.10b.

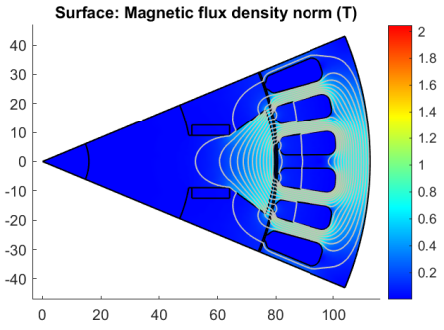


(a) Magnetic flux distribution

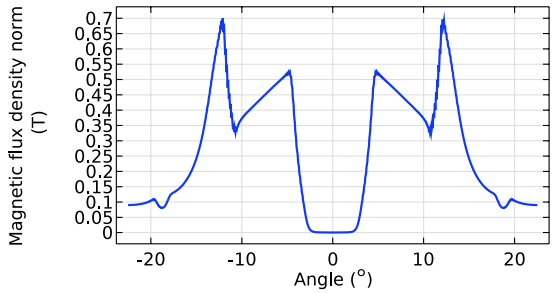


(b) Air gap magnetic flux density norm

Figure 4.10: Per-pole air gap magnetic flux distribution due to q-axis excitation only

Figure 4.10 shows the magnetic flux distribution and its norm along the middle of the air gap

under rated q-axis excitation only, i.e. $i_d = 0$, $i_{fd} = 0$. From the figure, it can be observed that the resulting q-axis magnetic flux links only the stator windings, i.e. no net magnetic flux links the field winding.

Once the field problem using FEM is solved, various motor characteristics of importance can be extracted using techniques of postprocessing in COMSOL Multiphysics. For example, using Equation (2.11) or (2.12) the flux linking the motor coils can be computed.

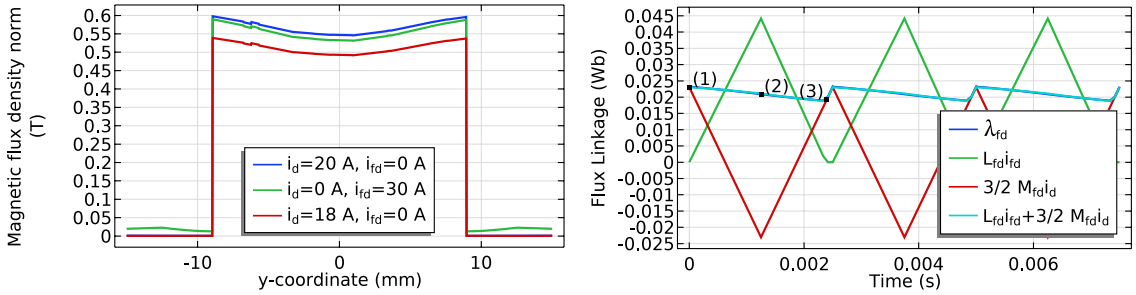


(a) Magnetic flux norm distribution linking field coils (b) Generation of field winding flux linkage

Figure 4.11: Per-pole field winding magnetic flux density distribution and flux linkage

Figure 4.11a shows the magnetic flux density norm across a vertical line at $x = 60\,mm$ (see Figure 4.9a) between $y = -15\,mm$ and $y = 15\,mm$. Almost all of the magnetic flux passes through the rotor iron core ($y = -9\,mm$ and $y = 9\,mm$) although non-zero leakage flux can be observed for non zero $i_{fd}$ values beyond the iron core. Using Equation (2.11) along the vertical line between $y = -9\,mm$ and $y = 9\,mm$ at $x = 60\,mm$, the flux linking the field winding $\lambda_{fd}$ can be computed. Figure 4.11b shows this flux linkage along with its contributing components calculated using the inductance concept. The field winding flux linkage varies between maximum (point (1)) corresponding to blue curve and minimum (point (3)) corresponding to the red curve in Figure 4.11a. The field winding flux linkage $\lambda_{fd}$ computed using FEM method (COMSOL actually uses the method of *Concatenated flux* to calculate flux linking a coil) and the $L_{fd}i_{fd} + {}^3\!/_2 M_{fd}i_d$ term calculated using inductance terms are both plotted in Figure 4.11b although they can not be distinguished from the figure.

Below are the time variations of the other main machine variables extracted from the solution using postporocessing techiques, see Figure 4.12. These waveforms are generated from the single-pole part of the motor equivalent to the FEM model COMSOL® described earlier, which is one-eighth of the whole motor. Shown in Figure 4.12 are the rotor current $i_{fd}$ (upper left), field winding flux linkage $\lambda_{fd}$ (upper right), stator d- and q- axis flux linkages $\lambda_d$ and $\lambda_q$ (lower left), and the electromagnetic torque produced $T_e$ (lower right). These values are obtained by supplying the stator with rated currents. To exclude the spatial torque ripple caused by the slots, the model was solved in locked rotor position at $0.4\,rad$. At that rotor position, the developed axial torque does not display the variation due to the slots as shown in Figure 4.5.

Assuming each one-eighth (single pole) sector of the stator and rotor parts are connected in series, the total amount of flux linkages and axial torque would be eight times that shown in Figure 4.12, while the currents remain the same. The total average torque is thus $8 \times 7.2059\,Nm =$

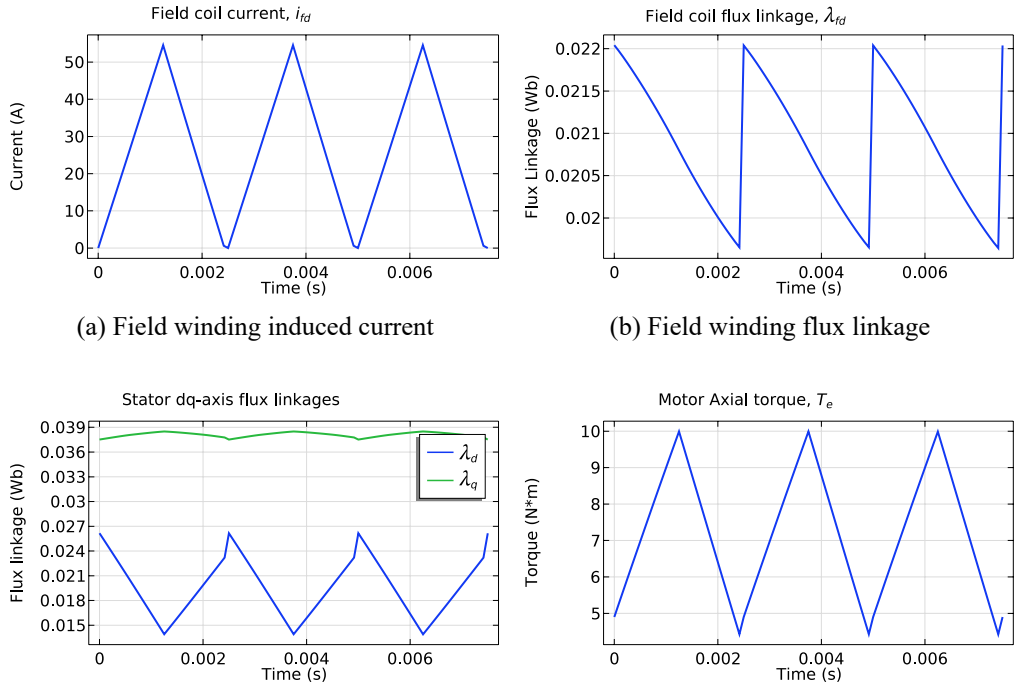


(a) Field winding induced current

(b) Field winding flux linkage

(c) Stator winding dq-axis flux linkages

(d) Axial torque

Figure 4.12: Per-pole COMSOL Model behavior

$58\,Nm$. For this position of the rotor, the peak-to-peak ripple torque is $9.9923 - 4.501\,Nm = 5.422\,Nm$ which is 74.7% of the average torque, a value that is higher than the value predicted by Equation (3.44). This descrepancy is caused by the difference in the values of the dq-axis inductances for different rotor positions mainly because of stator slots. Due to the non-exact sinusoidal nature of the variation of inductances with rotor position, the actual dq-axis vary from one rotor position to another.

When the rotor of the motor rotates, the effect of slots on the motor characteristics becomes apparent. For example, Figure 4.13 shows the field solution when the rotor is rotated at an angular speed of $1200\,rpm$.

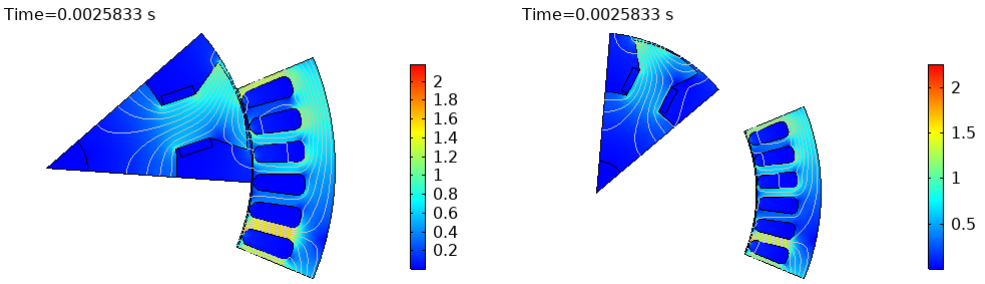


(a) field solution at $t_1 = 0.002583\,s$

(b) field solution at $t_2 = 0.00875\,s$

Figure 4.13: Time dependent field solution with constant rotor speed

In Figure 4.14 the axial torque generated when the motor rotates at a fixed angular speed of $1200\,rpm$ or $125\,rad/s$ is shown. It can be observed that the waveform in this figure is the combination of the patterns in Figure 4.12d modified by those shown in Figure 4.5.

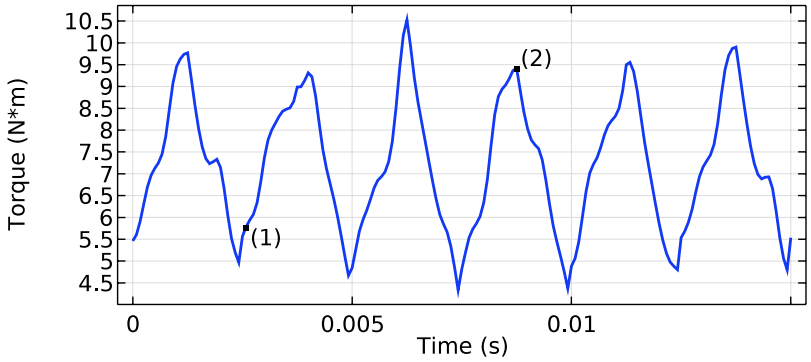


Figure 4.14: Axial torque for constant rotational speed

### Effect of varying stator current components

The following figure (Figure 4.15) shows the effect varying the stator current components $I_t$ and $I_f$ has on the average and ripple torque as well as on the field winding induced current and flux linkage when the motor is rotated at the rated angular speed of $1200\,rpm$.

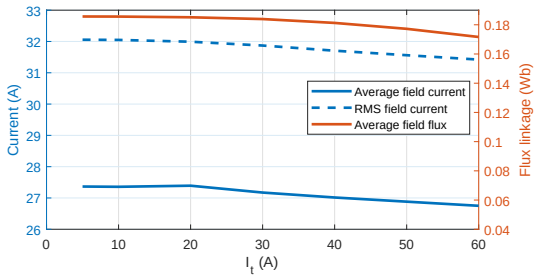


(a) Field winding current and flux, $I_f = 20\,A$

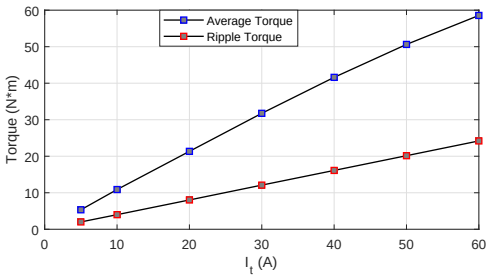


(b) Average and ripple torque, $I_f = 20\,A$

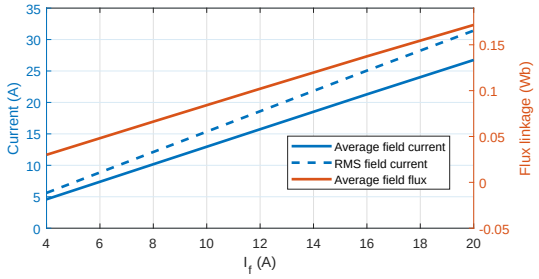


(c) Field winding current and flux, $I_t = 60\,A$

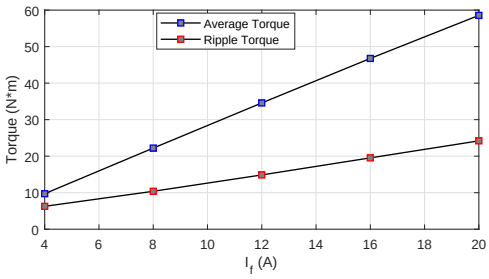


(d) Average and ripple torque, $I_t = 60\,A$

Figure 4.15: Effects of varying $I_t$ and $I_f$ on torque and field winding current and flux

Due to the nonuniformity of the torque, the ripple torque values in Figure 4.15b and 4.15d are computed as the standard deviation of the total torque data. Figure 4.15a and 4.15b show the effect of varying $I_t$ from zero to the rated value while $I_f$ is fixed at its rated value of 20 $A$. Figure 4.15c and 4.15d on the other hand show the effect of varying $I_f$ from zero to the rated value while $I_t$ is fixed at its rated value of 60 $A$.

### Effect of bias frequency $f_b$

To study how the bias frequency $f_b$ affects the performance of the motor, frequency domain studies are usually performed. COMSOL Multiphysics provides this type of study for models subject to harmonic excitation. For the motor model built in this thesis, however, the presence of the triangular d-axis current makes it difficult to define the coil excitation currents in the frequency domain. Therefore, instead of frequency domain studies individual time domain studies for different $f_b$ values were performed. The following figure shows this effect of the bias frequency $f_b$ on the motor characteristics. Similarly, the ripple torque plot in Figure 4.16b is the standard deviation of the total torque data.

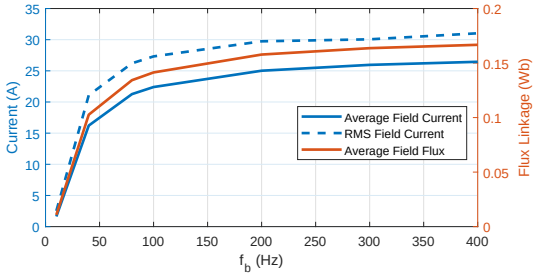


(a) Field winding induced current and flux

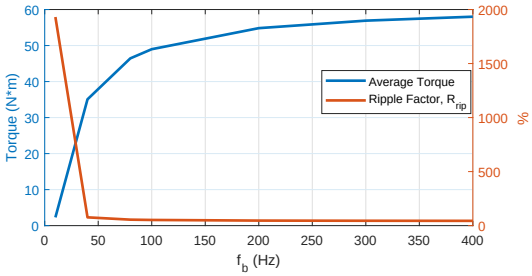


(b) Average torque and ripple factor, $R_{rip}$

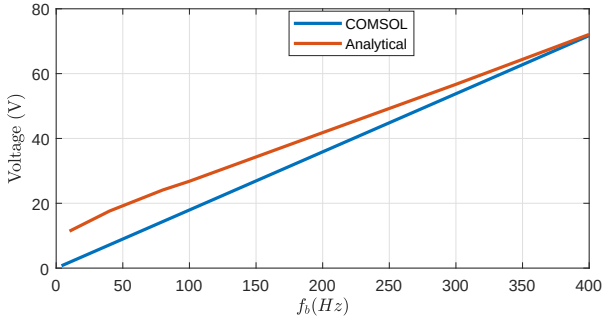


(c) Stator phase voltage

Figure 4.16: Effect of $f_b$ on motor characteristics

To account for the effect of only bias frequency $f_b$ on those motor characteristics, the simulation was performed in locked rotor position. This makes the speed voltages in Equation (2.40) to become zero. That is why the stator phase voltage below the rated value in Figure 4.16c. In this figure the plot of stator phase voltage versus bias frequency $f_b$ for the analytical model is included for comparison.

### 4.1.2 Simscape and Analytical Models

Figure 4.17 shows the previous motor characteristics for the COMSOL FEM model, the Simscape model and the analytical model when the motor was driven with $I_t = 20\,A$ and $I_f = 10\,A$. In the Simscape and analytical models, constant inductance values are used to parametrize the motor. For most of the low motor loading operation ranges the values of those inductances remain almost constant. However, when the motor is highly loaded, the inductances change as shown in Figure 4.3. This introduces differences in the motor behavior between the FEM model and the other two models. Thus, to compare the three models properly the effect of motor load and stator slots have to be removed.

The following plots in Figure 4.17 are generated at fixed rotor position (to remove effects of stator slots) and at low motor load operation region (to reduce iron saturation effects, hence inductance variations).

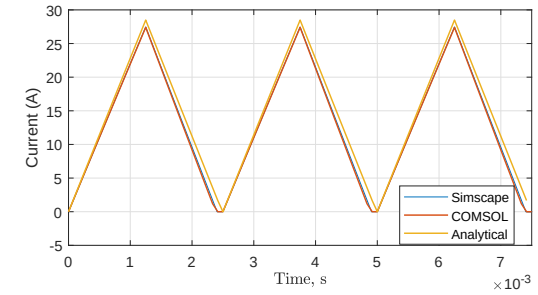


(a) Field winding induced current

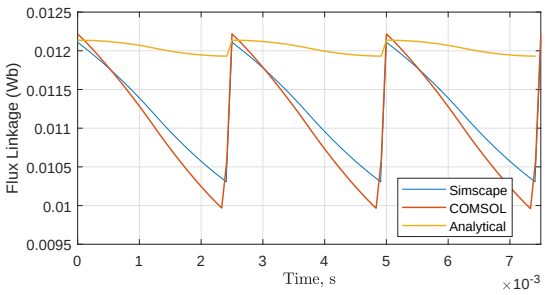


(b) Field winding flux linkage

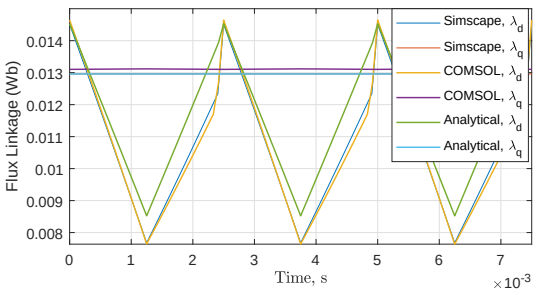


(c) Stator winding dq-axis flux linkages

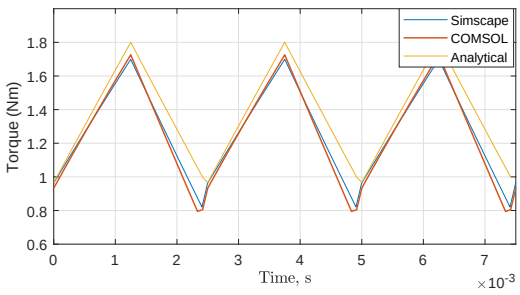


(d) Axial torque

Figure 4.17: COMSOL, analytical and Simscape models behaviors

#### Motor output characteristics

The following figure (Figure 4.18) shows the torque, voltage and power versus speed curves of the three motor models. The figure shows motor capabilities at different rotor speed. The torque shown in the plot in Figure 4.18a is the average torque. The analytical and the Simscape models are well within the voltage limit as shown in the figure.

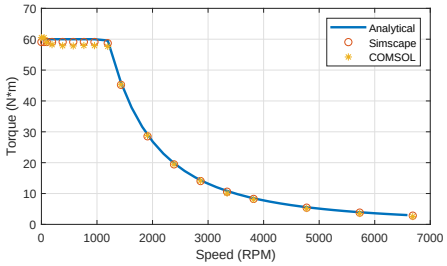


(a) Average torque versus speed curve

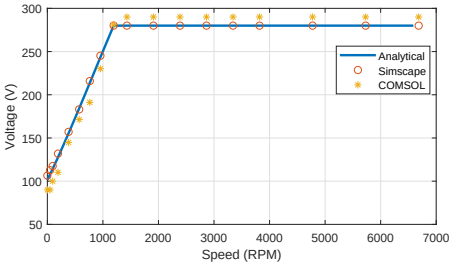


(b) Voltage versus speed curve

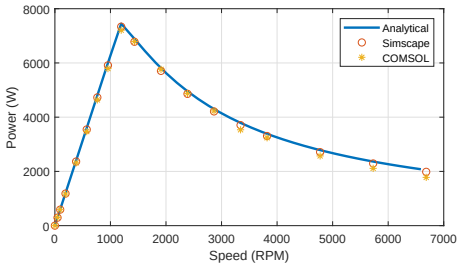


(c) Power versus speed curve

Figure 4.18: Motor output characteristics

### 4.1.3 Controller Performance

#### FEM Model

The FEM model controller speed response is shown in Figure 4.19 below. PI controller gains designed for the Simscape model speed loop were used, i.e., $K_P = 2.4$ and $K_I = 36$. The model was simulated for 30 bias period intervals $30T_b = 0.075$ seconds at an interval of $8.333 \times 10^{-5}$ seconds. The solution took $2\,hr\ 58\,min\ 24\,s$. The complete simulated file has just over 860 Megabytes of size.

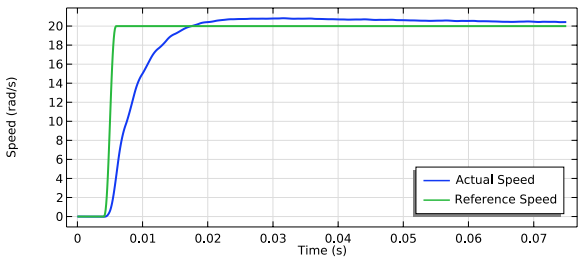


(a) Speed response

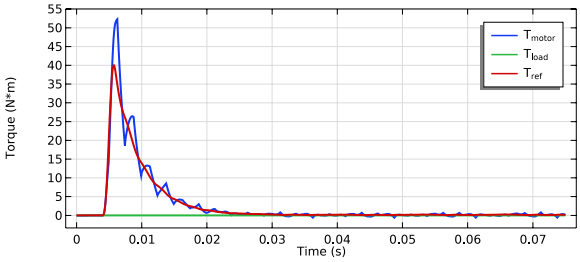


(b) Torque response

Figure 4.19: FEM model controller behavior

Load torque was not included here to limit the solution time. The resulting reference torque $T_{ref}$ and the actual motor torque $T_{motor}$ are shown in Figure 4.19b. The speed response is shown

to approach the reference command. If the simulation was allowed to continue, it would have reached the required value. One important thing to notice in Figure 4.19a is the oscillation in the speed response. This is caused by the torque ripple inherent to the motor.

### Simscape Model

Below in Figure 4.20 is the simulation model used to test the controller implemented using the approach in 3.5. Reference speed in RPM and load torque are provided using a signal builder block in SIMULINK.

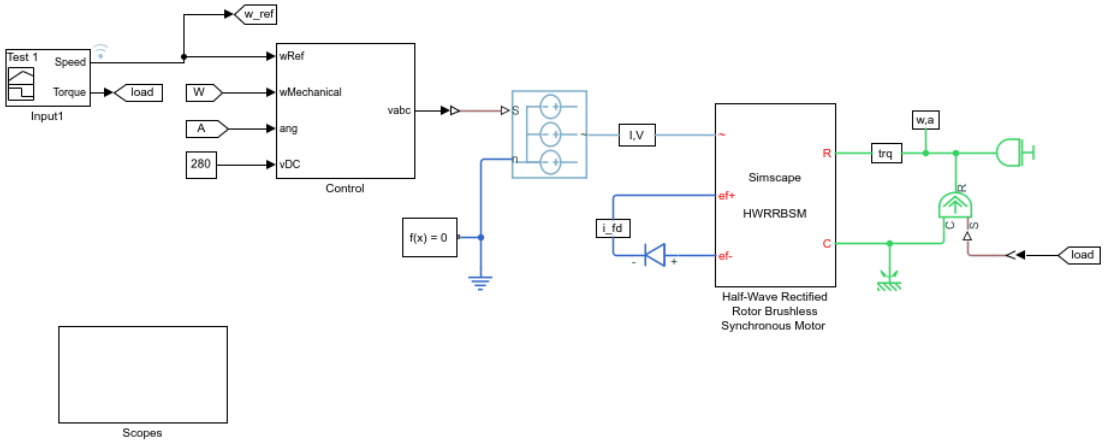


Figure 4.20: SIMULINK Controller setup

The actual implementation of 'control' block in the figure is provided in Appendix C. The response shown in Figure 4.21 displays the behavior of the speed control loop. Step changes in the reference speed command were applied at $0.05$, $0.05$, $1.5$ and $2.5$ seconds. The plot shows that the response has an overdamped response as designed.

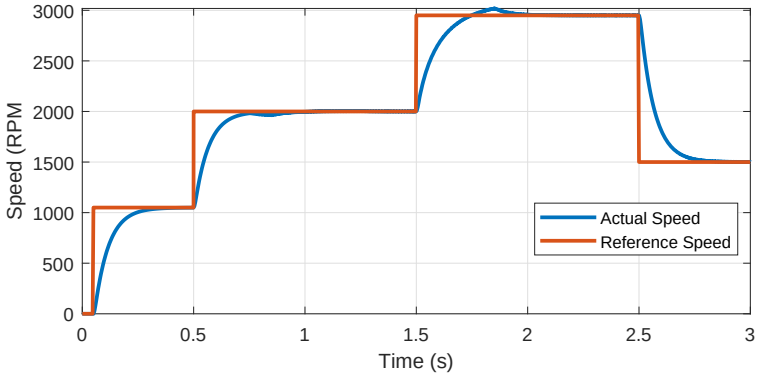


Figure 4.21: Model speed response

In Figure 4.22a, the load torque $T_{load}$, upper and lower torque limits, $\pm T_{lim}$ and reference torque $T_{ref}$ obtained from the speed loop are shown. In addition to the speed commands, load torque demand was applied at $t = 0.75\,s$ which was ramped up to $15\,Nm$ at $t = 0.85\,s$ remaining at that value until $t = 1\,s$. Then it was ramped down to $12\,Nm$ at $t = 1.25\,s$ from which on it remained unchanged for the remaining simulation time.

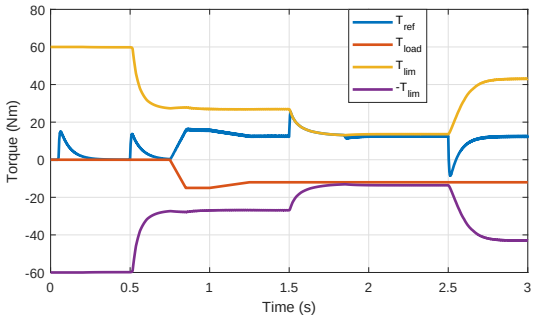


(a) Load and reference torques

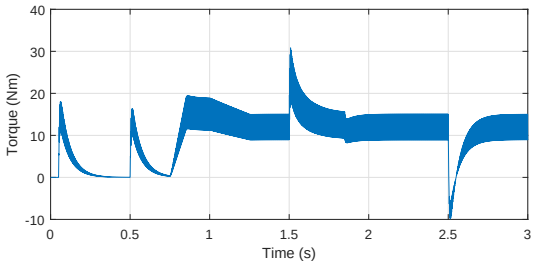


(b) Developed motor torque response

Figure 4.22: Motor torque response

The torque limits change with the rotor speed according to the torque speed curve in Figure 4.18. The reference torque $T_{ref}$ generated by the speed loop, on the other hand, is dependent on the load torque $T_{load}$ and the speed loop error command, $\omega_{err} = \omega_{ref} - \omega_{mec}$. In Figure 4.22b, the actual electromagnetic torque $T_e$ produced is shown. When the motor is operating at its full capacity between $t = 1.5\,s$ and $t = 1.75\,s$ (as shown by the torque demand $T_{ref}$ and torque limit $T_{lim}$), the stator voltage reaches its maximum value of $280\,V$ (see Figure 4.24b). In this time interval the speed response in Figure 4.21 shows overshoot due to integral windup caused by sustained velocity error signal caused by the limited (saturated) developed torque at the rotor. This problem can be avoided using integral anti-windup controllers. Figure 4.23 shows the speed response for the control system when such approach is implemented using the anti-windup scheme of back calculation

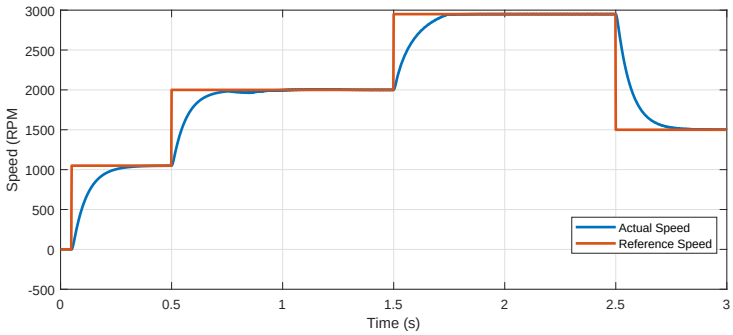


Figure 4.23: Model speed response with integral anti-windup control

The three-phase stator current supply and the corresponding phase voltage for the three stator phase windings for simulation is shown in Figure 4.24.

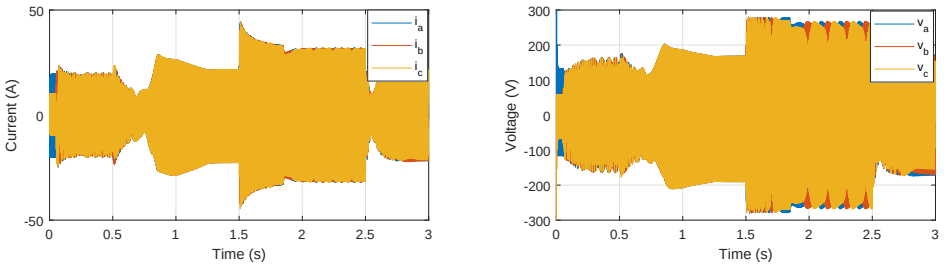


(a) Stator three-phase current (b) Stator three-phase voltage

Figure 4.24: Motor stator three-phase current and voltage

The d-axis reference current in this control approach is a time varying, hence the actual d-axis current never follows the reference current unless the current regulator has infinite gain [36]. This is shown in Figure 4.25.

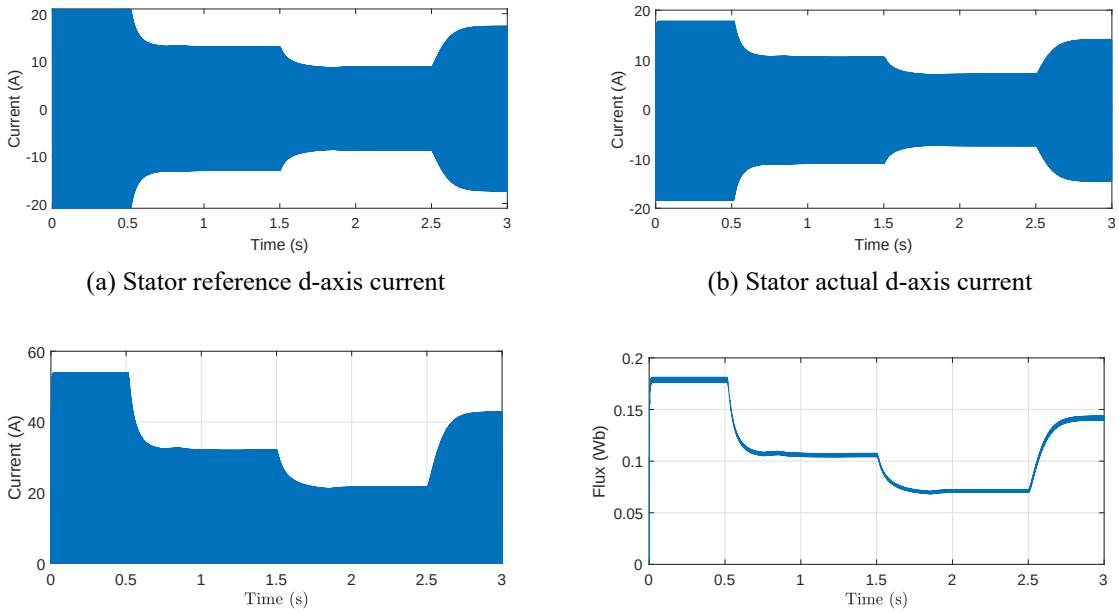


(a) Stator reference d-axis current (b) Stator actual d-axis current

(c) Field winding current (d) Field winding flux linkage

Figure 4.25: D-axis current and field flux linkage

By appropriately scaling the d-axis reference current, this limitation can be eliminated. The flux weakening operation can be observed in Figure 4.25d. The figure shows the variation of the field winding flux according to rotor speed, the $1/\omega_{mec}$ approach (Figure 4.21.) The dependence of this flux only on the field winding current $i_{fd}$ is also shown in Figure 4.25c and 4.25d

## 4.2 Discussion

As shown in Figure 4.10 the reference frame q-axis flux does not link the field winding (i.e. $\lambda_q = L_q i_q$). The d-axis flux distribution, however, is shown to link both the field and stator windings, (see Figure 4.9 ) implying that the flux is the result of both the stator and field winding currents. The air gap flux distributions shown in Figure 4.8 through Figure 4.10 are for the rated stator current supply. For the FEM model, besides the inherent temporal torque ripple introduced by the behavior of the motor, spatial torque ripple due to slots (Figure 4.5), reluctance torque due to saliency are also present. Thus the total electromagnetic torque produced at the rotor of the motor will have variations caused by:

1. varying d-axis MMF
2. stator slots and saliency
3. inductance variation due to varying load levels

From the Figure 4.15, it can be observed that field winding current and flux linkage remain unaffected for $I_t$ values of up to $30\,A$. Above this value, the average and RMS values of $i_{fd}$ and the average value of $\lambda_{fd}$ decrease, see Figure 4.15a. This is caused by the saturation of the iron cores in the stator and rotor which affects the values of the inductances. This effect is also observed in the average torque in Figure 4.15b. Varying the peak value of the field excitation component current $I_f$ of the stator current and observing the resulting motor behavior, one can deduce that for the rated value of $I_t = 60\,A$, the average and RMS value of $i_{fd}$ as well as the average value of field winding flux, $\lambda_{fd}$ linearly correlate with $I_f$. The straight line (linear) relationship between the average and ripple torque to $I_f$, in Figure 4.15d shows that saturation effects do not occur for this specific range of $I_f$ variations.

The effect of the bias frequency $f_b$ on the field winding current and flux plus the axial torque shown in Figure 4.16 shows the logarithmic relationship depicted in Figure 3.16 in Section 3.3. The presence of a time varying d-axis current component oscillating at the bias frequency introduces a non-zero rate of change of d-axis flux even under steady state conditions. This causes an additional d-axis voltage term proportional to the bias frequency, see Figure 4.16.

From the torque versus speed curve in Figure 4.18a, it can be observed that the motor torque decreases rapidly in the flux weakening region of operation. The mechanical power in this region (shown in Figure 4.18c) does not stay constant. This is one limitation of this motor as compared to PMSMs. The output torque in this region of operation can be improved by using optimal selection of the current components $I_t$ and $I_f$ using the maximum torque per ampere (MPTA) techniques.

The speed response for the FEM model based controller shows overshoot (see Figure 4.19a) although the PI gains were designed to have an overdamped closed loop response. This is due to the fact that the zero cancelation block was not added to the controller to reduce system complexity. The drive control system based on the Simscape model on the other hand performed as designed. In comparison the simulation time for this model was only $50\,s$. Thus, for the purposes of rapid drive system development the Simscape based model is preferred.

Although the easy torque and speed control capability of the motor is very promising, mechanical oscillation introduced by the torque ripple can be highly dangerous. Especially, this behavior is undesired for EV applications as it could cause mechanical instability and component failure.

# Chapter 5

# Conclusion and Future Work

## 5.1 Conclusion

The motor studied in this thesis is a three-phase synchronous machine with the field winding short-circuited by a diode. With no permanent magnets or brushed connections to excite the field winding, a time-varying superimposed d-axis current is used to induce a time-varying voltage in the field winding which is rectified by the diode to produce a DC current for excitation. Using the FEM implemented in COMSOL Multiphysics, this principle of operation was verified for a specific motor designed in this thesis. The motor displays the important performance characteristics such as wide range of speed and torque controlability (Figure 4.18a), variable field flux that can be controlled using stator current (Figure 4.25), and adjustable efficiency map (shown by different copper loss for different values of $\frac{I_t}{I_f}$ in Figure 3.19).

The FEM analysis involved the determination of the magnetic flux distribution within the geometry of the motor based on the governing Maxwell's equations of electromagnetics. Once the field distribution was computed, motor parameters (like inductance and resistance), and performance characteristics (like torque, flux linkage, voltage) were extracted to characterize the motor. The inductances were also used to parameterize the simscape and analytical models developed for the motor. This specific motor displayed an almost constant field winding flux linkage produced by the combination of the time-varying d-axis flux and the induced field winding flux. This almost constant flux was used to replace the permanent magnet or external brush connection to supply field winding current.

By adding additional physics defining other behaviors of the motor than the magnetic flux distribution, like electrical circuit and rotor dynamics, complete model representing the electromechanical behavior was developed within the COMSOL Multiphysics environment. This model was used to study the effect of varying some design and operation parameters such as bias frequency $f_b$, stator current components $I_t$ and $I_f$ on motor performance characteristics like developed electromagnetic torque, field winding induced current, flux linkage and voltage.

Of the three models the FEM based model is the closest to the actual real-life device. The model uses the actual geometrical and material properties to predict the motor's behavior. Especially, the effects of stator slots and magnetic saturation in the iron cores used for stator and rotor design were observed to affect the performance characteristics. These effects cause the predictions made by this

FEM model to differ from those made by the other two models developed based on assumption of neglecting such geometrical (stator slots) and material (magnetic saturation) properties.

From the results describing the effect of the bias frequency $f_b$ it can be concluded that a single frequency value can be chosen for the whole range of operation. The selection of this parameter should be based on the trade-off between reducing the ripple factor $R_{rip}$ on the lower end, and the reducing the hysteresis loss and meeting the sampling frequency limitations on the higher end. Special design technique could also be applied to reduce the ripple factor $R_{rip}$. By properly selecting different combinations of the stator current components $I_t$ and $I_f$, improved performance of the motor can be achieved at different operating points.

The FEM based model requires a large amount of computational resource to perform complex studies. The time-domain equivalent circuit based analytical equations were used as a basis of an approximate analytical model and a Simscape model. Besides the governing equations, these two models use different representations for the field winding rectifying diode (see Table 5.1)

Table 5.1: Different diode models used

| **Motor model** | **Diode model** | **Equation** |
|---|---|---|
| FEM | exponential | $i_{fd} = I_S \left(e^{\frac{v_{fd}}{NV_T}} - 1\right) \dfrac{1}{\sqrt{1 + \frac{I_S}{I_{KF}} \left(e^{\frac{v_{fd}}{NV_T}} - 1\right)}}$ |
| Simscape | piece-wise linear | $i_{fd}(t) = \begin{cases} \dfrac{v_{fd} - V_f(1 - R_{on}G_{off})}{R_{on}} & \text{for } v_{fd} \geq V_f \\ v_{fd}G_{off} & \text{for } v_{fd} < V_f \end{cases}$ |
| Analytical | ideal | $\begin{array}{ll} short\,circuit & \text{for } v_{fd} \geq 0 \\ open\,circuit & \text{for } v_{fd} < 0 \end{array}$ |

The major cause of differences in performance characteristics of the three motor models is the way the diode is modeled causing the field winding induce current $i_{fd}$ and flux linkage $\lambda_{fd}$ to vary from model to model. In the ideal condition, assuming $f_b$ is large enough, $\lambda_{fd}$ can be considered to remain constant. The maximum deviation of the fluxes of the models from this ideal flux can be used as a means of comparison among the models. From Figure 4.17, it can be seen that in terms of field winding flux linkage variation the analytical shows a 1.7%, Simscape a 14.8% and FEM (COMSOL) a 18.4% of maximum deviation from the ideal constant flux.

FOC based controller was designed to show the applicability of a simple speed controller. Pole placement was used to design the PI controllers gains for both the speed loop and dq-axis current loops. The performance of this controller was satisfactory with one limitation. The d-axis reference current $i_{d\_ref}$ for this motor is an AC triangular waveform unlike PMSMs or induction motors where the d-q axis reference currents are constant under steady state. This causes amplitude and phase error between the reference and actual d-axis currents when using a PI regulator.

If the computational resource allows it, additional physics interfaces can be added to the FEM model describing various physical aspects of the motor such as thermal, structural, noise and so

on. For fast and simple drive system designs however, the Simscape based model should be used. The analytical model equations were used to perform quick technical predictions and get insight into the performance of the motor. Due to the closed form of the equations within this model, operating limits and controller design calculations can be easily performed using these equations. The Simscape model was specifically built to be used for controller design and testing purposes. Both these models are based on constant winding inductance assumptions and are parametrized using inductances extracted from the FEM model.

From Figure 4.18, one can observe that the motor has high starting (and low speed) torque with wide controllable speed range. There are no permanent magnets or brushes for external field excitation connection offering simple and robust structure at a lower cost (no brushes or permanent magnets). The direct relationship between the current component $I_f$ and field flux enables easy implementation of variable field flux drive techniques. In addition, the reduction in this current component during flux-weakening operations lowers stator and rotor copper losses which improves the efficiency of the motor. These behaviors are all required from motors used as EV traction drives. However, the following are some of the limitations of this motor as a candidate for EV traction derive applications:

1. inherent torque ripple caused by time varying d-axis mmf
2. higher than normal frequency $f_b$ current component which would require higher sampling frequency for digital control implementations
3. non-constant power operating behavior in the flux-weakening region

## 5.2 Future Work

The models built and studied in this thesis focuses only on the electromagnetic characteristic of the motor. Especially, due to the high computational demand and the broader scope, thermal and structural studies were not performed using the FEM model. For future studies of this motor these analyses should be included.

To account for the core losses in the FEM model, the Jiles-Atherton hysteresis model for core materials have been attempted in the COMSOL Multiphysics simulation model. However, the complexity of the modeling added to the limited computational resource used in this thesis, the model did not converge. Hence, an approximate formula based on [37] has been used for the hysteresis loss. For accurate modeling of the effect of the bias frequency $f_b$ on motor losses, FEM based hysteresis loss calculations should be investigated.

In order to use the motor as a viable choice for traction drive for EVs, research on improving the limitations discussed in the previous section should be pursued. The torque ripple caused by the time varying d-axis mmf is fundamentally dependent on the magnetic design of the motor as shown by Equation (3.44). Therefore, appropriate design methods can be used to reduce the torque ripple to an acceptable range.

Controllers implementations regulating the peak value, $I_f$ of the triangular waveform $A_f(t)$ instead of $A_f(t)$ itself should be investigated. This would eliminate the d-axis current controller tracking problem discussed earlier. It also allows the use of lower sampling time d-axis controllers as the controller now controls the amplitude $I_f$ instead of the actual AC waveform $A_f(t)$. Better performance can be gained by using different combinations of the stator current components $I_t$ and $I_f$ at different operating points in the torque versus speed curve. Thus, optimal control techniques with objectives of reducing the copper loss and improving the axial torque produced like the maximum torque per ampere (MTPA) method should be investigated.

# Appendix A

# Analytical Calculations

## A.1 Reference frame calculations

Given reference frame transformation matrix from $abc$ to $dq0$

$$T = \frac{2}{3}\begin{bmatrix} \cos\theta & \cos\left(\theta - \frac{2\pi}{3}\right) & \cos\left(\theta - \frac{4\pi}{3}\right) \\ -\sin\theta & -\sin\left(\theta - \frac{2\pi}{3}\right) & -\sin\left(\theta - \frac{4\pi}{3}\right) \\ \frac{1}{2} & \frac{1}{2} & \frac{1}{2} \end{bmatrix} \tag{A.1}$$

and the inverse transform from $dq0$ to $abc$

$$T^{-1} = \begin{bmatrix} \cos\theta & -\sin\theta & 1 \\ \cos\left(\theta - \frac{2\pi}{3}\right) & -\sin\left(\theta - \frac{2\pi}{3}\right) & 1 \\ \cos\left(\theta - \frac{4\pi}{3}\right) & -\sin\left(\theta - \frac{4\pi}{3}\right) & 1 \end{bmatrix} \tag{A.2}$$

we have,

$$\begin{bmatrix} i_a \\ i_b \\ i_c \end{bmatrix} = T^{-1}\begin{bmatrix} i_d \\ i_q \\ i_0 \end{bmatrix} = \begin{bmatrix} \cos\theta & -\sin\theta & 1 \\ \cos\left(\theta - \frac{2\pi}{3}\right) & -\sin\left(\theta - \frac{2\pi}{3}\right) & 1 \\ \cos\left(\theta - \frac{4\pi}{3}\right) & -\sin\left(\theta - \frac{4\pi}{3}\right) & 1 \end{bmatrix}\begin{bmatrix} i_d \\ i_q \\ i_0 \end{bmatrix} \tag{A.3}$$

Now

$$\begin{bmatrix} \lambda_d \\ \lambda_q \\ \lambda_0 \end{bmatrix} = T\begin{bmatrix} \lambda_a \\ \lambda_b \\ \lambda_c \end{bmatrix} = \begin{bmatrix} \cos\theta & \cos\left(\theta - \frac{2\pi}{3}\right) & \cos\left(\theta - \frac{4\pi}{3}\right) \\ -\sin\theta & -\sin\left(\theta - \frac{2\pi}{3}\right) & -\sin\left(\theta - \frac{4\pi}{3}\right) \\ \frac{1}{2} & \frac{1}{2} & \frac{1}{2} \end{bmatrix}\begin{bmatrix} \lambda_a \\ \lambda_b \\ \lambda_c \end{bmatrix} \tag{A.4a}$$

$$\lambda_{fd} = l_{afd}i_a + l_{bfd}i_b + l_{cfd}i_c + l_{ffd}i_{fd} \tag{A.4b}$$

where $\lambda_a$, $\lambda_b$ and $\lambda_c$ are given by Equation (2.28) in which $i_a$, $i_b$, $i_c$ are given by Equation A.3

and simplifying gives

$$\lambda_d = (L_{aa0} + \frac{L_{aa2}}{2} + L_{ab0} + L_{ab2})i_d + L_{afd}i_{fd} \tag{A.5a}$$

$$\lambda_q = (L_{aa0} - \frac{L_{aa2}}{2} + L_{ab0} - L_{ab2})i_q \tag{A.5b}$$

$$\lambda_{fd} = \frac{3}{2}L_{afd}i_d + L_{ffd}i_{fd} \tag{A.5c}$$

Defining the dq-axis inductances as

$$L_d = L_{aa0} + L_{ab0} + \frac{1}{2}L_{aa2} + L_{ab2} \tag{A.6a}$$

$$L_q = L_{aa0} + L_{ab0} - \frac{1}{2}L_{aa2} - L_{ab2} \tag{A.6b}$$

$$L_{fd} = l_{ffd} \tag{A.6c}$$

$$M_{fd} = L_{afd} \tag{A.6d}$$

one can have

$$\lambda_d = L_d i_d + M_{fd}i_{fd} \tag{A.7a}$$

$$\lambda_q = L_q i_q \tag{A.7b}$$

$$\lambda_{fd} = \frac{3}{2}M_{fd}i_d + L_{fd}i_{fd} \tag{A.7c}$$

## A.2 Base Speed Determination

To find the base speed $\omega_b$, the voltage limit curve ellipse equations can be solved for $\omega$ for a given $V_{s\_max}$, and rated $dq-$ axis current values. Thus, writing the voltage limit equation as

$$v_d \approx \frac{d}{dt}\lambda_d - \omega\lambda_q \tag{A.8a}$$

$$v_q \approx \frac{d}{dt}\lambda_q + \omega\lambda_d \tag{A.8b}$$

which using

$$\lambda_d = L_d i_d + M_{fd}i_{fd} \tag{A.9a}$$

$$i_{fd} \approx \frac{3}{2}\frac{M_{fd}}{L_{fd}}(I_f - i_d) \tag{A.9b}$$

gives

$$\begin{aligned} v_d &= \left(L_d - \frac{3}{2}\frac{M_{fd}^2}{L_{fd}}\right)\frac{d}{dt}i_d - \omega L_q i_q \\ &= A\frac{d}{dt}i_d + \omega B i_q \end{aligned} \tag{A.10a}$$

$$\begin{aligned} v_q &= \omega\left[\left(L_d - \frac{3}{2}\frac{M_{fd}^2}{L_{fd}}\right)i_d + \frac{3}{2}\frac{M_{fd}^2}{L_{fd}}I_f\right] \\ &= \omega\left(Ai_d + CI_f\right) \end{aligned} \tag{A.10b}$$

where

$$A = L_d - \frac{3}{2}\frac{M_{fd}^2}{L_{fd}} \tag{A.11a}$$

$$B = -L_q \tag{A.11b}$$

$$C = \frac{3}{2}\frac{M_{fd}^2}{L_{fd}} \tag{A.11c}$$

Now the equation $v_d^2 + v_q^2 = V_{s\_max}^2$ can be written as

$$\left(A\frac{d}{dt}i_d + \omega B i_q\right)^2 + \omega^2 \left(Ai_d + CI_f\right)^2 = V_{s\_max}^2 \tag{A.12a}$$

or

$$\omega^2 \left[B^2 i_q^2 + \left(Ai_d + CI_f\right)^2\right] + \omega\left(2ABi_q\frac{d}{dt}i_d\right) + \left(A\frac{d}{dt}i_d\right)^2 - V_{s\_max}^2 = 0 \tag{A.12b}$$

Equation (A.12b) is quadratic in $\omega$ which can be solved using the quadratic root formula

$$\omega = \frac{-2ABi_q\frac{d}{dt}i_d \pm \sqrt{\left(2ABi_q\frac{d}{dt}i_d\right)^2 - 4\left[B^2 i_q^2 + \left(Ai_d + CI_f\right)^2\right]\left[\left(A\frac{d}{dt}i_d\right)^2 - V_{s\_max}^2\right]}}{2\left[B^2 i_q^2 + \left(Ai_d + CI_f\right)^2\right]} \tag{A.13}$$

The base speed is the rotor electrical speed $\omega_b$ at which the stator voltage reaches the maximum value of $V_{s\_max}$ when supplied with rated stator current. Thus, at this speed $i_q = I_t$, $i_d = \pm I_f$ and $\frac{d}{dt}i_d = \pm 4 I_f f_b$. Substituting those values in the above equation and solving gives four (two positive and two negative) values for $\omega_b$ corresponding to the four possibilities determined by the two $\pm$ operators in the equation. Let's use the part of the ellipse located in the first quadrant of the $i_d$-$i_q$ coordinate as the deciding curve. In this quadrant, the intersection is found under the area within the lower ellipse corresponding to $\frac{d}{dt}i_d = -4 I_f f_b$. In addition $i_d = I_f$. This quadrant represents the motoring operation region of the motor, i.e. $\omega > 0$ which is satisfied by using the plus sign infront of the square root sign. In general,

$$|\omega_b| = \frac{-8ABI_t I_f f_b + \sqrt{\left(8ABI_t I_f f_b\right)^2 - 4\left[B^2 I_t^2 + \left((A+C)I_f\right)^2\right]\left[\left(4AI_f f_b\right)^2 - V_{s\_max}^2\right]}}{2\left[B^2 I_t^2 + \left((A+C)I_f\right)^2\right]} \tag{A.14}$$

## A.3 Flux weakening $i_q$ calculation

For motor operating speed above the base speed $\omega_b$, first $I_f$ is decided according to the speed $\omega$ and $I_{f\_max}$. Once $I_f$ is determined, Equation A.12a can be solved for $i_q$ giving

$$i_q = \frac{-A\frac{d}{dt}i_d \pm \sqrt{V_{s\_max}^2 - (A+C)^2 I_f^2 \omega^2}}{B\omega} \tag{A.15}$$

The sign of $\frac{d}{dt}i_d$ is chosen based on which ellipse is used as the limiting curve. For positive values of of $i_q$, once $I_f$ is determined, the voltage limit is determined by the lower ellupse corresponding to $\frac{d}{dt}i_d = -4I_f f_b$. To give positive $i_q$ value, the sign of the square root must be negative since the sign of $B$ is negative. Thus, in general,

$$i_q = \frac{4AI_f f_b - \sqrt{V_{s\_max}^2 - (A+C)^2 I_f^2 \omega^2}}{B\omega} \tag{A.16}$$

# Appendix B

# Source Codes

## B.1 Model Simscape code

Listing B.1: Motor model code

```
component HWRRBSM
% Half-Wave Rectified Rotor Brushless Synchronous Motor
% This block models half-wave rectified brushless synchronous motor
% parametrized using constant inductance values. Connect the field winding
% rectifying diode using the 'ef+' and 'ef-' ports

    parameters
        % Main
        nPolePairs =  {1, '1'};            % Number of pole pairs
        wNominal = {0, 'rad/s'};           % Nominal mechanical speed

        % Impedances
        Ld  = {0.097,'H'}; % Stator d-axis self inductance, Ld
        Lq  = {0.049,'H'}; % Stator q-axis self inductance, Lq
        Mfd = {0.172,'H'}; % Stato-rotor d-axis Mutual inductance, Mfd
        Ra  = {1,'Ohm'};   % Stator phase winding resistance, Ra
        Lfd = {0.379,'H'}; % Rotor field circuit inductance, Lfd
        Rfd = {3,'Ohm'};   % Rotor field circuit resistance, Rfd

    end

    parameters (Access=protected)
        shift_3ph = { [0,-2*pi/3,2*pi/3], 'rad' };
    end


    nodes
        N = foundation.electrical.three_phase;           % ~:left
        R = foundation.mechanical.rotational.rotational; % R:right
        C = foundation.mechanical.rotational.rotational; % C:right
        ep = foundation.electrical.electrical;           % ef+:left
        en = foundation.electrical.electrical;           % ef-:left
    end

    variables
        % Mechanical
        angular_position_diff = {0, 'rad'}; % Rotor angle wrt synchronous reference
            frame
```

```
    % Flux linkages
    lambda_d = {0,'Wb'};
    lambda_q = {0,'Wb'};
    lambdaf_d = {0,'Wb'};
end

variables (Access=protected)
    % Mechanical
    torque = {0, 'N*m' };   % Mechanical torque

    % Stator currents
    I = {[0 0 0], 'A' };    % Phase currents
    i_d = {0, 'A'};         % d-axis current
    i_q = {0, 'A'};         % q-axis current

    if_d = {0, 'A'};        % d-axis rotor current
end

branches
    I      : N.I    -> *;
    if_d   : ep.i -> en.i;
    torque : C.t -> R.t;
end

equations
    let
        ef_d = ep.v - en.v;
        angular_velocity = R.w - C.w;
        electrical_angle = nPolePairs*(angular_position_diff + wNominal*time);
        electrical_angle_vec = electrical_angle+shift_3ph;

        % Set up Park's transform
        abc2dq = 2/3*[...
                 cos( electrical_angle_vec );...
                -sin( electrical_angle_vec )];

        dq2abc = [...
            cos(electrical_angle_vec(1)) -sin(electrical_angle_vec(1));...
            cos(electrical_angle_vec(2)) -sin(electrical_angle_vec(2));...
            cos(electrical_angle_vec(3)) -sin(electrical_angle_vec(3))];

        % Voltages a,b,c -> d,q
        vdq = abc2dq*N.V';
        ed = vdq(1);
        eq = vdq(2);

    in
        % Electric to mechanical rotation
        angular_velocity == wNominal + angular_position_diff.der;

        % Electrical equations
        ed == lambda_d.der - nPolePairs*angular_velocity*lambda_q + i_d*Ra;
        eq == lambda_q.der + nPolePairs*angular_velocity*lambda_d + i_q*Ra;
         0 == -lambdaf_d.der - Rfd*if_d + ef_d;


        % Flux Equations
        lambda_d  == Ld*i_d + Mfd*if_d;
        lambda_q  == Lq*i_q;
        lambdaf_d == (3/2)*Mfd*i_d + Lfd*if_d;
```

```
            I' == dq2abc*[i_d;i_q];
            % An equation constraining sum of currents equal to zero is
            % needed for dq0 transform, but not for the dq transform.
            % I(1)+I(2)+I(3) == 0;

            % Mechanical torque
            torque == 3/2*nPolePairs*(lambda_d*i_q - lambda_q*i_d);

        end
    end
end
```

## B.2 Inductance Extraction code

Listing B.2: Inductance Extraction

```
% This version of the script is used fof extracting the inductances in
% which
% 1. the model is single-pole,
% 2. coil b is excited by DC current  and
% 3. the rotor d-axix is aligned with the stator a-axis.
% Thus, the stator mutual inductances are between b and c, self inductance
% is that of coil b

% Assuming the COMSOL Server is started and the model is loaded to the
% MATLAB Workspace with the model tag 'model', the following lines of code
% extract the inductances of the motor.

% First the a-phase of the stator winding is excited with a DC current of 1
% A while the other phase windings are opened circuited including the
% rotor (field) winding. This step provides the self-inductance of the
% stator a-phase along with the mutual inductances of the other coils with
% this a-phase winding.

% The inductances of the other phase windings i.e. phases b and c is
% similar to the phase-a inductance expression except that they are shifted
% by 120 and 240 degrees with respect to the phase-a winding according to
% the position of the rotor.

model = ModelUtil.model('Model2');

I0 = 60; s3 = num2str(I0);
model.param.set('I0',s3);
model.param.set('If','0[A]');
model.sol('sol1').run;
Lbb = mphglobal(model,'mf.LCoil_b');
Lba = mphglobal(model,'mf.L_a1_b')+mphglobal(model,'mf.L_a2_b');
Lbc = mphglobal(model,'mf.L_c_b');
Lbr = mphglobal(model,'mf.L_r_b');
ra  = mphglobal(model,'mf.RCoil_b');


% From Laa0 + Laa2cos(2theta_r-2*pi/3) = Lbb, we have
Laa0 = mean(Lbb);

% and
Laa2 = max(Lbb - Laa0);
```

```
% From -Lab0 - Lab2cos(2theta_r-pi) = Lbc, we have
Lab0 = mean(-Lbc);
% Hence, we have
Lab2 = max(Lbc + Lab0); % only the peak to peak value is needed here
% Finally from Lbr = Lbfcos(theta_r), we have
Mfd = max(Lbr);

% DQ0 axis inductances
Ld = Laa0 + Lab0 + 0.5*Laa2 + Lab2;
Lq = Laa0 + Lab0 - 0.5*Laa2 - Lab2;
L0 = Laa0 - 2*Lab0;
Ra = mean(ra);

% To calculate the self-inductance of the rotor winding the dc excitation
% will be as follows, where the field winding is excited with 1 A current
% and the a-phase stator winding is left unexcited. By running the FEM
% solver again and extracting the solution, the rotor winding
% self-inductance can be obtained as follows.

model.param.set('I0','0[A]');
If = 60; s4 = num2str(If);
model.param.set('If',s4);
model.sol('sol1').run;
Lff = mphglobal(model,'mf.LCoil_r');
rfd = mphglobal(model,'mf.RCoil_r');
Rfd = mean(rfd);
Lfd = mean(Lff);
```

# Appendix C

# SIMULINK Blocks

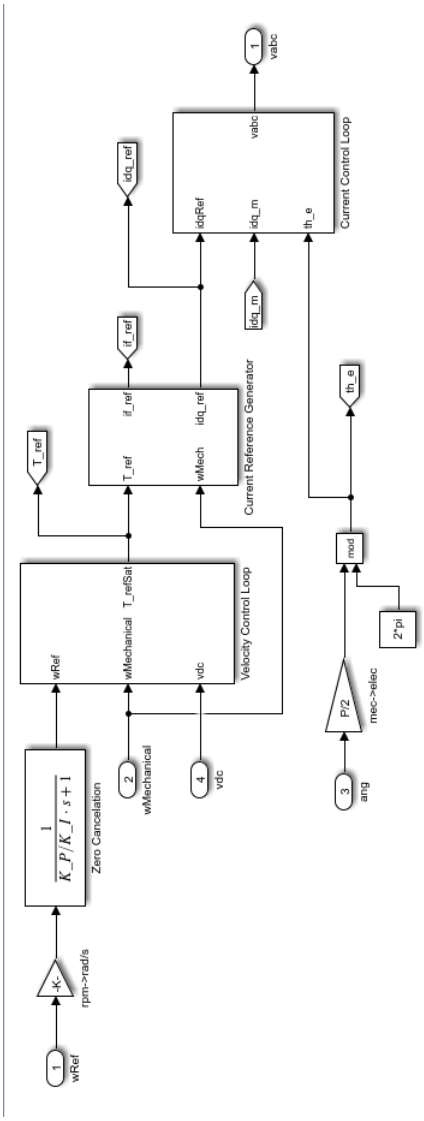


Figure C.1: Internal implementation of control block

The torque limiter block in Figure C.2 uses a lookup table generated for this specific motor to determine the maximum torque available at a given speed. This is done to prevent algebraic loops in the model during simulation.

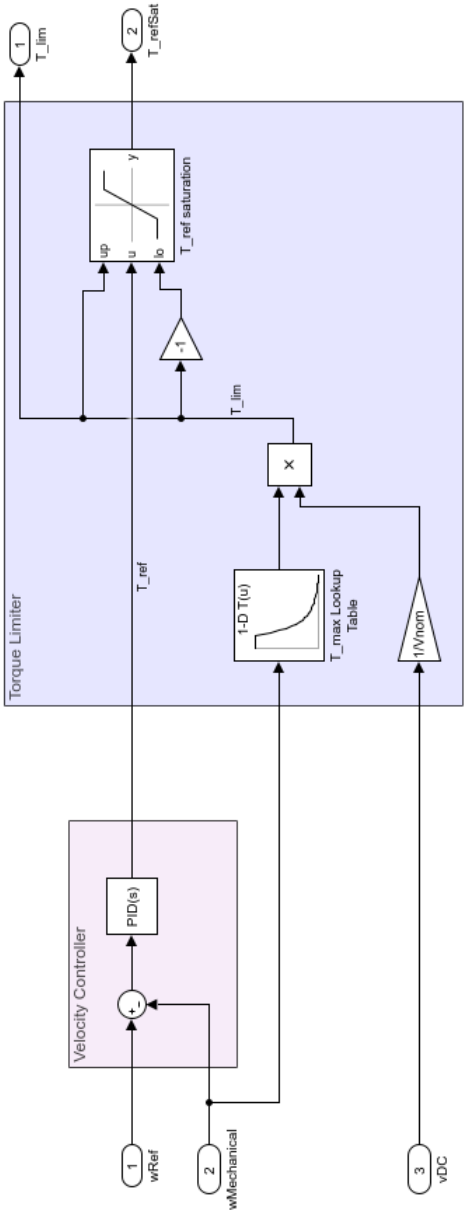


Figure C.2: Velocity controller with torque limiter

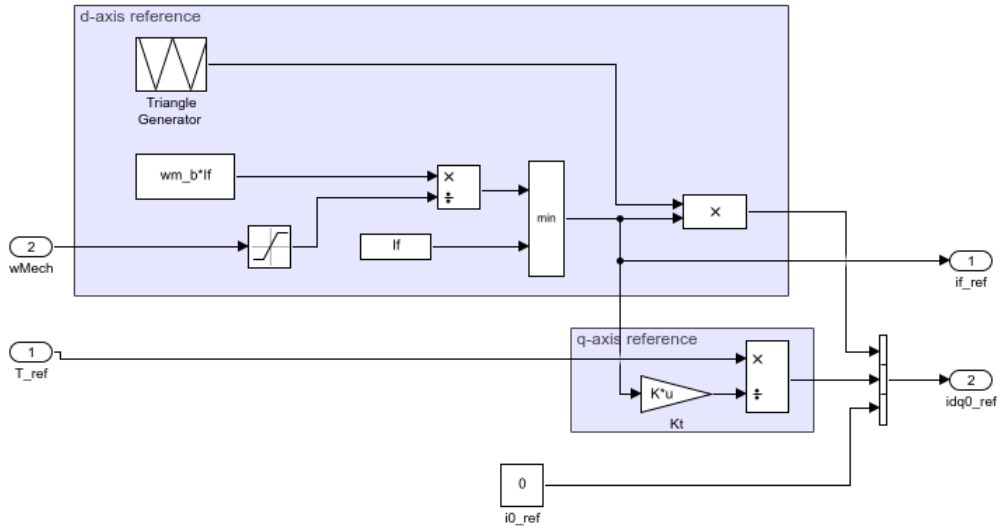


Figure C.3: Current reference generator implementation

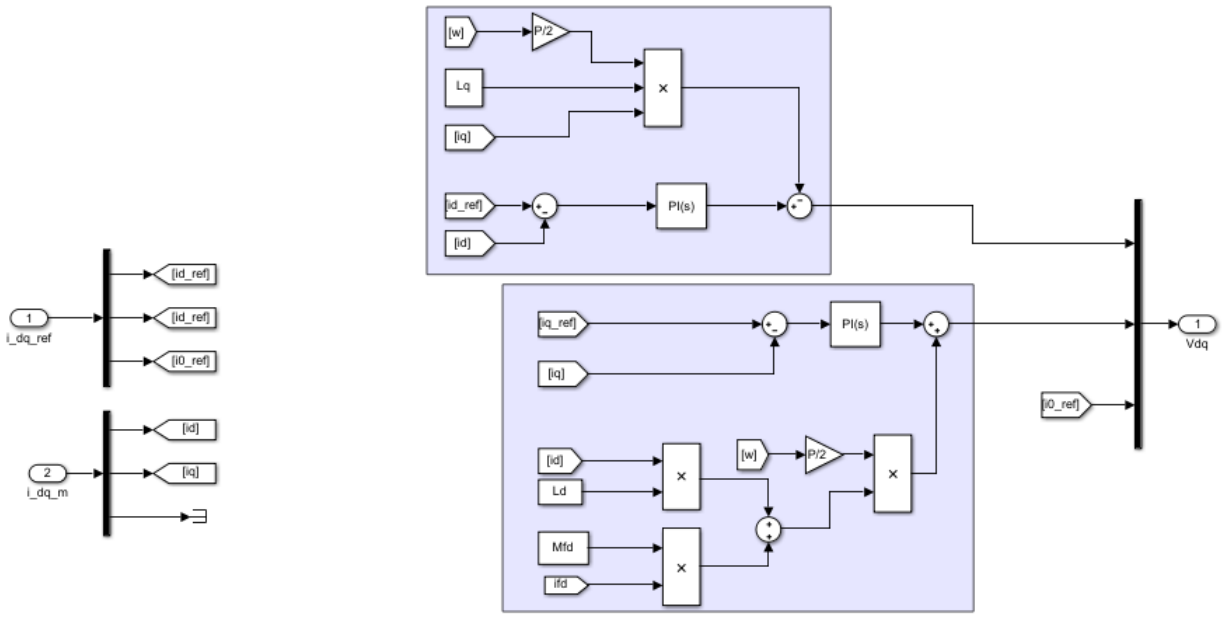


Figure C.4: DQ axis current controllers implementations

# Appendix D

# COMSOL Design Parameters

The following table shows the design of the FEM model geometry based on the procedure adapted from [27, 26]

Table D.1: COMSOL FEM model geometry design

| Name | Expression | Value | Description |
|---|---|---|---|
| $D_{os}$ | 260 [mm] | 0.26 m | Initial stator outer diameter |
| $T_e$ | 60 [Nm] | 60 N·m | Rated electromagnetic torque |
| $P_{mec}$ | $7.5 \times 10^3$ [W] | 7500 W | Rated mechanical power |
| $\omega_m$ | $\frac{P_{mec}}{T_e}$ | 125 1/s | Rated mechanical rotational speed |
| $ratio$ | 0.62 | 0.62 | Stator outer diameter to inner diameter ratio |
| $D_{is}$ | $D_{os}ratio$ | 0.1612 m | Stator inner diameter |
| $\sigma_m$ | 21e3 [Pa] | 21000 Pa | Tangential stress force |
| $\alpha_r$ | 0.5855 | 0.5855 | Rotor pole arc factor |
| $L$ | $4\frac{T_e}{\sigma_m \pi D_{is}^2 \alpha_r}$ | 0.13999 m | Axial length of the motor, saliency accounted |
| $L_{ag}$ | $0.18 + 0.01P_{mec}^{0.4}$ [mm] | $5.2461 \times 10^{-4}$ m | Air gap length |
| $Q_s$ | 48 | 48 | No. of stator slots |

Continued on next page

**Table D.1 – continued from previous page**

| | | | |
|---|---|---|---|
| P | 8 | 8 | No. of poles |
| m | 3 | 3 | No. of phases |
| q | $Q_s/Pm$ | 2 | No. of slots per pole per phase |
| $\tau_p$ | $\pi D_{is}/P$ | 0.063303 m | Stator pole pitch |
| $\tau_s$ | $\pi D_{is}/Q_s$ | 0.010551 m | Stator slot pitch |
| $\alpha$ | 0 [rad] | 0 rad | Winding piching angle |
| $k_p$ | $\cos 2\alpha$ | 1 | Coil pitch factor for the fundamental component |
| $n$ | $Q_s/P$ | 6 | No. stator slots per pole |
| $\beta$ | $\pi/n$ | 0.5236 | Electrical angular displacement b/n slots in rad |
| $k_d$ | $\frac{\sin q\frac{\beta}{2}}{q\sin\frac{\beta}{2}}$ | 0.96593 | Coil distribution factor |
| $k_w$ | $k_p k_d$ | 0.96593 | Coil winding factor |
| $A$ | $35 \times 10^3$ [A/m] | 35000 A/m | Linear current density |
| $pf$ | 0.9 | 0.9 | Assumed power factor |
| $\eta$ | 0.9 | 0.9 | Assumed motor efficiency |
| $B_{ag}$ | $\frac{\sqrt{2}\sigma}{Apf}$ | 0.94281 T | Calculated air gap flux density |
| $w_e$ | $P\frac{w_m}{2}$ | 500 1/s | Rated electrical angular speed |
| $e$ | 400 [V] | 400 V | Battery Voltage |
| $V$ | $e/\sqrt{3}$ | 230.94 V | Maximum line to line voltage |
| $alp$ | 0.85 | 0.85 | Pole arch flux distribution coefficient |
| $N_{ss}$ | $\frac{V}{w_e k_w B_{ag}\tau_p Lalp}$ | 78.843 | No. of turns of stator phase winding |

Continued on next page

**Table D.1 – continued from previous page**

| | | | |
|---|---|---|---|
| $z_q$ | $round(^{2mN_{ss}}/_{Qs})$ | 10 | No. of winding turns per slot rounded to the nearest integer |
| $N_s$ | $^{z_q Qs}/_{2m}$ | 80 | Corrected no. of turns to give integer no. of $z_q$ |
| $I_s$ | 63 [A] | 63 A | Rated stator current |
| $J_s$ | $6.5[A/mm^2]$ | $6.5 \times 10^6$ A/m² | Selected current density |
| $S_{Cu}$ | $^{I_s}/_{Js}$ | $9.6923 \times 10^{-6}$ m² | Stator winding copper area |
| $S_{sCu}$ | $z_q S_{Cu}$ | $9.6923 \times 10^{-5}$ m² | Slot area required for the copper winding |
| $ff$ | 0.7 | 0.7 | Winding slot filling factor |
| $S_{slot}$ | $^{S_s Cu}/_{ff}$ | $1.3846 \times 10^{-4}$ m² | Actual slot area required |
| $B_{sy}$ | 1.6 [T] | 1.6 T | Stator yoke flux density |
| $B_{st}$ | 2.2 [T] | 2.2 T | Stator tooth flux density |
| $w_{st}$ | $^{B_{ag}\tau_s}/_{B_{st}}$ | 0.0045214 m | Stator tooth width |
| $\alpha_{sp}$ | $^{\pi}/_{Q_s}$ | 0.06545 | Refer to Figure D.1a |
| $a$ | 1 | 1 | |
| $slot_{opf}$ | 0.2 | 0.2 | Slot opening factor |
| $s_0$ | $\tau_s slot_{opf}$ | 0.0021101 m | Slot opening |
| $\alpha_{st\_min}$ | $2a \sin \frac{w_{st}}{D_{is}}$ | 0.05609 | Minimum slot opening angle |
| $s_{0max}$ | $D_{is} \sin\left(\alpha_{sp} - \frac{\alpha_s t\_min}{2}\right)$ | 0.0060283 m | Maximum slot opening |
| $h_{s4}$ | 0.5 [mm] | $5 \times 10^{-4}$ m | slot opening rectangle height |
| $\alpha_w$ | 30 [deg] | 0.5236 rad | Refer to Figure D.1a |
| $h_{s3}$ | $\frac{\frac{s_{0max}-s_0}{2} + h_{s4} \tan \alpha_{sp}}{\frac{1}{\tan \alpha_w} - \tan \alpha_{sp}}$ | 0.0011952 m | Refer to Figure D.1a |

Continued on next page

**Table D.1 – continued from previous page**

| | | | |
|---|---|---|---|
| $h_{s2}$ | 0 [mm] | 0 m | slot classic insulation thickness |
| $w_{s3}$ | $s_{0max} + 2\left(h_{s4} + h_{s3}\right)\tan\alpha_{sp}$ | 0.0062505 m | Refer to Figure D.1a |
| $w_{s2}$ | $w_{s3} + 2h_{s2}\tan\alpha_{sp}$ | 0.0062505 m | Refer to Figure D.1a |
| $h_{s1}$ | $\frac{-w_{s2} + \sqrt{w_{s2}^2 + 4S_{slot}\tan\alpha_{sp}}}{2\tan\alpha_{sp}}$ | 0.018546 m | Refer to Figure D.1a |
| $w_{s1}$ | $w_{s2} + 2h_{s1}\tan\alpha_{sp}$ | 0.0086816 m | Refer to Figure D.1a |
| $h_s$ | $h_{s4} + h_{s3} + h_{s2} + h_{s1}$ | 0.020241 m | Stator slot height |
| $h_{sy1}$ | $\frac{B_{ag}\tau_p}{\pi B_{sy}}$ | 0.011874 m | Stator yoke height calculated from flux relationships |
| $D_{os1}$ | $\frac{round\left(1000(D_{is} + 2h_s + 2h_{sy1})\right)}{1000}$ | 0.225 m | Stator outer diameter computed from $h_{sy1}$ |
| $D_{or}$ | $D_{is} - 4Lag$ | 0.15906 m | Rotor outer diameter |
| $\theta_{rs}$ | $\frac{\pi}{5}$ [rad] | 0.62832 rad | Rotor pole spread angle |
| $pr_{arc}$ | $\alpha_r 2\frac{\pi}{2}$ [rad] | 0.45985 rad | Rotor pole arc angle |
| $k_{rr}$ | 0.7 | 0.7 | tampering factor |
| $D_{ir}$ | $0.4D_{or}$ | 0.063624 m | Rotor internal (axel) diameter |
| $h_{r1}$ | $D_{or}\cos\left(k_{rr}\frac{pr_{arc}}{2}\right)\sin\frac{pr_{arc}}{2}$ | 0.035782 m | Refer to Figure D.1b |
| $h_{r2}$ | $0.5h_{r1}$ | 0.017891 m | Refer to Figure D.1b |
| $h_{r3}$ | $0.2h_{r2}$ | 0.0035782 m | Refer to Figure D.1b |
| $w_{r3}$ | $\frac{h_{r1}}{4\tan\theta_{rs}}$ | 0.012312 m | Refer to Figure D.1b |
| $w_{r2}$ | $\frac{D_{or}}{2}\cos\left(k_{rr}\frac{pr_{arc}}{2}\right)\cos\left(\frac{pr_{arc}}{2}\right) - \frac{D_{ir}}{2} - w_{r3}$ | 0.032312 m | Refer to Figure D.1b |
| $w_r1$ | $w_{r2} + w_{r3}$ | 0.044624 m | Refer to Figure D.1b |

Continued on next page

| Table D.1 – continued from previous page | | | |
|---|---|---|---|
| $w_{r4}$ | $0.4w_{r2}$ | 0.012925 m | Refer to Figure D.1b |

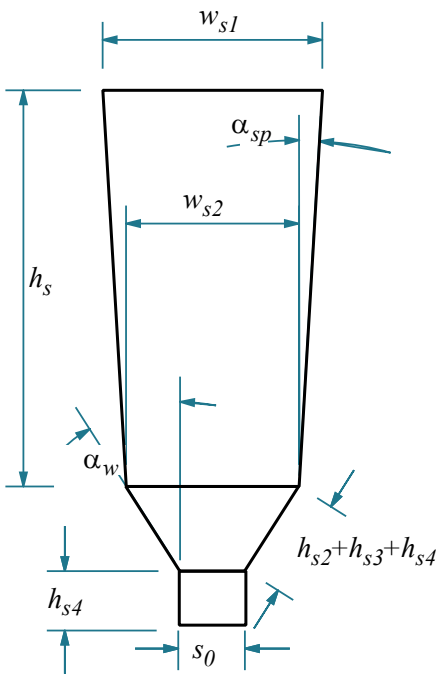


(a) Single stator slot

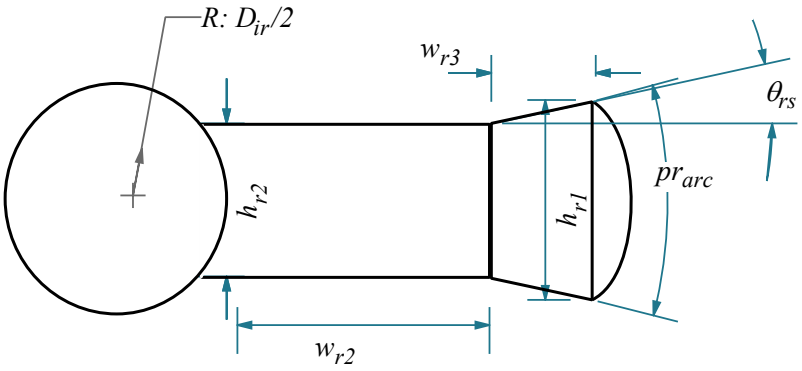


(b) Single rotor pole

Figure D.1: FEM model geometry parameters

# Bibliography


[1] *Vehicle traction motor design trends*. SAE International®. 2018. URL: https://www.sae.org/news/2018/05/latest-electric-motor-design-trends (visited on 05/30/2018).

[2] Ghulam Jawad et al. "Novel Brushless Wound Rotor Synchronous Machine With Zero Sequence Third Harmonic Field Excitation". In: *IEEE Trans. Magn.* 9464.c (2015), pp. 1–4. DOI: 10.1109/TMAG.2015.2512281.

[3] Byung-il Kwon and Asif Hussain. "A new brushless wound rotor synchronous machine using a special stator winding arrangement". In: *Electr. Eng.* (2017). ISSN: 1432-0487. DOI: 10.1007/s00202-017-0662-8.

[4] Fei Yao et al. "Principle of Operation and Performance of a Synchronous Machine Employing a New Harmonic Excitation Scheme". In: *IEEE Trans. Ind. Appl.* 9994.c (2015). DOI: 10.1109/TIA.2015.2425363.

[5] Jun Oyama et al. "Analysis of half-wave rectified brushless synchronous motor with permanent magnets". In: *Conference Record of the 1990 IEEE Industry Applications Society Annual Meeting*. IEEE. 1990, pp. 146–151.

[6] Jun Yamaguch et al. "Principle and fundamental characteristics of half-wave rectified brushless synchronous motor". In: *Electrical engineering in Japan* 107.6 (1987), pp. 98–106.

[7] Yuta Nakashima et al. "Fundamental output characteristics a claw pole type half-wave rectified variable field flux motor". In: *2017 20th International Conference on Electrical Machines and Systems (ICEMS)*. IEEE. 2017, pp. 1–5.

[8] Yuta Nakashima, Takashi Abe, and Tsuyoshi Higuchi. "Experimental investigations on variable field flux control of a claw pole type half-wave rectified variable field flux motor". In: *2016 19th International Conference on Electrical Machines and Systems (ICEMS)*. IEEE. 2016, pp. 1–5.

[9] Sakutaro Nonaka and Kunio Fujii. "Brushless self-excited three-phase synchronous motor driven by voltage source inverter". In: *Electrical engineering in Japan* 103.4 (1983), pp. 81–89.

[10] Ozlem Ozgun and Mustafa Kuzuoglu. *MATLAB-based Finite Element Programming in Electromagnetic Modeling*. Taylor & Francis Group, 2019. ISBN: 9781498784078.

[11] Kay Hameyer and Ronnie Belmans. *Numerical Modelling and Design of Electrical Machines and Drives*. 1st ed. WIT Press, 1999. ISBN: 1853126845.

[12] Erich Schmidt. "Finite element analysis of electrical machines and transformers: State of the art and future trends". In: *COMPEL-The international journal for computation and mathematics in electrical and electronic engineering* 30.6 (2011), pp. 1899–1913.

[13] Marius Rosu et al. *Multiphysics simulation by design for electrical machines, power electronics and drives*. Vol. 66. John Wiley & Sons, 2017.

[14] Thomas A Lipo. *Introduction to AC machine design*. Vol. 63. John Wiley & Sons, 2017.

[15] COMSOL Multiphysics® v. 5.5. *AC/DC Module User's Guide*. COMSOL AB. Stockholm, Sweden, 2018. URL: `https://www.comsol.com`.

[16] Nicola Bianchi. *Electrical Machine Analysis using Finite Elements*. 6000 Broken Sound Parkway NW: Taylor & Francis Group, 2005. ISBN: 9781420057874.

[17] *What Is the Curl Element (and Why It It Used)?* COMSOL Inc. 2019. URL: `https://www.comsol.com/blogs/what-is-the-curl-element-and-why-is-it-used` (visited on 12/30/2019).

[18] *An Introduction to the Finite Element Method*. COMSOL Inc. 2019. URL: `https://www.comsol.com/cyclopedia/multiphysics/finite-element-method` (visited on 12/30/2019).

[19] A E Fitzgerald, Charles Kingsley, and Stephen D Umans. *Electric Machinery*. McGraw-hill, 2003. ISBN: 0073660094.

[20] Prabha Kundur, Neal J Balu, and Mark G Lauby. *Power system stability and control*. Vol. 7. McGraw-hill New York, 1994.

[21] Paul C Krause, Oleg Wasynczuk, and Scott D. Sudhoff. *Analysis of Electric Machinery and Drive Systems*. 2nd ed. John Wiley & SONS. INC. PUBLICATION, 2002. ISBN: 0-471-14326-X.

[22] MATLAB® v. R2019. *Basic Principles of Modeling Physical Networks*. MathWorks, Natick, MA, USA, 2019. URL: `www.mathworks.com`.

[23] Takashi Abe, Kyosuke Maeda, and Tsuyoshi Higuchi. "Variable field flux characteristics of a novel claw pole type half-wave rectified variable field flux motor". In: *2015 18th International Conference on Electrical Machines and Systems (ICEMS)*. IEEE. 2015, pp. 2003–2007.

[24] Takashi Abe et al. "Influence of Rotor Structure on the Torque Characteristic of a Novel Claw Pole Type Half-Wave Rectified Variable Field Flux Motor". In: *2015 17th European Conference on Power Electronics and Applications (EPE'15 ECCE-Europe)*. IEEE. 2015, pp. 1–9.

[25] COMSOL Multiphysics® v. 5.5. *COMSOL Multiphysics Reference Manual*. COMSOL AB, Stockholm, Sweden, 2019. URL: www.comsol.com.

[26] Ion Boldea and Lucian Tutelea. *Electric Machines: Steady State, Transients, and Design with MATLAB*. 1st ed. 6000 Broken Sound Parkway NW: Taylor & Francis Group, 2010. ISBN: 9781420055726.

[27] Juha Pyrhonen, Tapani Jokinen, and Valeria Hrab. *Design of Rotating Electrical Machines*. John Wiley & Sons, 2008.

[28] COMSOL Multiphysics® v. 5.5. *COMSOL Multiphysics*. COMSOL AB, Stockholm, Sweden, 2019. URL: www.comsol.com.

[29] Lipeng Liu. *How the B-H Curve Affects a Magnetic Analysis (and How to Improve It)*. COMSOL Inc. 2019. URL: https://www.comsol.com/blogs/how-the-b-h-curve-affects-a-magnetic-analysis-and-how-to-improve-it/ (visited on 08/30/2019).

[30] British Stainless Steel Association. *Magnetic properties of austenitic stainless steels*. 2019. URL: https://www.bssa.org.uk/topics.php?article=4 (visited on 09/30/2019).

[31] Engineering ToolBox. *Permeability.* 2016. URL: https://www.engineeringtoolbox.com/permeability-d_1923.html (visited on 09/30/2019).

[32] Nirmal Paudel. *Guidelines for Modeling Rotating Machines in 3D*. 2016. URL: www.comsol.com/blogs/guidelines-for-modeling-rotating-machines-in-3d (visited on 2019).

[33] James C. Robinson. *An Introduction to Ordinary Differential Equations*. Cambridge University Press, 2004. ISBN: 9780521826501.

[34] James Larminie and John Lowry. *Electric Vehicle Technology Explained*. 2nd ed. John and Sons, 2012. ISBN: 9781119942733.

[35] Norman S Nise. *Control systems engineering*. John Wiley & Sons, 2020.

[36] Sang-Hoon Kim. *Electric Motor Control: DC, AC, and BLDC Motors*. 1st ed. Radarweg 29, PO Box 211, 1000 AE Amsterdam, Netherlands: Elsevier Inc., 2017. ISBN: 978-0-12-812138-2.

[37] Janusz Turowski and Marek Turowski. *Engineering Electrodnamics: Electric Machine, Transformer, and Power Equipment Design*. Taylor & Francis Group, 2014. ISBN: 9781466589322.